Title
Collision-less Coupling between Explosive Debris Plasma and Magnetized Ambient Plasma

Author
Bondarenko, Anton

Publication Date
2015

Peer reviewed|Thesis/dissertation

University of California
Los Angeles

Collision-less Coupling between Explosive Debris Plasma and Magnetized Ambient Plasma

A dissertation submitted in partial satisfaction
of the requirements for the degree
Doctor of Philosophy in Physics

by

Anton Sergeivich Bondarenko

2015

Abstract of the Dissertation

Collision-less Coupling between Explosive Debris Plasma and Magnetized Ambient Plasma

by

Anton Sergeivich Bondarenko

Doctor of Philosophy in Physics

University of California, Los Angeles, 2015

Professor Christoph Niemann, Chair

The explosive expansion of a dense debris plasma cloud into relatively tenuous, magnetized, ambient plasma characterizes a wide variety of astrophysical and space environments, including supernova remnants, interplanetary coronal mass ejections, and ionospheric explosions. In these and other related phenomena, collision-less electro-magnetic processes rather than Coulomb collisions typically mediate the transfer of momentum and energy from the debris plasma to the ambient plasma. In an effort to better understand the detailed physics of collision-less coupling mechanisms, compliment *in situ* measurements, and provide validation of previous computational and theoretical work, the present research utilizes a unique experimental platform at the University of California, Los Angeles (UCLA) to study the interaction of explosive debris plasma with magnetized ambient plasma in a reproducible laboratory setting. Specifically, by jointly employing the Large Plasma Device (LAPD) and the Phoenix laser facility, the super-Alfvénic, quasi-perpendicular expansion of laser-produced carbon (C) and hydrogen (H) debris plasma through preformed, magnetized helium (He) ambient plasma is investigated via a variety of sophisticated diagnostics, including emission spectroscopy, wavelength-filtered imaging, a magnetic flux probe, and a Langmuir probe. The key result is the direct observation of collision-less coupling via large Doppler shifts in a He II ion spectral line, which indicate that the ambient ions accelerate in response to the explosive debris plasma. Specifically, the He II ions accelerate along a trajectory that

qualitatively corresponds to the large-scale laminar electric field generated by the debris expansion. A custom computational approach is utilized to simulate the initial He II ion response to the explosive debris plasma, and a synthetic Doppler-shifted wavelength spectrum constructed from the simulated ion velocities excellently reproduces the experimental measurements, verifying that the observed He II ion acceleration quantitatively corresponds to the laminar electric field. The direct observation of laminar collision-less coupling is consistent with the parameter regime of the experiment and validates previous computational and theoretical studies.

The dissertation of Anton Sergeivich Bondarenko is approved.

Vassilis Angelopoulos

Troy A. Carter

Walter N. Gekelman

Christoph Niemann, Committee Chair

University of California, Los Angeles

2015

Table of Contents

List of Figures

List of Tables

Acknowledgments

I would like to thank:

My advisor, Prof. Chris Niemann, for his consistent availability to have scheduled and unscheduled discussions with his graduate students, for being a patient and polite communicator even during stressful times, and for being very open-minded and optimistic towards new research directions.

Dr. Carmen Constantin, for building, maintaining, and operating the laser systems that allowed us to perform our experiments.

Prof. Walter Gekelman, Prof. Troy Carter, and Prof. Vassilis Angelopoulos, for their guidance as members of my dissertation committee.

Dr. Steve Vincena, Dr. Bart Van Compernolle, and Dr. Shreekrishna Tripathi, for their indispensable assistance during our experiments on the LAPD, and for their willingness to stay late and come in on weekends to match our hectic schedule.

My fellow graduate students. In particular, Dr. Derek Schaeffer and Erik Everson, for their countless hours of mentoring, and without whom the process of becoming a good experimentalist would be inconceivably difficult; Eric Clark, for elucidating the complexities of our experiment through his simulations; and Jeffrey Bonde, for numerous involved discussions that deepened my understanding of the problems we were trying to solve.

Zoltan Lucky, Marvin Drandell, and Dr. Patrick Pribyl, for always willing to offer their assistance and expertise as we prepared for our experiments.

Harry Lockart and the other members of the Physics and Astronomy Machine Shop, for machining our various designs with impressive precision and getting it right the first time around.

My parents, for always being encouraging and understanding, even as my anticipated graduation date was postponed.

Vita

2006	B.A. (Physics), University of Colorado, Boulder
2010	M.S. (Physics), University of California, Los Angeles
2008-2010	Teaching Fellow, University of California, Los Angeles.
2010-2015	Research Fellow, University of California, Los Angeles.

Publications

A. S. Bondarenko, D. B. Schaeffer, E. T. Everson, S. E. Clark, C. G. Constantin, and C. Niemann. "Spectroscopic measurement of high-frequency electric fields in the interaction of explosive debris plasma with magnetized background plasma." *Physics of Plasmas*, **21**(12):122112, 2014.

A. S. Bondarenko, D. B. Schaeffer, E. T. Everson, C. G. Constantin, S. E. Clark, and C. Niemann. "Feasibility of characterizing laser-ablated carbon plasmas via planar laser induced fluorescence." *The Review of Scientific Instruments*, **83**(10):10E515, 2012.

CHAPTER 1

Introduction

1.1 Overview

The explosive expansion of a dense plasma cloud into relatively tenuous, magnetized, ambient plasma characterizes a wide variety of astrophysical and space environments. Supernova remnants in the free-expansion phase [56], for example, consist of stellar material rapidly moving through the surrounding magnetized interstellar plasma. Interplanetary coronal mass ejections [10] at the Sun produce fast-moving plasma bursts that can interact with the Earth's magnetosphere. Man-made explosions in the Earth's upper atmosphere, including high-altitude nuclear detonations [21] and magnetospheric particle tracer experiments [31, 35], involve explosive plasma expansion into the magnetized medium of the ionosphere.

In these and other related phenomena, the expanding "debris" plasma decelerates as it both interacts with the ambient plasma and expels the magnetic field within the debris cloud volume to form a diamagnetic cavity [64]. From basic considerations of momentum and energy conservation [5], it follows that the principal debris deceleration mechanism depends on the Alfvénic Mach number M_A, defined as the ratio of the debris expansion speed to the ambient plasma Alfvén speed. Specifically, in the super-Alfvénic limit ($M_A \gg 1$), the debris decelerates primarily due to momentum and energy transfer to the ambient plasma, while in the sub-Alfvénic limit ($M_A \ll 1$), the debris decelerates as it expends energy on the expulsion of the magnetic field. Naturally, both types of interactions play a significant role in the intermediate case ($M_A \sim 1$). A salient feature of many astrophysical and space environments is that the collisional mean free path exceeds the characteristic distance over which the

expanding debris significantly slows by orders of magnitude [65]. Thus, in the super-Alfvénic regime ($M_A > 1$), the expectation is that the debris plasma transfers substantial momentum and energy to the ambient plasma via collision-less, collective, electro-magnetic processes rather than through classical Coulomb collisions.

Collision-less momentum and energy transfer between explosive debris plasma and magnetized ambient plasma is a subject of ongoing research, and a number of recent theoretical and computational studies [13, 14, 29, 62, 63] have made significant progress by investigating the detailed physics of collision-less coupling mechanisms and defining parameters designed to predict the necessary plasma conditions for coupling (or decoupling) to occur. Presently, the proposed physical models and parameters demand experimental verification. The use of *in situ* observations of astrophysical and space phenomena for this purpose carries numerous challenges, including extraordinarily large spatial and temporal scales, irreproducibility, and limited data. Thus, properly scaled [19], parameter-controlled, reproducible laboratory experiments are crucial for complementing *in situ* measurements, validating theory and simulations, and moving towards a complete understanding of collision-less debris-ambient plasma interaction.

To this end, the present work reports a laboratory investigation of the super-Alfvénic, quasi-perpendicular expansion of laser-produced debris plasma through preformed, magnetized ambient plasma, utilizing a unique experimental platform at the University of California, Los Angeles (UCLA). This chapter begins by introducing important theoretical concepts (Section 1.2) and provides a detailed outline of the entire work to follow (Section 1.3).

1.2 Theoretical Background

1.2.1 Interaction Length Scales

To introduce the length scales associated with the explosion of a debris plasma cloud into surrounding magnetized plasma, it is useful to consider a spherically symmetric debris shell

consisting of N_d ions, each of mass m_d, radially expanding at speed V_d into a homogenous ambient plasma of density n_a and ion mass m_a. The ambient plasma is initially magnetized by a uniform magnetic field of magnitude B_0.

In the initial phase of explosive debris expansion (at times much earlier than a debris ion gyro-period but later than an electron gyro-period), the effectively free-streaming debris ions outrun the magnetically confined electrons, generating a radial electric field that keeps the electrons and ions together and maintains quasi-neutrality. This electric field drives the electrons into an azimuthal $\vec{E} \times \vec{B}$ drift, which, in conjunction with $\vec{\nabla} p_e \times \vec{B}$ electron pressure gradient drifts, produces a diamagnetic current inside the debris shell that lowers the magnetic field magnitude ($B < B_0$) within the volume bounded by the current layer (the diamagnetic cavity). A sufficiently strong diamagnetic current results in full expulsion of the magnetic field within the cavity ($B = 0$). More complicated effects [64] set up an additional, oppositely directed azimuthal current just ahead of the debris shell, which increases the magnetic field magnitude ($B > B_0$) over a small region in front of the cavity (the magnetic compression). Fig. 1.1 schematically demonstrates the formation of a diamagnetic current and the characteristic deformation of the magnetic field. As the debris plasma expansion continues, it propagates the diamagnetic current layer forward and the cavity increases in size. In addition, the debris interacts with the ambient plasma, either through classical Coulomb collisions or via collision-less, collective, electro-magnetic processes. Both the growing volume of the expelled magnetic field and coupling to the ambient plasma expend the debris plasma energy, slowing its expansion.[1] Eventually, the debris stops and the diamagnetic cavity reaches a maximum size, after which the magnetic field gradually returns to its original magnitude via diffusion.

The relative importance of the magnetic field to the ambient plasma in decelerating the expanding debris can be inferred by utilizing conservation of energy and momentum to define several useful length scales [5]. The magnetic stopping radius R_B characterizes the maximum

[1] Additional processes, such as the generation of shear Alfvén waves, can further expend the debris energy, though these losses are assumed to be negligible here.

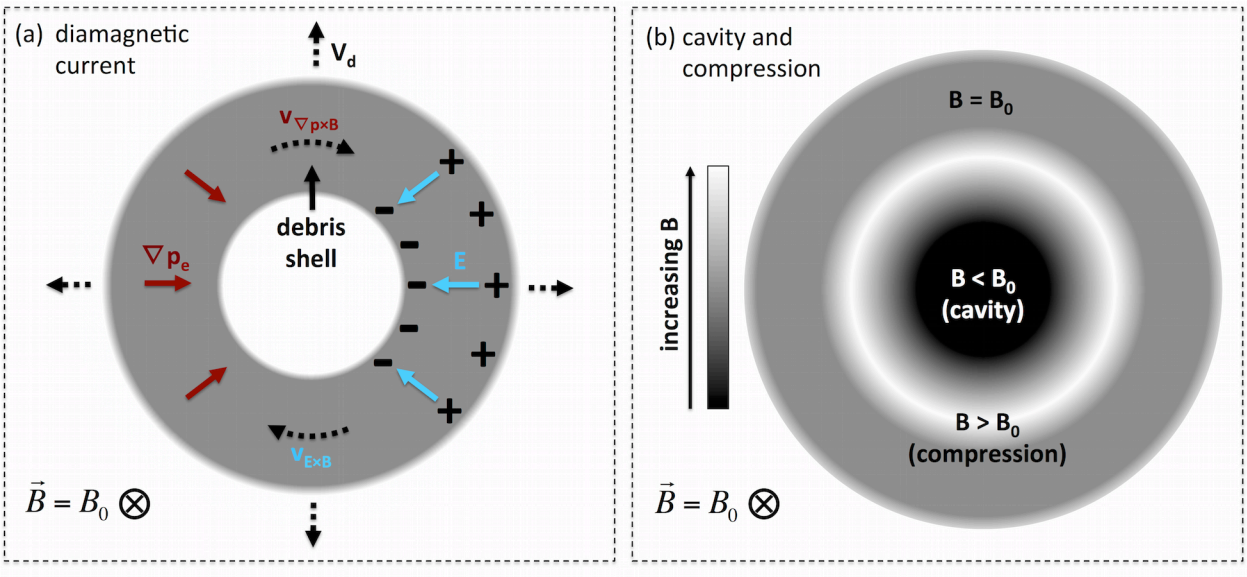

Figure 1.1: Schematic demonstration of the diamagnetic current and the characteristic deformation of the magnetic field for a radial debris shell expansion through an initially uniform magnetic field pointing into the page. In (a), the free-streaming ions outrun the magnetically confined electrons, generating a radially inward electric field that maintains quasi-neutrality. This electric field drives the electrons into an azimuthal $\vec{E} \times \vec{B}$ drift in the clockwise direction, which, in conjunction with the clockwise $\vec{\nabla} p_e \times \vec{B}$ drift due to an assumed radially inward electron pressure gradient, constitutes the diamagnetic current. As shown via the gray-scale contour in (b), this reduces the magnetic field magnitude within the current layer (the diamagnetic cavity). An additional, oppositely directed azimuthal current just ahead of the debris shell (not shown) increases the magnetic field magnitude in front of the cavity (the magnetic compression).

expansion of a debris shell provided that it only uses energy to expel the magnetic field, thus neglecting interactions with the ambient plasma. Assuming full expulsion within the diamagnetic cavity and ignoring the relatively insignificant volume spanned by the magnetic compression, the initial debris kinetic energy (carried almost entirely by the ions) can be equated to the energy of the expelled magnetic field within a spherical volume of radius R_B,

yielding

$$\frac{1}{2}N_d m_d V_d^2 = \left(\frac{B_0^2}{8\pi}\right)\left(\frac{4\pi R_B^3}{3}\right),\ R_B = \left(\frac{3N_d m_d V_d^2}{B_0^2}\right)^{\frac{1}{3}}. \tag{1.1}$$

The equal mass radius R_M characterizes the maximum expansion of a debris shell provided that it only couples to the ambient plasma, neglecting any interactions with the magnetic field. Assuming that all of the ambient ions are swept up and acquire the velocity of the debris ions, conservation of momentum requires that expansion stops when the debris ions overrun an equivalent mass of ambient ions. Equating the total debris mass to the total ambient mass within a spherical volume of radius R_M yields

$$N_d m_d = n_a m_a \left(\frac{4\pi R_M^3}{3}\right),\ R_M = \left(\frac{3N_d m_d}{4\pi n_a m_a}\right)^{\frac{1}{3}}. \tag{1.2}$$

The principal debris deceleration mechanism follows from the ratio of the magnetic stopping radius R_B to the equal mass radius R_M. This quantity is easily shown to depend on the ratio of the debris expansion speed V_d to the ambient plasma Alfvén speed $v_A \equiv \frac{B_0}{\sqrt{4\pi n_a m_a}}$, defined as the Alfvénic Mach number M_A:

$$\frac{R_B}{R_M} = V_d^{\frac{2}{3}}\left(\frac{4\pi n_a m_a}{B_0^2}\right)^{\frac{1}{3}} = \left(\frac{V_d}{v_A}\right)^{\frac{2}{3}} \equiv M_A^{\frac{2}{3}}. \tag{1.3}$$

In the limit $M_A \gg 1$, corresponding to a highly super-Alfvénic debris expansion, $R_M \ll R_B$ and R_M provides the stopping distance, indicating that the debris decelerates primarily due to coupling to the ambient plasma. In the limit $M_A \ll 1$, corresponding to a sub-Alfvénic debris expansion, $R_B \ll R_M$ and R_B yields the stopping distance, signifying that the debris decelerates due to expulsion of the magnetic field. In the intermediate case $M_A \sim 1$, $R_B \sim R_M$ and both types of interactions play a significant role in slowing the debris.

While the above arguments demonstrate that coupling between explosive debris plasma and magnetized ambient plasma is significant in the super-Alfvénic regime ($M_A > 1$), the detailed physics of the coupling mechanisms have yet to be addressed. In environments of sufficiently high density, classical Coulomb collisions provide effective momentum and energy transfer from debris to background. However, in the tenuous conditions of typical astrophysical and space phenomena, the debris ion-ambient ion and debris ion-ambient electron

collisional mean free paths exceed the characteristic debris stopping distance (e.g., the equal mass radius R_M) by orders of magnitude, indicating that collision-less, collective, electromagnetic processes are responsible for debris-ambient coupling. Collision-less momentum and energy transfer can generally be attributed to either turbulent mechanisms, which involve the development of plasma instabilities, or laminar mechanisms, corresponding to the generation of large-scale electric fields. The following two subsections explore turbulent and laminar collision-less coupling in further detail.

1.2.2 Turbulent Collision-less Coupling

Turbulent collision-less coupling involves the development of instabilities that effectively transfer energy from debris to background. A candidate mechanism is the magnetized ion-ion two-stream instability [47], which develops due to the relative streaming of debris ions through ambient ions across a magnetic field and converts the directed debris ion energy into thermal ambient ion energy. Another potential mechanism is the modified two-stream instability [40], which results from the relative drift between the debris ions and electrons across a magnetic field and couples the directed debris energy into ambient ion thermal energy perpendicular to the magnetic field and electron thermal energy parallel to the magnetic field. Excitation of these instabilities requires the Alfvénic Mach number M_A associated with the debris expansion to satisfy the condition

$$M_A \leq (1+\beta_e)^{\frac{1}{2}}\ ,\ \beta_e \equiv \frac{8\pi n_e k_B T_e}{B_0^2}, \tag{1.4}$$

where n_e and T_e are the electron density and temperature, k_B is Boltzmann's constant, and B_0 is the magnetic field magnitude. In the limit $\beta_e \ll 1$, typical of many astrophysical and space environments, the above condition reduces to $M_A \leq 1$, indicating that turbulent collision-less coupling mechanisms are typically ineffective in the super-Alfvénic regime.

1.2.3 Laminar Collision-less Coupling

In laminar collision-less coupling, large-scale electric fields that arise as debris plasma expands into magnetized ambient plasma accelerate the ambient ions. A general expression for the laminar electric field follows from a combination of the electron fluid momentum equation and Ampere's Law. Ignoring resistivity due to collisional or anomalous effects, the electron momentum equation is

$$m_e n_e \frac{d\vec{v}_e}{dt} = -\vec{\nabla} p_e - e n_e \left(\vec{E} + \frac{\vec{v}_e}{c} \times \vec{B} \right), \tag{1.5}$$

where m_e, n_e, $\vec{v}_e$, and $p_e = n_e k_B T_e$ are the electron mass, density, fluid velocity, and scalar pressure, respectively, e is the elementary charge, c is the speed of light, and $\vec{E}$ and $\vec{B}$ are the electric and magnetic fields. As the system evolves, quasi-neutrality dictates that the electrons continually redistribute themselves to locally match the total charge density of all the debris and ambient ion species, each of density n_i and charge number Z_i, such that

$$n_e \cong \sum\nolimits_i Z_i n_i. \tag{1.6}$$

On time scales relevant to significant momentum and energy transfer from the debris ions to the ambient ions, the electrons respond almost instantaneously due to their negligible mass and transient behavior can be ignored. Thus, a good approximation to Eq. 1.5 is the massless electron limit $m_e \to 0$, which allows for a solution to the laminar electric field:[2]

$$\vec{E}_{lam} = -\frac{1}{e n_e} \vec{\nabla} p_e - \frac{\vec{v}_e}{c} \times \vec{B}. \tag{1.7}$$

Eq. 1.7 can be expressed in terms of the ion current densities by substitution from Ampere's Law. Neglecting the displacement current corresponding to transient high-frequency components of the electric and magnetic fields and solving for the electron fluid velocity $\vec{v}_e$ in terms of the ion current densities $\vec{J}_i$ yields

$$\vec{\nabla} \times \vec{B} = \frac{4\pi}{c} \left(\sum\nolimits_i \vec{J}_i - e n_e \vec{v}_e \right), \; \vec{v}_e = \frac{1}{e n_e} \left(\sum\nolimits_i \vec{J}_i - \frac{c}{4\pi} \vec{\nabla} \times \vec{B} \right), \tag{1.8}$$

[2]The massless assumption that eliminates the left-hand side of Eq. 1.5 cannot be applied to the ions, elucidating why the electron momentum equation is the starting point for the derivation of the laminar electric field.

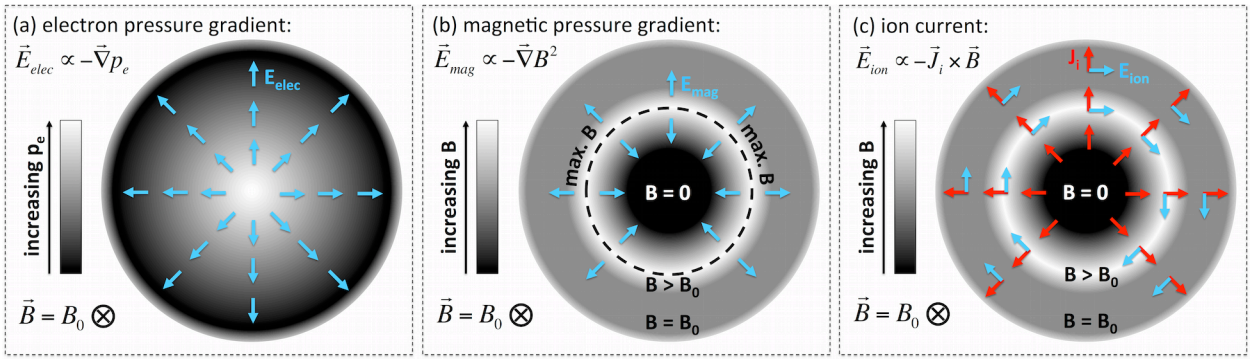

Figure 1.2: Schematic demonstration of the direction of the three terms comprising the laminar electric field of Eq. 1.9, assuming a spherically symmetric, radial debris expansion through a magnetic field pointing into the page. In (a), the electron pressure represented by the gray-scale contour is assumed to increase towards the center of the debris cloud, which, in accordance with the first term, results in a radially outward electric field. In (b), the magnetic field profile represented by the gray-scale contour shows full expulsion within the diamagnetic cavity and compression at the cavity edge. In accordance with the second term, and under the reasonable assumption that the magnetic pressure gradient significantly exceeds the magnetic tension in the central plane perpendicular to the magnetic field, the resulting electric field points in the direction of decreasing magnetic field magnitude, radially away from the maximum of the compression. In (c), the radial debris ion current generates an azimuthal electric field in the clockwise direction where the magnetic field is non-zero, in accordance with the third term.

where the sum is taken over all the debris and ambient ion species. Substitution of Eq. 1.8 into Eq. 1.7 produces the expression

$$\vec{E}_{lam} = -\frac{1}{en_e}\vec{\nabla} p_e - \frac{1}{4\pi e n_e}\vec{B} \times \left(\vec{\nabla} \times \vec{B}\right) - \frac{1}{en_e c}\sum\nolimits_i \vec{J}_i \times \vec{B}. \tag{1.9}$$

From Eq. 1.9, it follows that the laminar electric field arises due to three features: electron pressure gradients (first term), spatial variations in the magnetic field (second term), and ion currents across the magnetic field (third term). The first and third terms can be understood intuitively from the requirement of quasi-neutrality (Eq. 1.6). The first term expresses the

electric field that must work against the electron flux generated by gradients in density and temperature in order to keep the electrons and ions together, while the third term represents the electric field that must work against the $\vec{v} \times \vec{B}$ Lorentz force that attempts to push apart electrons and ions moving across the magnetic field. The second term can be interpreted by utilizing a vector identity to express it as

$$-\frac{1}{4\pi e n_e}\vec{B} \times \left(\vec{\nabla} \times \vec{B}\right) = \frac{1}{e n_e}\left[-\vec{\nabla}\frac{B^2}{8\pi} + \frac{\left(\vec{B} \cdot \vec{\nabla}\right)\vec{B}}{4\pi}\right]. \tag{1.10}$$

This term thus represents the effective force caused by magnetic pressure gradients $-\vec{\nabla}B^2/8\pi$ and magnetic tension $\left(\vec{B} \cdot \vec{\nabla}\right)\vec{B}/4\pi$. If the magnetic pressure gradients significantly exceed the tension (a reasonable scenario in the plane perpendicular to the magnetic field), the resulting electric field due to this term simply points in the direction of decreasing magnetic field magnitude. As demonstrated schematically in Fig. 1.2, all three features contributing to the laminar electric field can arise in the context of explosive debris plasma expansion into a magnetized background.

Collision-less momentum and energy transfer takes place as the ambient ions are subjected to the laminar electric field, resulting in acceleration due to the Lorentz force,

$$\vec{a} = \frac{Z_a e}{m_a}\left(\vec{E}_{lam} + \frac{\vec{v}_a}{c} \times \vec{B}\right), \tag{1.11}$$

where Z_a, m_a, and $\vec{v}_a$ are the ambient ion charge number, mass, and velocity, respectively. Generally, the ambient ion trajectory is highly complex because the laminar electric field consists of components of various orientations (Fig. 1.2) and, along with the magnetic field, depends on position and time. However, some insight into the ambient ion response can be obtained by considering the relative magnitudes of the three terms comprising Eq. 1.9 [5]. First, the ratio of the electron pressure gradient term to the magnetic pressure gradient and tension term scales as

$$\frac{\left|\frac{1}{e n_e}\vec{\nabla} p_e\right|}{\left|\frac{1}{4\pi e n_e}\vec{B} \times \left(\vec{\nabla} \times \vec{B}\right)\right|} \sim \beta_e. \tag{1.12}$$

In the limit $\beta_e \ll 1$, representative of astrophysical and space environments, the magnetic pressure gradient and tension term thus significantly exceeds the electron pressure gradient

term. Second, the ratio of the cross-field ion current term to the magnetic pressure gradient and tension term scales as

$$\frac{\left|\frac{1}{en_e c}\sum_i \vec{J}_i \times \vec{B}\right|}{\left|\frac{1}{4\pi e n_e}\vec{B} \times \left(\vec{\nabla} \times \vec{B}\right)\right|} \sim \frac{L}{d_i} M_A, \tag{1.13}$$

where M_A is the Alfvénic Mach number of the debris expansion, L denotes the spatial scale of significant variations in the magnetic field, and d_i is the ion inertial length. It therefore follows that, in the super-Alfvénic limit ($M_A \gg 1$), the cross-field ion current term provides the dominant contribution to the laminar electric field.[3] Laminar coupling in this limit, typically termed Larmor coupling, characteristically involves an $\vec{E} \times \vec{B}$ drift of the ambient ions in the original direction of the cross-field component of the debris ion current. Fig. 1.3 illustrates the ambient ion response for the simplified case of a uniform current and magnetic field. Secondary effects, such as debris ion deceleration and laminar electric field components due to ambient ion currents, are not considered here.

1.2.4 Coupling Parameters

Collision-less coupling in the super-Alfvénic regime has been the subject of a number of recent theoretical and computational studies. These investigations have proposed several parameters designed to predict the necessary plasma conditions for debris-ambient coupling (or decoupling) to occur. In [29], for example, a theoretical analysis of Larmor coupling determined that the debris ions fail to couple to the ambient ions provided that the parameter α falls in the range

$$\omega_{ca}\delta t_d < \alpha < 1,\ \alpha \equiv \frac{\pi}{2}\frac{Z_d n_d}{(Z_d n_d + Z_a n_a)}, \tag{1.14}$$

where ω_{ca} is the ambient ion gyro-frequency, δt_d is the temporal duration of the debris current at any given position, Z_d and n_d are the debris ion charge number and density, and Z_a and n_a are the ambient ion charge number and density. The upper limit ($\alpha < 1$) expresses that effective coupling does not occur if the cross-field ion current term of the

[3] This term is also dominant if cross-field ion currents exists in a region of uniform magnetic field, where magnetic pressure gradients and tension do not exist.

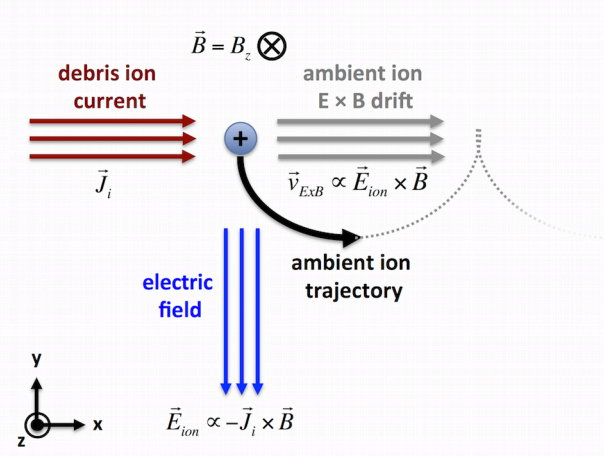

Figure 1.3: Schematic demonstration of Larmor coupling. A uniform debris ion current directed in the $+x$ direction moves through a uniform magnetic field pointing in $-z$ and generates an electric field in $-y$, in accordance with the dominant third term of Eq. 1.9. A stationary ambient ion subjected to the laminar electric field initially accelerates in $-y$ and rotates into $+x$ within one-quarter of a gyro-period due to the Lorentz force caused by the magnetic field. Provided that the ambient ion does not stream ahead of the debris, it continues to follow an $\vec{E} \times \vec{B}$ trajectory with a gyro-center drift in $+x$.

laminar electric field is insufficient to accelerate an ambient ion up to the speed of the debris ions within one-quarter of a gyro-period (see Fig. 1.3). The lower limit ($\alpha > \omega_{ca}\delta t_d$) implies that coupling fails if the ambient ion gyro-radius exceeds the spatial width of the debris pulse. The study thus concluded that the efficiency of debris-ambient coupling depends, in part, on the ratio of the ambient charge density to the debris charge density. Another investigation [14] utilizing "hybrid code" simulations (kinetic ions, massless fluid electrons) verified that strong debris-ambient coupling depends on a parameter proportional to R_M/ρ_d, where R_M is the equal mass radius and ρ_d is the directed debris ion gyro-radius. For example, for the specific case of C V debris ions expanding into H ambient plasma, strong coupling only occurs when $R_M/\rho_d > 0.7$. This semi-empirical condition follows from the requirement that the simulated debris-ambient interaction is sufficient to launch a collision-less shock into the ambient plasma. The study thus verified that strong coupling generally requires the

debris ion gyro-radius to be smaller than the characteristic debris stopping distance. Similar coupling parameters have also been derived analytically and computationally in other related work [4, 25].

1.3 Outline

A complete understanding of collision-less momentum and energy coupling between super-Alfvénic debris plasma explosions and surrounding magnetized plasmas currently demands experimental investigation in the context of properly scaled, parameter-controlled, reproducible laboratory environments. Recent experiments [44, 48, 51] have utilized a super-Alfvénic debris plasma "piston" to successfully drive quasi-perpendicular collision-less shocks into ambient, magnetized plasma. Additional experiments and observational studies [12, 56] have also explored the role of magnetized streaming instabilities in collision-less debris-ambient interaction. However, investigations of the detailed physics of laminar coupling mechanisms (i.e., the role of Eq. 1.9) and related coupling parameters (e.g., Eq. 1.14) have been largely limited to computational and theoretical work, with the exception of a recent study [53].

To this end, the present work reports a laboratory investigation of the super-Alfvénic, quasi-perpendicular expansion of laser-produced carbon (C) and hydrogen (H) debris plasma through preformed, magnetized helium (He) ambient plasma, utilizing a unique experimental platform at the University of California, Los Angeles (UCLA). Sophisticated diagnostics, including emission spectroscopy, wavelength-filtered imaging, a magnetic flux probe, and a Langmuir probes, monitor the debris-ambient interaction. The subsequent analysis utilizes various computational tools, including radiation-hydrodynamic modeling, collisional-radiative modeling, synthetic wavelength spectrum generation, and custom simulations, in order to compare the experimental data to the theoretical framework. The key result of this work is the direct observation of collision-less debris-ambient coupling that is consistent with the laminar electric field.

Chapter 2 introduces the experiment and reports the key features of debris-ambient interaction discerned from the data. The results provide direct evidence of laminar collision-less coupling between the laser-produced debris and the magnetized He background. Specifically, strong Doppler shifts detected in a He II ion spectral line indicate acceleration, and the inferred He II ion trajectory is determined to be qualitatively consistent with the laminar electric field of Eq. 1.9. In addition, the data indicates that the debris-ambient interaction results in the generation of energetic electrons.

Chapter 3 investigates whether the observed initial He II ion acceleration in response to the laser-produced debris is quantitatively consistent with the laminar electric field. The analysis first develops a simple model of the debris plasma expansion that allows for a direct calculation of the laminar electric field as a function of position and time via Eq. 1.9. The calculated electric field is then utilized to simulate the initial He II ion response. Comparison to the experimental data shows excellent agreement and self-consistency with the theoretical framework of laminar collision-less coupling. Limitations of the analysis are also addressed. Finally, Chapter 4 summarizes the key conclusions and recommends future steps in order to further this research.

Appendix A presents preliminary evidence of instabilities in the context of laser-produced debris expansion into magnetized He background, based on an experiment similar to that of Chapter 2. Specifically, harmonic modulations observed in a He II ion spectral line suggest strong oscillatory electric fields, in accordance with the time-dependent Stark effect. A detailed analysis of the spectra yields estimates of the electric field magnitudes and frequencies, which are found to be consistent with the electrostatic electron beam-plasma instability provided that the debris-ambient interaction generates sufficiently energetic electrons. Additional experimental evidence for the existence of such fast electrons and potential fast electron generation mechanisms are discussed.

Appendix B provides a feasibility study of utilizing the planar laser-induced fluorescence (PLIF) diagnostic in order to characterize laser-produced debris plasmas. In particular, PLIF schemes accessible to commercially available tunable lasers are identified for several

C ion charge states by utilizing radiation-hydrodynamic and collisional-radiative modeling. Because PLIF characterization yields a three-dimensional visualization of the debris expansion, it can potentially improve upon the debris expansion model of Chapter 3 and thus further develop understanding of collision-less debris-ambient interaction.

CHAPTER 2

Experimental Observation of Debris-Ambient Interaction

2.1 Overview

As detailed in Chapter 1, collision-less coupling between explosive debris plasma and magnetized ambient plasma, in which collective, electromagnetic processes rather than classical Coulomb collisions mediate the momentum and energy transfer, characterizes a variety of astrophysical and space phenomena. Moreover, theoretical arguments demonstrate that in the low-beta limit ($\beta_e \equiv \frac{8\pi n_e k_B T_e}{B_0^2} \ll 1$) typifying these environments, super-Alfvénic ($M_A > 1$) debris expansions couple to the magnetized background plasma primarily through large-scale laminar electric fields. The present lack of experimental data regarding laminar collision-less coupling motivates the need for reproducible laboratory experiments that can compliment *in situ* measurements and provide validation of computational and theoretical work. To this end, a unique experimental platform at the University of California, Los Angeles (UCLA), has been utilized to study the super-Alfvénic, quasi-perpendicular expansion of laser-produced carbon (C) and hydrogen (H) debris plasma through preformed, magnetized helium (He) ambient plasma via a variety of sophisticated diagnostics, including emission spectroscopy, wavelength-filtered imaging, a magnetic flux probe, and a Langmuir probe.

This chapter reports the key features of debris-ambient interaction discerned from the experimental data. Section 2.2 introduces the laboratory facility and describes the configuration and parameters of the experiment and the diagnostics in detail. Section 2.3 assesses the initial electron and ion temperatures and densities of the preformed, magnetized He ambient

plasma, prior to its perturbation by the laser-produced debris. Section 2.4 then examines the effect of the explosive debris on the He background, focusing on two principal observations. First, the debris-ambient interaction results in the generation of energetic electrons. Second, and of greater significance in the context of this work, Doppler shifts in a He II ion spectral line directly indicate that the explosive debris causes an acceleration of the He II ions along a trajectory that is qualitatively consistent with the laminar electric field (Eq. 1.9). The data analysis in this section is primarily qualitative. A quantitative treatment of the observed He II ion acceleration is presented in Chapter 3. Finally, Section 2.5 concludes this chapter by summarizing the main experimental results.

2.2 The Experiment

2.2.1 Experimental Platform

The unique experimental platform at UCLA for investigating the interaction between explosive debris plasma and magnetized ambient plasma utilizes two facilities in combination. The first facility, the Large Plasma Device (LAPD) [24], creates a well-characterized, current-free, steady-state (10 ms), highly reproducible (1 Hz), and large plasma column (18 m length, $\sim$ 1 m diameter) via cathode-anode discharge using a variety of gas fills (typically H, He, Ne, and Ar). Magnetic coils along the length of the machine generate a configurable axial magnetic field ($200 - 1800$ G) that magnetizes and radially confines the plasma. Numerous ports along the LAPD allow for diagnostic access. The second facility, the Phoenix Laser Laboratory, provides three laser systems that can be used to generate explosive debris plasma via ablation of solid targets (typically graphite or plastic) or as diagnostic beams. The kJ-class Raptor laser [43] generates the most energetic pulse (1053 nm, 25 ns, $>$ 200 J) and requires 45 minutes between shots in order for the flash lamps to cool sufficiently. The Phoenix laser [17], typically utilized in parallel with Raptor as a diagnostic beam, produces a lower-energy pulse (1064 nm, 5 ns, 20 J) once every 5 minutes. Peening, the newest laser system, delivers pulses (1053 nm, 16 ns, 30 J) at a maximum rate of 6 Hz. A typical

experiment jointly utilizes the two facilities as follows: a solid target embedded within the LAPD is irradiated with one of the lasers, generating explosive ablation plasma that expands through the preformed, magnetized plasma. Concurrently, a variety of diagnostics monitor the debris-ambient interaction.

2.2.2 Setup and Parameters

In the present experiment, schematically illustrated in Fig. 2.1 and Fig. 2.2, the LAPD generates steady-state He plasma via an 8 ms long discharge of a single, high-emissivity lanthanum hexaboride (LaB_6) cathode located at one end of the machine. In the region relevant to the experiment, the plasma is radially confined by an axial magnetic field of 710 G. The resulting magnetized plasma column, roughly aligned to the central axis, has a diameter of ≈ 20 cm, a typical electron density of $\approx 7 \times 10^{12}$ cm^{-3}, and a typical electron temperature of ≈ 4 eV. (Section 2.3 contains a more detailed characterization of the ambient plasma parameters). A long, rectangular high-density polyethylene $(C_2H_4)_n$ target is submerged into the LAPD and offset from the central axis by 30 cm, with the target surface normal oriented perpendicular to the magnetic field. The Raptor laser, operating at 150 ± 20 J per 5 ns pulse, is focused onto the target at an angle of 30° to the surface normal through a 1.8 m focal length lens, resulting in a spot diameter of 1.5 mm^2 and a surface intensity of 1.7 ± 0.3 TW/cm^2. The energetic laser pulse, timed to irradiate the target 7.5 ms after the start of the LaB_6 cathode discharge, ablates and ionizes the surface, producing explosive plasma consisting of various C and H ion charge states. Because laser-ablated plasma is primarily directed along the target surface normal independent of the laser angle of incidence, the present target orientation ensures that the debris expands quasi-perpendicular to the magnetic field and through the maximal volume of ambient plasma. The target is moved up or down between every laser shot to provide a fresh, flat surface for ablation. Since the target offset from the central axis (30 cm) is larger than the radius of the preformed He plasma column (≈ 10 cm), the laser-produced debris must expand through a region of neutral He gas before reaching the ambient plasma. Table 2.1 summarizes the experimental parameters.

laser energy	150 ± 20 J
laser intensity	1.7 ± 0.3 TW/cm^2
background magnetic field	710 G
debris plasma species	C and H
ambient plasma species	He
ambient plasma diameter	≈ 20 cm
ambient electron density	$\approx 7 \times 10^{12}$ cm^{-3}
ambient electron temperature	≈ 4 eV

Table 2.1: Parameters of debris-ambient coupling experiment.

2.2.3 Coordinate System

In the co-ordinate system utilized for the present experiment, the horizontal dimension across the diameter of the machine defines the x axis, the vertical direction across the diameter defines the y axis, and the long, axial dimension defines the z axis. The location of the target center closest to where the laser irradiates the target surface defines the origin $(x, y, z) = (0, 0, 0)$ cm, but due to the finite target width, the laser actually impinges on the target at $(x, y, z) = (0.6, 0, 0)$ cm. The time at which the laser pulse first irradiates the target defines the initial time $t = 0$ s. The target surface normal (and thus the primary direction of debris plasma expansion) is oriented in $+x$, and the coils of the LAPD produce a magnetic field that points in $-z$. The primary axis of debris expansion (the "blow-off axis") is defined by $(y, z) = (0, 0)$ cm, and the central perpendicular plane (the "blow-off plane") is defined by $z = 0$ cm. The central axis of the LAPD corresponds to $(x, y) = (30, 0)$ cm.

2.2.4 Diagnostics

Four primary diagnostics are utilized in this experiment. First, a custom-built spectroscopic fiber probe is fixed at coordinates $(y, z) = (-30, 0)$ cm and freely moves along x via a motorized 1D drive. The probe is oriented to collect line-integrated light emission along y

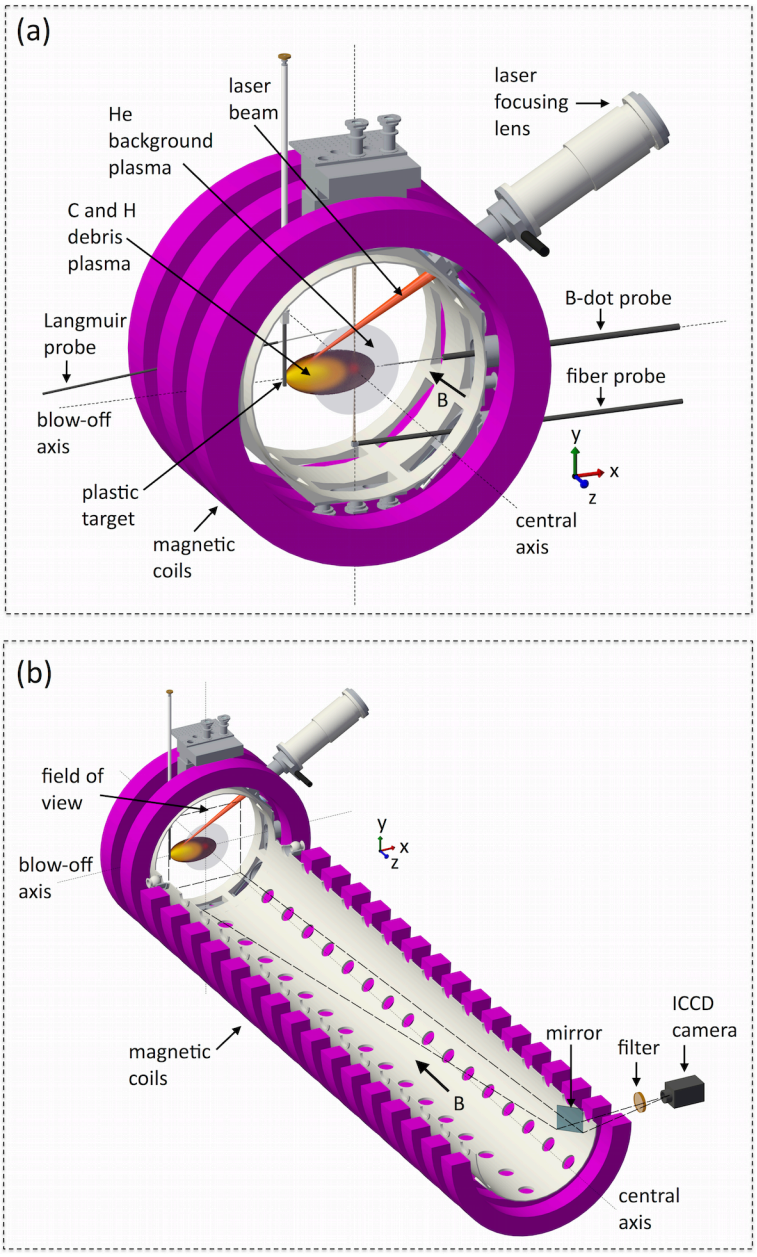

Figure 2.1: 3D schematic of the experimental setup, showing the utilized section of the LAPD and the quasi-perpendicular expansion of laser-produced C and H debris plasma through the preformed, magnetized He ambient plasma. In (a), a spectroscopic fiber probe, a magnetic flux probe, and a Langmuir probe monitor the debris-ambient interaction. In (b), a mirror placed far down the length of the machine allows for wavelength-filtered imaging of the blow-off plane.

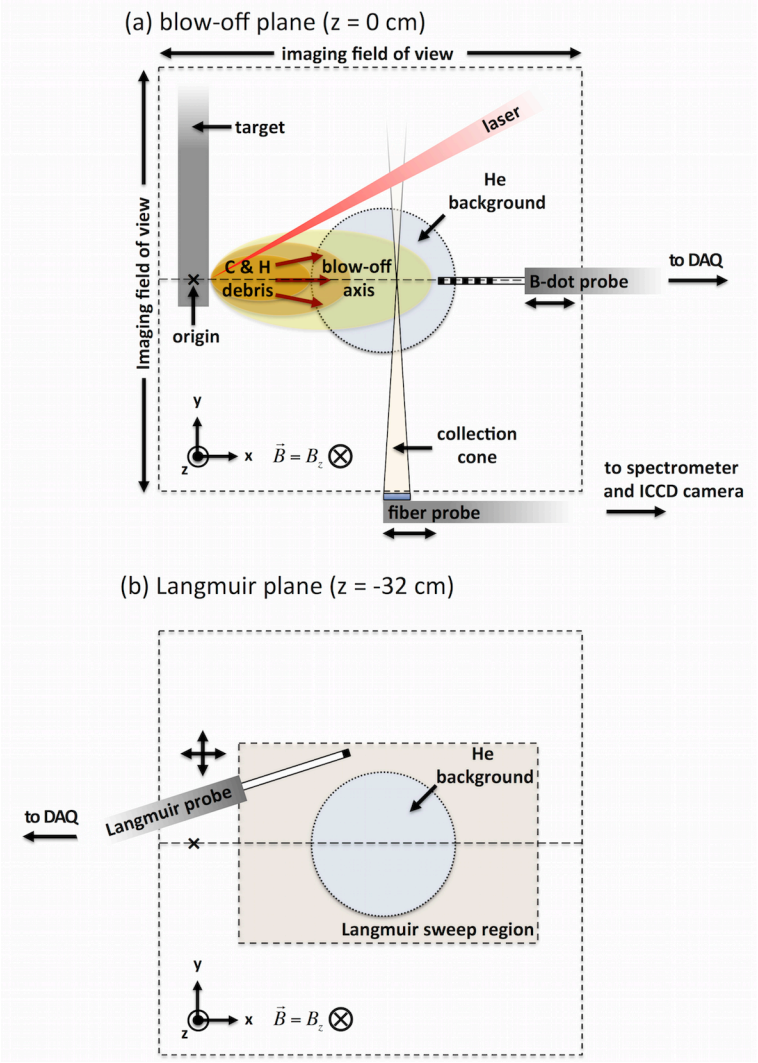

Figure 2.2: 2D schematic of the experimental setup. In the blow-off plane (a), the laser-produced debris plasma expands primarily in $+x$ through a magnetic field directed in $-z$. The debris passes through a region of neutral gas fill before reaching the He ambient plasma column. The spectroscopic fiber probe is focused on the blow-off axis and collects line-integrated emission along y. The magnetic flux probe takes measurements along the blow-off axis. Both probes can freely move along x. In the field of view of the wavelength-filtered images, the preformed He plasma column appears roughly in the center, the target falls near the left edge, and the magnetic field points into the page. In the plane one port downfield (b), the Langmuir probe freely moves along x and y and can scan the entire planar profile of the He ambient plasma.

(perpendicular to both the background magnetic field and the primary blow-off direction). A 75 mm focal length lens at the probe's collection end projects an image from the blow-off axis onto a linear array of 20 200-μm fused silica optical fibers. The linear array is oriented such that the imaged field of view spans ≈ 0.1 cm along x and ≈ 1.5 cm along z. However, the collected signal also contains defocused contributions along the entire line of sight. The fibers are coupled through a slit (50 μm or 100 μm) into a 0.75 m SPEX spectrometer containing a 3600 g/mm UV holographic grating. The spectrum is centered on the He II ion 468.6 nm line and projected onto a Princeton Instruments (PI) MAX 4 intensified charge coupled device (ICCD) camera, yielding a spectral resolution of ≈ 0.02 nm. Light emission collected during laser shots is typically time-integrated for $500 - 1000$ ns at various delays after the laser pulse, while emission collected from the unperturbed ambient plasma is typically time-integrated for 2 ms and averaged over as many as 25 cathode discharges. Calibration of the spectrometer, as well as a measurement of the instrumental broadening function, is accomplished via an Oriel pencil-style xenon (Xe) calibration lamp.

Second, a custom magnetic flux (or "B-dot") probe [22] consisting of 5 differentially-wound single-axis cores spaced at 1 cm increments is fixed at the blow-off axis and freely moves along x via a motorized 1D drive. The probe is oriented to measure the rate of change of the z component of the magnetic field ($\frac{dB_z}{dt}$), and the signals are sent through custom-built 150 MHz differential amplifiers and coupled into a 1.25 GHz, 10-bit digital acquisition system (DAQ). The measurements from each core are then numerically integrated, thus yielding B_z as a function of time at 5 consecutive positions from a single laser shot.

Third, a Langmuir probe [11] is fixed one port downfield from the target, corresponding to the plane $z = -32$ cm, and freely moves along both x and y via a motorized 2D drive. The probe is utilized for two purposes. First, in the unperturbed, ambient plasma, it performs a detailed planar scan while the bias voltage on the exposed conducting face is swept, yielding contours of the electron density and temperature in the plane perpendicular to the magnetic field. In this mode, the conducting face is oriented in the $-z$ direction (away from the LaB_6 cathode) in order to eliminate the effects of the primary ionizing electrons. Second, during

laser shots, the conducting face is oriented in the $+z$ direction (towards the target and debris plasma) and biased at fixed voltages of -20 V and -50 V in order to search for energetic electrons launched along the magnetic field at specific positions. The Langmuir probe output is also coupled into the DAQ.

Lastly, an aluminum mirror inside the LAPD, located at $z \approx 500$ cm, reflects light collected along the length of the machine through a port window. The reflected light then passes through a wavelength filter and is collected by a zoom lens attached to a PIMAX 4 ICCD camera. The lens is configured to bring the blow-off plane $z = 0$ cm into focus and yields a field of view of ≈ 60 cm along x and ≈ 60 cm along y. In the resulting images, the preformed plasma column of the LAPD appears roughly in the center, the target falls near the left edge, and the magnetic field points into the page. Two different wavelength filters are utilized in order to selectively image particular ion species. The first filter, centered at 468.6 nm with a 1 nm bandwidth, isolates He II ions via the 468.6 nm spectral line. The second filter, centered at 500 nm with a 10 nm bandwidth, is tilted slightly with respect to the optical axis in order to isolate C V ions via the 494.4 nm spectral line. Light emission collected during laser shots is time-integrated for 30 ns at various delays after the laser pulse.

2.3 Characterization of the Unperturbed Ambient Plasma

Prior to assessing the interaction of the explosive laser-produced debris with the preformed, magnetized background of the LAPD, it is necessary to characterize the He ambient plasma in its initial, unperturbed state. To this end, a Langmuir probe scan yields planar profiles of the electron density and temperature. The measurements are then utilized in combination with emission spectroscopy and collisional-radiative modeling to estimate the temperature of the He II ion charge state and to demonstrate the consistency of the Langmuir-measured electron temperature to the spectroscopic data.

2.3.1 Electron Density and Temperature

To obtain contours of the electron density and temperature of the He ambient plasma, the Langmuir probe performs a planar scan from $x = 5$ cm to $x = 55$ cm and from $y = -15$ cm to $y = 15$ cm at 1 cm increments. The exposed conducting face of the probe is oriented in the $-z$ direction (away from the LaB_6 cathode) in order to eliminate the effects of the primary ionizing electrons. At each position, the bias voltage on the conducting surface is swept while measuring the resulting current to it, and both the electron temperature and density follow from the response curve [11]. Though the Langmuir scan takes place in the plane one port downfield from the target ($z = -32$ cm), the measurements can also be assumed to characterize the blow-off plane ($z = 0$ cm), since variations in electron temperature and density along the magnetic field should be insignificant over such short distances. From the scan, it follows that the electron density profile of the plasma column has a full width at half-maximum (FWHM) of ≈ 20 cm. The peak density of $n_{e,max} \approx 7.2 \times 10^{12}$ cm^{-3} occurs at $(x, y) = (32, 6)$ cm, somewhat offset from the central axis of the LAPD. The electron temperature profile is more complex and involves several anomalous readings near the edges of the scan region. The peak temperature of $k_B T_{e,max} \approx 4.3$ eV occurs at $(x, y) = (36, 2)$ cm. The profiles are shown in Fig. 2.3.

2.3.2 He II Ion Temperature

An estimate of the He II ion temperature follows from the observed Doppler broadening in the He II 468.6 nm spectral line profile. To obtain the spectrum, the fiber probe collects line-integrated emission along y at $x = 30$ cm, through the central region of the ambient plasma column. Other broadening mechanisms, in addition to the Doppler effect, contribute significantly to the observed line shape and must be carefully taken into account in order to extract the ion temperature. Under the present experimental parameters, three primary features comprise the final measured line shape: instrumental broadening, fine structure splitting, and Doppler broadening. Other mechanisms, such as Zeeman splitting, pressure

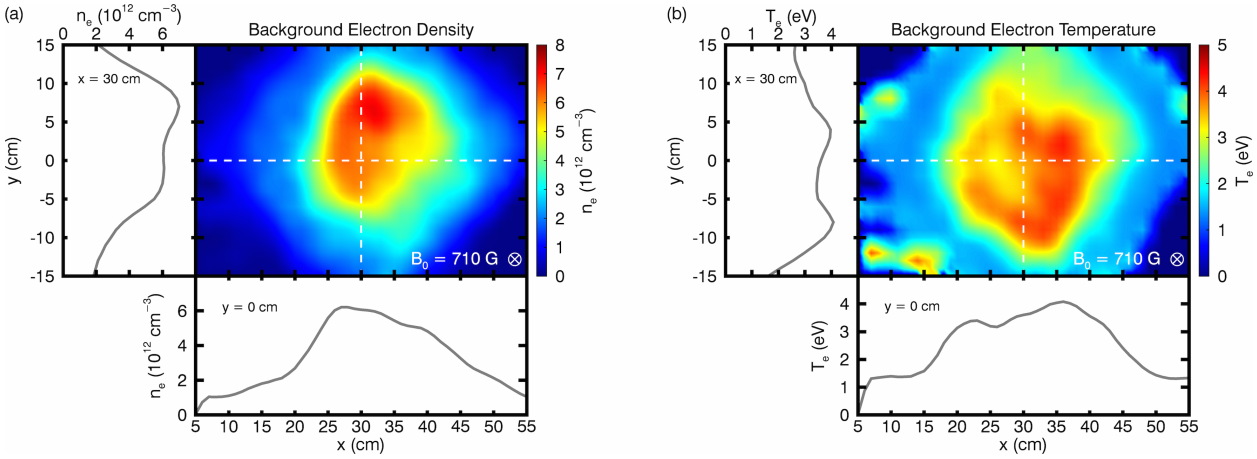

Figure 2.3: Results of the swept Langmuir probe scan, showing contours of (a) the electron density and (b) the electron temperature of the unperturbed He ambient plasma in the plane perpendicular to the magnetic field. The contours include line-outs along the axes $y = 0$ cm and $x = 30$ cm.

Stark broadening, and the natural line width, are well below the resolution limit of the spectroscopic setup.

Instrumental broadening results due to the finite spectrometer slit width and the spectral response of the diffraction grating. An experimental determination of the instrument function, denoted S_{inst}, consists of illuminating the fiber probe with a calibration source (in this case, a Xe lamp) and measuring the wavelength profile of a spectral line known to have an intrinsic width smaller than the resolution limit of the spectroscopic setup. In this way, any broadening in the observed profile corresponds purely to instrumental effects.

Fine structure corresponds to a small splitting of electronic energy levels of the same principal quantum number n due to electron spin-orbit coupling and relativistic corrections. The He II 468.6 nm spectral line, corresponding to spontaneous transitions from $n = 4$ to $n = 3$, thus actually consists of a closely spaced series of lines of generally different relative intensities. The fine structure profile, denoted S_{fs}, is obtained with the aid of the collisional-radiative simulation code PrismSPECT [38], which calculates the plasma ionization distribution and energy level populations, determines the transition powers of spectral

lines, and generates synthetic spectral profiles given the plasma temperature, density, and geometry as input. The present PrismSPECT simulation is carried out in non-local thermal equilibrium (non-LTE), steady-state mode, such that the ionization balance and energy level populations follow from the equilibrium solution to a large set of atomic rate equations rather than from the Saha and Boltzmann distributions. The computation utilizes a detailed He atomic model that contains rates corresponding to a variety of transition processes, including spontaneous emission, collisional excitation and de-excitation, and photoionization. Representative measurements from the Langmuir scan (Fig. 2.3) along the optical collection axis at $x = 30$ cm provide the plasma temperature (4 eV) and ion density (10^{13} cm^{-3}) inputs for the simulation.[1] The primary ionizing electrons from the 150 V LaB_6 cathode discharge are also incorporated by including a small non-thermal electron population (assumed to comprise 5% of the total electron density) with a directed kinetic energy of 150 eV. The calculation is performed in "zero width" geometry, implicitly assuming the plasma to be optically thin and ignoring non-local radiative transfer effects. The fine structure spectrum S_{fs} of the He II 468.6 nm line is then constructed directly from the calculated transition powers of the contributing components, using wavelengths from the NIST Atomic Spectral Database [34]. The PrismSPECT simulation parameters are summarized in Table 2.2.

Lastly, Doppler broadening results due to the thermal motion of the emitting population. Under the assumption of a Maxwellian distribution of the He II ion velocity component along the optical collection axis, the Doppler spectral profile, denoted S_{Dop}, can be expressed in wavelength space as

$$S_{Dop}(\lambda) = C \times \exp\left[-\frac{m_{He}c^2}{2k_B T_i}\left(\frac{\lambda - \lambda_c}{\lambda_c}\right)^2\right], \tag{2.1}$$

where λ is the independent variable indicating the wavelength, λ_c is the central wavelength of the spectral line, m_{He} is the He atomic mass, T_i is the He II ion temperature, k_B is

[1] PrismSPECT only provides a single input field for the plasma temperature and thus assumes that the ion and electron temperatures are equal, which is certainly not the case in the He ambient plasma of the LAPD. Moreover, while the electron density has been measured, the ion density can only be roughly inferred by making assumptions on the average plasma charge state. However, transition power ratios calculated by PrismSPECT have been shown to be virtually independent of ion temperature and density, and therefore the present inputs should yield an accurate simulation of the fine structure profile.

atomic model	He, all levels
simulation type	non-LTE, steady-state
plasma temperature	4 eV
ion density	10^{13} cm^{-3}
geometry	zero width
non-thermal electron energy	150 eV
non-thermal electron fraction	0.05

Table 2.2: PrismSPECT simulation parameters used to generate the fine structure profile S_{fs} of the He II 468.6 nm line.

Boltzmann's constant, c is the speed of light, and C is an arbitrary normalization constant. The FWHM of the Doppler contribution to the measured profile thus provides a direct diagnostic of the temperature via $\Delta\lambda_{FWHM} = \sqrt{\frac{8k_B T_i \ln 2}{m_{He}c^2}}\lambda_c$.

The total simulated spectral profile S_{tot} can be constructed via convolution of the experimentally measured instrument function S_{inst}, the PrismSPECT-generated fine structure profile S_{fs}, and the Maxwellian Doppler profile S_{Dop} of Eq. 2.1:

$$S_{tot} = S_{inst} \otimes S_{fs} \otimes S_{Dop}. \tag{2.2}$$

A spatially averaged estimate of the He II ion temperature then follows from a best fit of S_{tot} to the measured, line-integrated profile of the He II 468.6 nm line. Specifically, a Levenberg-Marquardt mean-squared error minimization algorithm varies the ion temperature T_i, which modifies S_{tot} through the Doppler contribution S_{Dop} in Eq. 2.2, until a best fit is achieved. Fig. 2.4 demonstrates the construction of the simulated spectrum S_{tot} from the three primary broadening mechanisms and compares the best fit to the measured profile. The fit reproduces the measured line shape, including the significant asymmetry in the profile attributed primarily to the fine structure, and yields a He II ion temperature of $k_B T_i = 0.3 \pm 0.2$ eV. Despite the large relative error resulting from the significant width of the instrument function relative to the Doppler broadening, the present analysis provides an

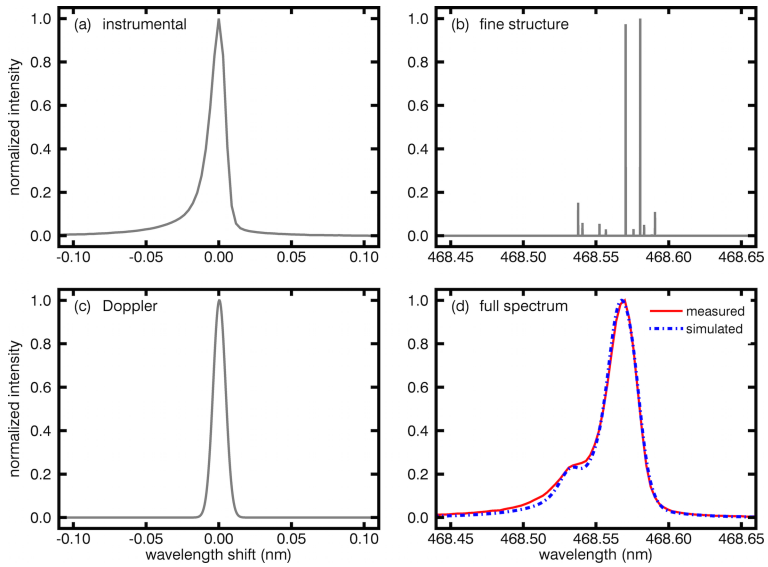

Figure 2.4: Construction of the best-fit simulated spectrum S_{tot} and comparison to the measured profile of the He II 468.6 nm spectral line. The simulated spectrum is generated via a convolution of (a) the experimentally measured instrument function S_{inst}, (b) the PrismSPECT-generated fine structure profile S_{fs}, and (c) the Maxwellian Doppler profile S_{Dop} of Eq. 2.1. A mean-squared error minimization algorithm varies the He II ion temperature T_i, which modifies the width of the Doppler contribution until a best fit (dashed blue line) to the measured profile (solid red line) is obtained in (d). The best fit reproduces the line shape, including the asymmetry resulting primarily from fine structure, and yields a He II ion temperature of $k_B T_i = 0.3 \pm 0.2$ eV.

improved upper bound on the He II ion temperature of $k_B T_i \leq 0.5$ eV.

2.3.3 Consistency of Electron Temperature and Spectral Line Shape

As demonstrated in the previous subsection, the spectral profile of He II 468.6 nm line depends on the He II ion temperature, which affects the Maxwellian Doppler broadening contribution. Less obviously, the line shape also depends on the electron temperature, which generally affects the relative intensities of the various lines comprising the fine structure profile through a modification of the energy level populations. The best-fit simulated spectrum

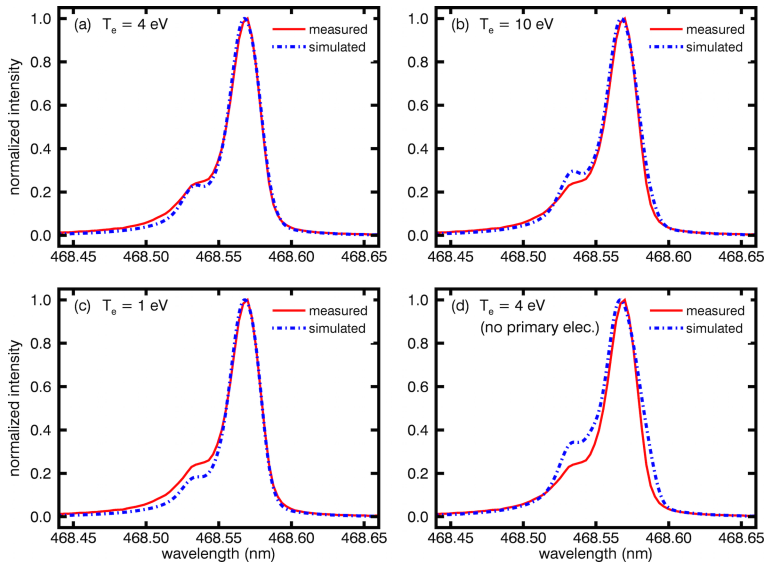

Figure 2.5: Comparison of the simulated (dashed blue line) and measured (solid red line) profiles of the He II 468.6 nm line for an electron temperature of (a) 4 eV, (b) 10 eV, (c) 1 eV, and (d) 4 eV without a non-thermal population fraction at 150 eV, at the best-fit ion temperature of $k_BTi = 0.3$ eV. The comparisons indicate a non-trivial dependence of line shape on electron temperature. The best fit in (a) requires both an electron temperature of ≈ 4 eV (consistent with the Langmuir scan) and a directed 150 eV primary ionizing electron population (consistent with the LaB_6 cathode discharge voltage).

that so effectively reproduces the measured line shape in Fig. 2.4 relies on a PrismSPECT-generated fine structure profile corresponding to a bulk electron temperature of 4 eV and a small non-thermal population with a directed kinetic energy of 150 eV, suggesting a consistency with Langmuir probe measurements of Fig. 2.3. To further investigate the effect of electron temperature on the simulated line shape, additional PrismSPECT calculations are carried out at 1 eV and 10 eV, and once again at 4 eV but without the non-thermal electron population, while keeping all other simulation parameters equivalent to Table 2.2. As before, the simulated fine structure profiles are convolved with the instrument function and the Doppler profile in order to construct the total spectra, with the He II ion temperature now held fixed at the best-fit value of $k_BTi = 0.3$ eV. Fig. 2.5 compares the simulated spectra to the measured profile, indicating a small but non-trivial modification of the line

shape resulting from a change in the relative intensities of the fine structure components at different electron temperatures. The comparisons indicate that the simulated spectrum fails to reproduce the measured profile as accurately at electron temperatures significantly higher (10 eV) or lower (1 eV) than those derived from the Langmuir scan ($\approx$ 4 eV) or without the inclusion of a 150 eV primary ionizing electron population corresponding to the LaB_6 cathode discharge. These results thus point out a consistency between the Langmuir measurements of electron temperature, the observed spectral profile of the He II 468.6 nm line, and collisional-radiative modeling in PrismSPECT.

2.4 Key Features of Debris-Ambient Interaction

When an energetic pulse from the Raptor laser irradiates the surface of the polyethylene $(C_2H_4)_n$ target, it generates explosive debris plasma consisting of various C and H charge states that expands quasi-perpendicular to the background magnetic field through the pre-formed He plasma column of the LAPD (see Fig. 2.1 and Fig. 2.2). The diagnostics monitoring the resulting debris-ambient interaction yield two principal observations. The first observation is the generation of energetic electrons, measured directly via a biased Langmuir probe and indirectly via wavelength-filtered imaging, which reveals a significant increase in the He II ion self-emission. Comparison of the filtered images to the magnetic field profile measured by a magnetic flux probe further supports the existence of energetic electrons. The second observation, of greater significance in the context of this work, is the acceleration of He II ions in response to the expanding debris along a trajectory qualitatively consistent with the laminar electric field (Eq. 1.9). This result comes directly from emission spectroscopy, which detects strong Doppler shifts in a He II ion spectral line.

2.4.1 The Laser-Produced Debris Plasma

In general, the laser-produced debris plasma is a complex, non-equilibrated system characterized by drastic spatial and temporal variations in density and temperature and mixtures

of ion charge states of differing velocity distributions. While Chapter 3 provides a more detailed, quantitative characterization of the debris plasma generated in this experiment, it is sufficient for the purposes of the present analysis to discuss the key features in a qualitative manner.

At $t = 0$ s, the impact of an intense Raptor laser pulse onto the polyethylene $(C_2H_4)_n$ target ionizes the surface atoms by rapidly ejecting the electrons. This generates strong ambipolar electric fields that rip C and H ions from the target surface. In these initial fields, the ions experience acceleration proportional to their charge state and inversely proportional to their mass. Thus, ions with higher charge-to-mass ratios attain faster average expansion speeds [7], though each charge state also generally develops a significant, roughly Gaussian velocity spread about the average [48]. Additionally, pressure anisotropies in the initial plasma drive the expansion primarily perpendicular to the target surface, forming an ellipsoidal cloud elongated along the blow-off axis [54]. The initial debris plasma thus consists of various fractions of all the ion charge states (H II, C II - C VII), which expand primarily along the blow-off axis with drifting Maxwellian velocity distributions segmented by the charge-to-mass ratios. This identifies H II and C VII as the fastest and second fastest ion charge states [59], respectively, and C II as the slowest.[2] The debris also typically contains neutral atoms and molecular species [32], which expand significantly slower than the ions.

The debris plasma, which can be considered as an essentially instantaneous explosion due to the insignificant duration of the laser pulse (5 ns) relative to time scales relevant to the experiment (~ 1 μs or longer), then expands quasi-perpendicular to the background magnetic field, passes through a region of neutral He gas fill, and eventually reaches and interacts with the performed He plasma column of the LAPD. The cross-field debris expansion results in the formation of a leading magnetic compression and a growing diamagnetic cavity, as illustrated in Fig. 1.1. Simultaneously, the debris density, which achieves near solid values

[2] An important implication of the segmented velocity distributions to the present experiment is that while the fastest ion charge states can certainly exceed the Alfvén speed of the ambient plasma ($M_A > 1$), the slower charge states may fail to do so ($M_A < 1$). Thus, in accordance with the theory outlined in Chapter 1, the physics corresponding to both regimes can potentially become important. This issue is considered further in Appendix A.

($\sim 10^{23}$ cm^{-3}) at the target surface immediately after ablation, rapidly drops by orders of magnitude as a function of both distance from the target and time after the laser pulse as the plasma expands.

2.4.2 Generation of Energetic Electrons

Measurements performed by several diagnostics jointly demonstrate that the debris-ambient interaction generates energetic electrons. Wavelength-filtered imaging provides initial, indirect evidence by revealing a considerable intensification of the He ambient plasma self-emission in response to the explosive debris. Fig. 2.6 compares images of C V debris ions and He II ambient ions collected via emission of the 494.4 nm and 468.6 nm spectral lines, respectively, at $t = 500$ ns, $t = 750$ ns, and $t = 1000$ ns. Due to the highly energized initial state of the debris plasma, the C V ions fluoresce intensely as they expand primarily along the blow-off axis, revealing flute-like structures at the leading edge.[3] However, the He II ions remain virtually undetectable in the short (30 ns) exposures until the leading edge of the C V ions sweeps through the ambient plasma, substantially increasing the He II 468.6 nm fluorescence in its wake.

Fig. 2.7 more clearly demonstrates the correspondence of the C V leading edge to the intensified He II region by comparing normalized intensity profiles of C V and He II along the blow-off axis from the images of Fig. 2.6. The profiles are superimposed on a line-out of the unperturbed ambient electron density of Fig. 2.3. In terms of half-maximums, the line-outs at $t = 500$ ns reveal that He II intensification initially develops between $x \approx 20$ cm and $x \approx 25$ cm, where the leading edge of C V first penetrates the He plasma column after crossing a region of neutral gas fill. As the debris continues to expand through the ambient plasma, the He II fluorescence boundary trails the C V leading edge and the volume of intensified He II grows. By $t = 750$ ns, the leading edges of both the C V and He II profiles reach $x \approx 30$ cm, and by $t = 1000$ ns, they reach $x \approx 35$ cm. Fig. 2.7 also compares the intensity line-outs

[3]Flute-like structures in laser-produced plasmas have been observed in a related experiment [16] and likely correspond to the large Larmor radius Rayleigh-Taylor (LLR) instability. This feature is not investigated further in the present analysis.

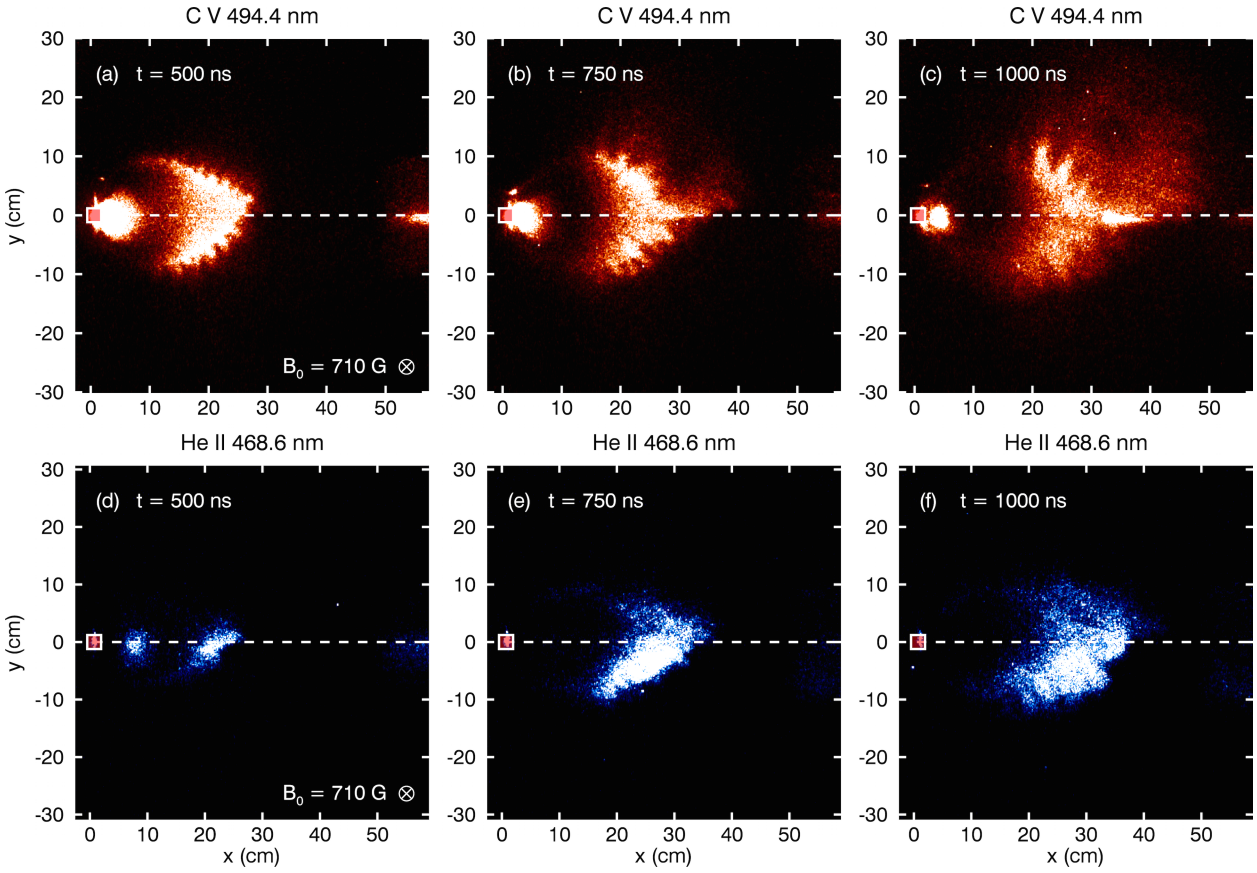

Figure 2.6: Wavelength-filtered images of C V debris ions (via the 494.4 nm line) and He II ambient ions (via the 468.6 nm line) at $t = 500$ ns, $t = 750$ ns, and $t = 1000$ ns, collected over 30 ns integration times. The superimposed squares mark the position where the laser pulse irradiates the target surface, the dashed lines denote the blow-off axis, and the magnetic field points into the page. Comparison of the images demonstrates that as the leading edge of the C V ions sweeps through the ambient plasma, the He II ion fluorescence considerably increases in its wake. The C V images also reveal flute-like structures at the leading edge that correspond to instabilities [16].

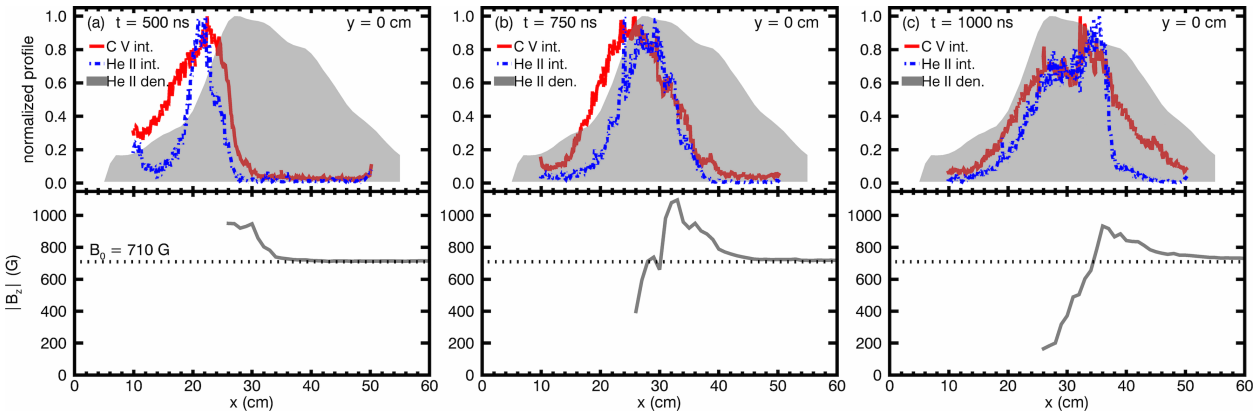

Figure 2.7: Normalized intensity profiles of C V (solid red line) and He II (dashed blue line) along the blow-off axis from the images of Fig. 2.6, superimposed on a line-out of the unperturbed ambient electron density (gray fill) of Fig. 2.3. The profiles are compared to the magnetic field's z component, also measured along the blow-off axis. The leading edges of the C V and He II emission profiles (at half-maximum) spatially correspond to each other and to the maximum of the magnetic compression.

to the spatial profiles of the magnetic field's z component, measured along the blow-off axis via a magnetic flux probe. At $t = 500$ ns, the magnetic compression becomes apparent at the edge of the measured region, where the field increases above the background value of $B_0 = 710$ G. The compression continues to propagate along the blow-off axis, and by $t = 750$ ns, the maximum reaches $x \approx 33$ cm. By $t = 1000$ ns, the maximum reaches $x \approx 36$ cm and the trailing diamagnetic cavity becomes more fully apparent. During this time interval, the maximum achieved compression ratio is $\frac{B_z}{B_0} \approx 1.5$. The comparison reveals that the leading edges (at half-maximum) of the C V and He II emission profiles approximately correspond to the peak magnetic compression. The correspondence also suggests that C V is the dominant debris charge state driving the cavity expansion, which is addressed in Chapter 3.

The C V ions become difficult to image for $t > 1500$ ns at the current exposure settings due to a rapid decline in the emission of the 494.4 nm line. However, the He II ions can be tracked much later in time due to the continued intense fluorescence at 468.6 nm. Fig. 2.8 shows a series of He II images at various times between $t = 1500$ ns and $t = 13000$ ns.

In addition to demonstrating the prolonged duration of intensified emission, the time series also reveals that between $t = 1500$ ns and $t = 5000$ ns the fluorescing He II cloud becomes significantly displaced from its original position, ending up centered at roughly $(x, y) \approx (50, 10)$ cm. After $t = 5000$ ns, the cloud remains mostly stationary though intensified emission continues until at least $t = 13000$ ns.

Fig. 2.9 more clearly demonstrates the significant displacement of the fluorescing cloud by comparing normalized profiles of the He II intensity along the blow-off axis from three of the images of Fig. 2.8 to a line-out of the unperturbed ambient electron density of Fig. 2.3. At $t = 2000$ ns, the debris plasma has swept through and intensified the entire ambient plasma column and the fluorescence profile roughly matches the density line-out. By $t = 5000$ ns, however, the peak of He II emission has moved from $x \approx 30$ cm to $x \approx 50$ cm, a displacement of ≈ 20 cm from the peak density position of the unperturbed plasma. At $t = 8000$ ns, peak fluorescence continues at $x \approx 50$ cm. Fig. 2.9 also compares the intensity line-outs to the spatial profiles of the magnetic field's z component along the blow-off axis. At $t = 2000$ ns, most of the He II emission region falls within the diamagnetic cavity. The front edge of the cavity continues to propagate forward while the back end begins to collapse, and by $t = 5000$ ns, the magnetic field returns to its background value everywhere except for a ≈ 15 cm interval centered at $x \approx 45$ cm. Correspondingly, the strongest He II emission only persists in the region where the cavity remains and decreases significantly in the region where the cavity collapses. By $t = 8000$ ns, the remainder of the cavity collapses but fluorescence continues in the vicinity of the final cavity position. Together, Fig. 2.8 and Fig. 2.9 thus demonstrate three features: the prolonged duration of intensification, the correspondence of the peak emission to the position of the diamagnetic cavity, and the displacement of the fluorescing cloud. The displacement provides preliminary evidence of debris-ambient coupling, which will be addressed in more detail in the following subsection.

To understand how the imaged intensification indirectly indicates energetic electrons, it is necessary to recall that emission of the 468.6 nm spectral line requires a population of He II ions to spontaneously transition from energy levels with principal quantum number

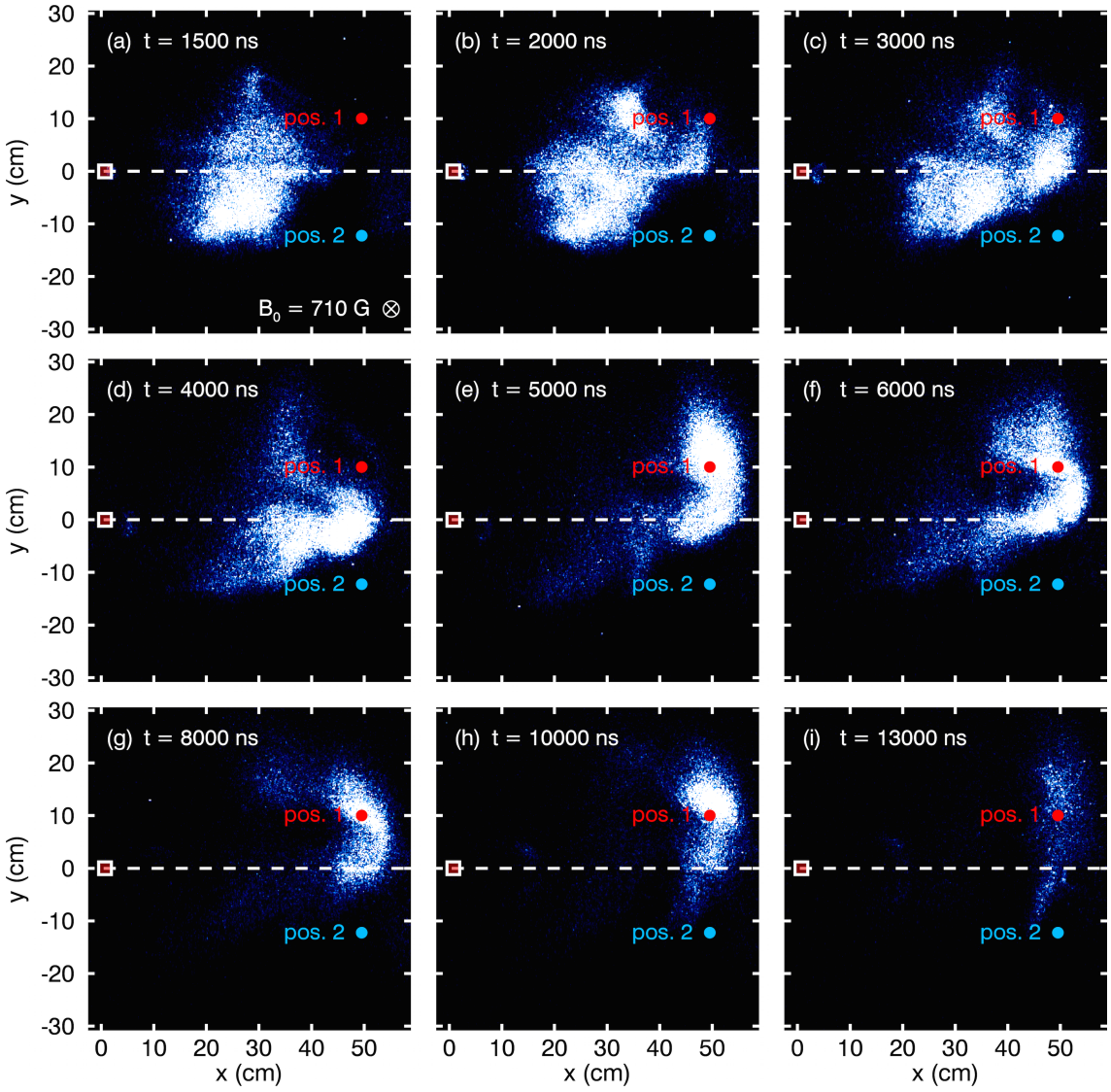

Figure 2.8: Wavelength-filtered images of He II ambient ions (via the 468.6 nm line) at various times between $t = 1500$ ns and $t = 13000$ ns, collected over 30 ns integration times. The superimposed squares mark the position where the laser pulse irradiates the target surface, the dashed lines denote the blow-off axis, and the magnetic field points into the page. The red dots marked "pos. 1" and the blue dots marked "pos. 2" denote the field-aligned positions of the biased Langmuir probe in Fig. 2.10. The images demonstrate the prolonged duration of intensified He II ion emission and reveal a significant displacement of the fluorescing cloud between $t = 1500$ ns and $t = 5000$ ns.

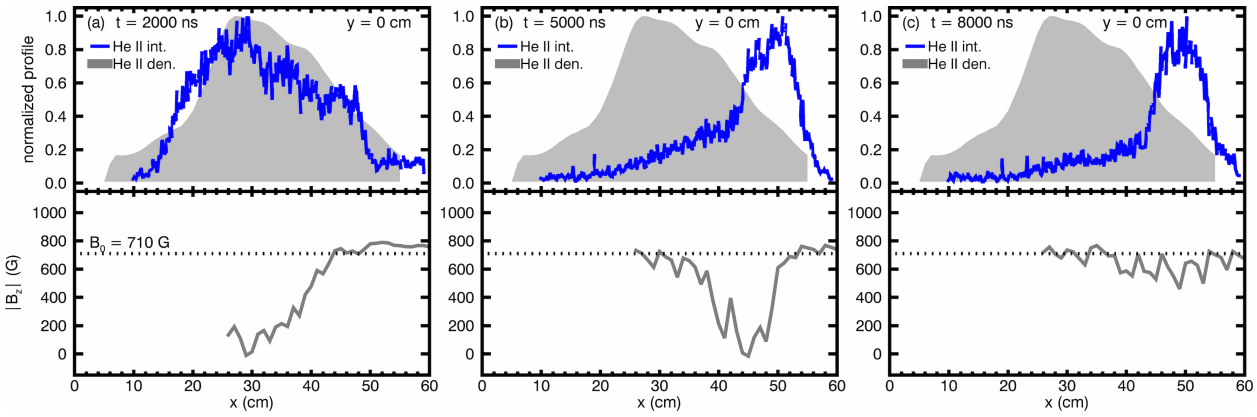

Figure 2.9: Normalized intensity profiles of He II (solid blue line) along the blow-off axis from three of the images of Fig. 2.8, superimposed on a line-out of the unperturbed ambient electron density (gray fill) of Fig. 2.3. The profiles are compared to the magnetic field's z component, also measured along the blow-off axis. First, the comparisons demonstrate a significant (≈ 20 cm) displacement of the peak He II emission from the peak density position of the unperturbed plasma. Second, the comparisons show that the peak He II emission follows the diamagnetic cavity and then persists in the vicinity of the final cavity position after its collapse. The small oscillations in the magnetic field profiles likely correspond to a shadowing issue of the 5-tip magnetic flux probe.

$n = 4$ to $n = 3$. Intensified fluorescence therefore requires a significant increase in the $n = 4$ population. A detailed analysis of the PrismSPECT simulations carried out in Section 2.3 indicates that the primary mechanism populating $n = 4$ is excitation from the predominant ground state $n = 1$ via collisions with free electrons, which must have a kinetic energy of at least 51 eV in order to overcome the energy difference between the two levels [34]. Intensification thus necessitates an increase in the population of free electrons with energies ≥ 51 eV. Moreover, as demonstrated in Fig. 2.8, increased fluorescence persists for at least 13 μs even though the characteristic spontaneous decay time from $n = 4$ to $n = 3$ is only ~ 10 ns. This indicates that energetic electrons continually repopulate the $n = 4$ level for the entire duration of intensification.

The spatial correspondence of the magnetic field profiles to the intensity line-outs further

supports the existence of energetic electrons. Due to their low mass, the electrons are effectively tied to the magnetic field lines and cannot propagate along the blow-off axis. For example, an energetic electron with a directed cross-field kinetic energy of 100 eV (roughly corresponding to a speed of $v_\perp = 6000$ km/s) in the background magnetic field $B_0 = 710$ G has a gyro-radius of only $\rho_e = \frac{m_e c v_\perp}{e B_0} \approx 0.05$ cm. However, the electrons can freely stream within the diamagnetic cavity, where the magnetic field is expelled. This is consistent with both Fig. 2.7, which shows virtually no intensification ahead of the magnetic compression, and Fig. 2.9, which demonstrates that the peak He II emission follows the diamagnetic cavity and survives only in the region where the cavity finally collapses. In other words, the intensified region of He II follows the energetic electrons, which are confined by the evolving magnetic field profile.

Measurements from a biased Langmuir probe provide direct confirmation of energetic electrons. The conducting face of the Langmuir probe is oriented in the $+z$ direction (towards the target and debris plasma) and biased at -20 V and at -50 V. Two positions are selected for measurement based on the He II images of Fig. 2.8. The first position, denoted via the red dot at $(x, y) = (50, 10)$ cm, places the probe in a field-aligned configuration to the intensified He II cloud. The second position, denoted via the blue dot at $(x, y) = (50, -13)$ cm, sets the probe outside of the fluorescence region. Fig. 2.10 compares the Langmuir probe readings to the intensities from the images of Fig. 2.8 at the two positions as a function of time. At the position field-aligned to the fluorescing cloud, the Langmuir probe detects a significant electron current (represented by the measured negative voltage), first at a bias of -20 V and then -50 V. The fact that electrons reach the conducting face despite the negative biases indicates directed electron kinetic energies along the magnetic field of > 50 eV, consistent with the indirect inference from intensification of the He II 468.6 nm line. Moreover, the temporal duration of energetic electrons corresponds to the He II emission. The negative voltage first becomes apparent between $t = 4$ μs and $t = 5$ μs, just as the fluorescing cloud arrives at the probe position in Fig. 2.8, and persists until $t \approx 12$ μs, consistent with the significant intensity drop between $t = 10$ μs and $t = 13$ μs. By contrast, at the position

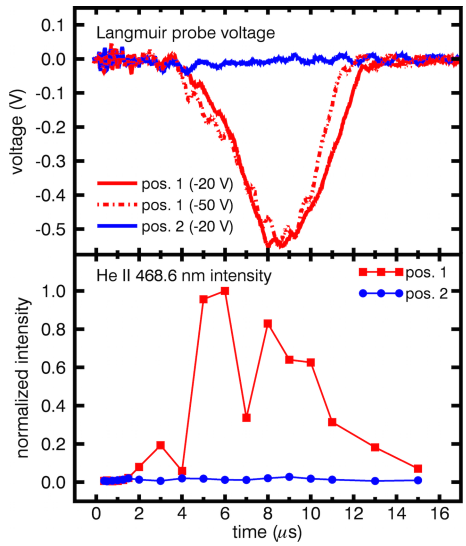

Figure 2.10: Comparison of biased Langmuir probe measurements to imaged He II 468.6 nm intensities as a function of time at the two positions marked in Fig. 2.8. In a field-aligned configuration to the fluorescing He II cloud ("pos. 1"), the Langmuir probe detects an electron current at biases of −20 V (solid red line) and −50 V (dashed red line), consistent with the observed He II intensification (red squares). Outside of the fluorescing cloud ("pos. 2"), the Langmuir probe does not detect any electrons at a bias of −20 V (solid blue line), and correspondingly, no increase in He II emission is observed (blue circles).

outside of the fluorescence region, the Langmuir probe does not measure any electron current even at a bias of −20 V, indicating that maximum electron energies in this region cannot exceed 20 eV.

Biased Langmuir probe readings, wavelength-filtered images, and magnetic flux probe measurements thus jointly demonstrate the generation of energetic electrons (> 50 eV). As verified by Thomson scattering measurements [48] under similar conditions in the LAPD, initially hot electrons in the laser-produced debris cool rapidly, reaching thermal background levels less than 5 cm from the target and well within 1 μs after ablation. In combination with the fact that the debris density becomes comparable to the ambient density by the time the debris reaches the ambient plasma column (see Chapter 3), the detection of energetic electrons as far as ≈ 50 cm from the target and later than 10 μs after the laser pulse in the

present experiment indicates that they are generated by the debris-ambient interaction and cannot simply correspond to a hot remnant of the initial debris plasma. While the exact mechanisms responsible for the fast electron population remain to be determined, the present data points to several hypotheses. The correspondence of the He II intensification boundary to the magnetic compression in Fig. 2.7 suggests that energetic electrons first develop within the azimuthal current layers (i.e., the diamagnetic current). Recalling that the diamagnetic current forms, in part, due to azimuthal $\vec{E} \times \vec{B}$ drifts of the electrons, the drift kinetic energy may be sufficient to excite ground state He II ions and create the observed increase in fluorescence. However, as demonstrated in Fig. 2.9, continued He II fluorescence long after the collapse of the diamagnetic cavity indicates that the diamagnetic current cannot account for the energetic electrons later in time. Another potential source of fast electrons is an instability driven by the slower, sub-Alfvénic ($M_A < 1$) charge states of the expanding debris plasma. Appendix A considers this possibility in further detail.

2.4.3 He II Ion Acceleration

Of greatest significance in the context of this work is the observed acceleration of He II ions in response to the explosive debris plasma along a trajectory qualitatively consistent with the laminar electric field (Eq. 1.9). A preliminary indication that the debris pushes the ambient plasma already appears in Fig. 2.8 and Fig. 2.9, which demonstrate a displacement of the fluorescing He II cloud in both the $+x$ and $+y$ directions, consistent with the gyration expected of ions moving through a magnetic field directed in $-z$. Direct observation of He II ion motion in response to the debris follows from spectroscopic measurements of Doppler shifts in the He II 468.6 nm line. The considerable intensification of this line caused by energetic electrons has a highly beneficial consequence, as it allows for significantly better time resolution in the spectroscopic measurements. In fact, with the present apparatus, the intensified plasma yields sufficient signal-to-noise ratios with integration times of only 500 ns, a vast improvement over the ~ 1 ms exposures required in the unperturbed ambient plasma. This allows for sub-gyro-period resolution (a He II ion in the background magnetic field

$B_0 = 710$ G has a gyro-period of $T = \frac{2\pi m_{He} c}{eB_0} \approx 4$ μs), a crucial aspect of the measurements to follow.

Fig. 2.11 shows wavelength profiles of the He II 468.6 nm line measured via the fiber probe at three different positions and time intervals. The corresponding filtered images of He II ion fluorescence illustrate the spatiotemporal configuration of the spectroscopic measurements by highlighting the optical collection axis of each wavelength profile. The fiber probe tracks the intensified cloud along x while collecting line-integrated emission along y. For comparison, spectra are also collected in the unperturbed ambient plasma. The first wavelength profile, measured at $x = 30$ cm and time-integrated from $t = 500$ ns to $t = 1000$ ns, demonstrates strong asymmetric Doppler broadening predominantly towards lower wavelengths (a blue shift). Recalling that the fiber probe points in the $+y$ direction (see Fig. 2.2), the observed blue shift denotes that the intensified He II ions initially acquire a velocity component in $-y$. The blue shift of $\Delta\lambda = -0.25 \pm 0.02$ nm (measured at half-maximum of the profile) corresponds to a velocity component along y of $v_y = \frac{c\Delta\lambda}{\lambda_c} = -160 \pm 13$ km/s, where λ_c is the central wavelength of the transition at 468.6 nm and c is the speed of light. This is almost two orders of magnitude faster than the root-mean-square speed of ≈ 3 km/s derived from the ≈ 0.3 eV He II ion temperature within the unperturbed ambient plasma. The second wavelength profile, measured at $x = 45$ cm and time-integrated from $t = 4000$ ns to $t = 4500$ ns, reveals a strong asymmetric Doppler broadening predominantly towards higher wavelengths (a red shift). This indicates that, farther from the target and later in time, intensified He II ions change direction and develop a large velocity component in $+y$. In fact, the red shift of $\Delta\lambda = 0.22 \pm 0.02$ nm (measured at half-maximum of the profile) corresponds to a y velocity component of $v_y = 141 \pm 13$ km/s, similar in magnitude but opposite in direction to the first measurement. The third wavelength profile, measured at $x = 47.5$ cm and time-integrated from $t = 9000$ ns to $t = 10000$ ns, demonstrates a reduced and roughly symmetric Doppler broadening about the line center. This suggests that at late times the intensified He II ions no longer have a directed drift but remain heated above the unperturbed ambient ion temperature. Approximating the line shape to a Maxwellian yields

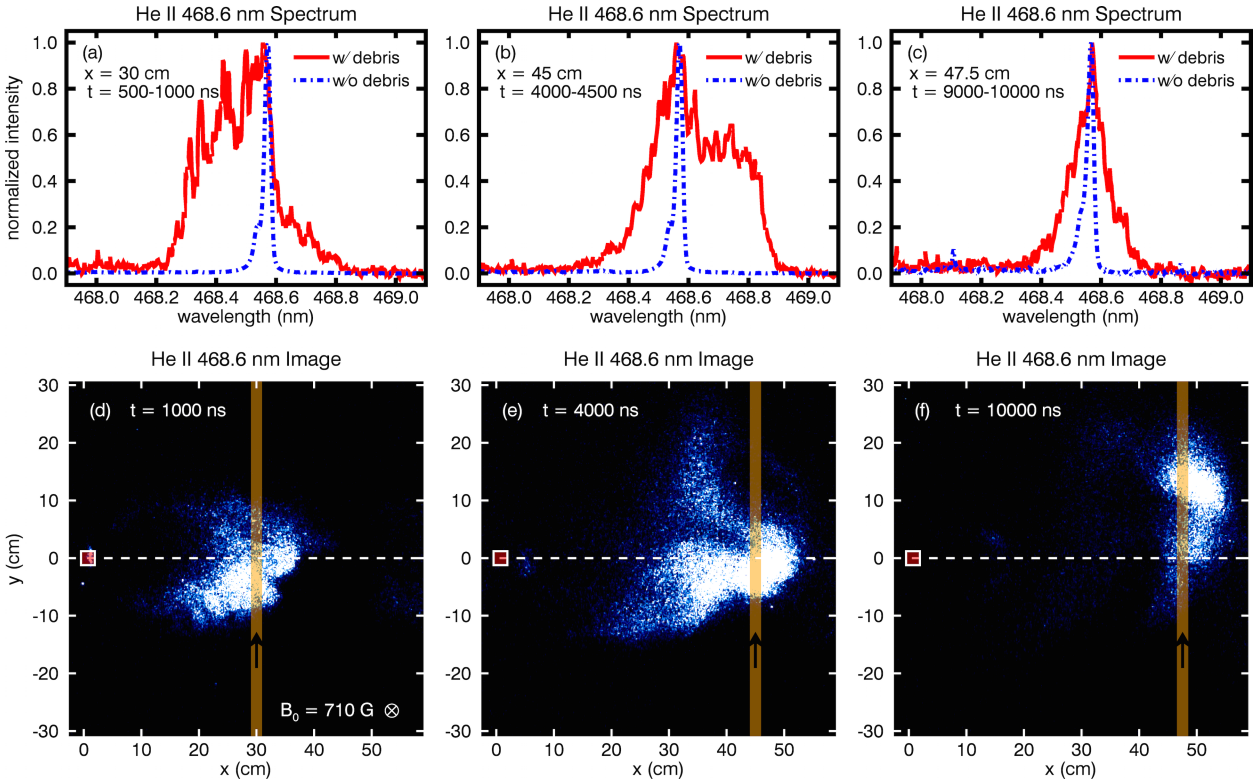

Figure 2.11: Wavelength profiles of the He II 468.6 nm spectral line measured in the presence of explosive debris (solid red line) and in the unperturbed ambient plasma (dashed blue line) at three different positions and time intervals. The corresponding filtered images of He II fluorescence highlight the optical collection axis (thick orange line) of the spectroscopic measurements. In (a), asymmetric Doppler broadening predominantly towards the lower wavelengths (blue shift) indicates an initial acceleration of He II ions in the $-y$ direction. In (b), asymmetric Doppler broadening predominantly towards the higher wavelengths (red shift) demonstrates that, farther from the target and later in time, the He II ions change direction and now move primarily in $+y$. In (c), reduced and roughly symmetric Doppler broadening suggests that at late times the He II ions no longer have a directed drift but remain somewhat heated above the unperturbed ambient ion temperature.

root-mean-square speeds along y of ≈ 30 km/s, about an order of magnitude faster than the unperturbed ambient plasma.

The spectroscopic measurements of Fig. 2.11 indicate that the explosive debris plasma, which expands primarily in the $+x$ direction along the blow-off axis, initially pushes the He II ambient ions in the $-y$ direction, transverse to its expansion. Moreover, later in time and farther from the target, the He II ions appear to reverse their direction and move in $+y$. In order to interpret these counterintuitive results, it is useful to first establish the parameter regime of the present experiment by considering the Alfvénic Mach number M_A, the electron beta β_e, and the debris ion-ambient ion collisional mean free path λ_{da}. To estimate M_A, a characteristic debris expansion speed V_d is determined from the time of flight of the magnetic compression. From Fig. 2.7, the peak compression reaches $x \approx 30$ cm at $t = 500$ ns, corresponding to $V_d \approx 600$ km/s. Under the assumption of He II as the dominant ambient charge state, the ion density n_a is well-represented by $n_{e,max} \approx 7.2 \times 10^{12}$ cm^{-3} from the peak electron density measurement of Fig. 2.3, and the Alfvén speed in the ambient plasma at the background magnetic field of $B_0 = 710$ G calculates to $v_A = \frac{B_0}{\sqrt{4\pi n_a m_{He}}} \approx 290$ km/s. The resulting Mach number of $M_A \equiv \frac{V_d}{v_A} \approx 2$ thus confirms a super-Alfvénic ($M_A > 1$) expansion. An estimate of β_e similarly follows from the peak electron density $n_{e,max}$ and the peak electron temperature $k_B T_{e,max} \approx 4.3$ eV of Fig. 2.3, yielding $\beta_e \equiv \frac{8\pi n_{e,max} k_B T_{e,max}}{B_0^2} \approx 0.0025$. Near the target surface, β_e can significantly exceed this value due to the much higher debris plasma densities and temperatures. However, as the debris cloud expands out to the ambient plasma column, the electrons cool rapidly [48] and densities drop to values comparable to the ambient plasma (see Chapter 3). Thus, the debris-ambient interaction satisfies the condition $\beta_e \ll 1$. Finally, the debris ion-ambient ion multi-Coulomb collisional mean free path λ_{da} [33] follows from the expression

$$\lambda_{da} = \left(\frac{m_d V_d^2}{2}\right)^2 \left[\pi \left(1 + \frac{m_d}{m_a}\right) Z_d Z_a n_a e^4 \ln \Lambda\right]^{-1}, \tag{2.3}$$

where m_d and m_a are the debris and ambient ion masses, Z_d and Z_a are the debris and ambient ion charge states, V_d is the debris ion speed, n_a is the ambient ion density, e is the elementary charge, and $\ln \Lambda$ is the Coulomb logarithm. For a C V debris ion streaming

at 600 km/s through He II ions at the peak ambient density from Fig. 2.3, Eq. 2.3 yields $\lambda_{da} \approx 50$ km, indicating that at the scales of the experiment size D, the debris ion-ambient ion interaction is collision-less ($\lambda_{da} \gg D$).

Recalling the theoretical considerations outlined in Chapter 1, momentum and energy transfer from debris ions to ambient ions in the super-Alfvénic ($M_A > 1$), low electron beta ($\beta_e \ll 1$), collision-less ($\lambda_{da} \gg D$) regime that characterizes the present experiment is mediated primarily by the laminar electric field:

$$\vec{E}_{lam} = -\frac{1}{en_e}\vec{\nabla}p_e - \frac{1}{4\pi en_e}\vec{B} \times \left(\vec{\nabla} \times \vec{B}\right) - \frac{1}{en_e c}\sum\nolimits_i \vec{J_i} \times \vec{B}. \tag{1.9}$$

Fig. 2.12 illustrates that the asymmetric Doppler broadening observed in Fig. 2.11 is, in fact, qualitatively consistent with He II ion acceleration via the third term of Eq. 1.9, which arises due to cross-field ion currents. Along the blow-off axis, the various charge states comprising the expanding debris plasma set up ion current densities $\vec{J_i}$ primarily directed in $+x$. Due to the magnetic field directed in $-z$, the cross-field ion current term accordingly generates a laminar electric field pointing in the $-\vec{J_i} \times \vec{B}$ direction, which corresponds to $-y$ at the blow-off axis. As the explosive debris first crosses into the ambient He plasma column, this electric field immediately pushes a population of intensified He II ions in the $-y$ direction, accelerating them from the initial thermal root-mean-square speeds of only ≈ 3 km/s to a directed drift of up to ≈ 160 km/s towards the collecting fiber probe. This produces the observed asymmetric Doppler broadening towards the lower wavelengths measured at $x = 30$ cm. The subsequent motion of the He II ions cannot be determined exactly without resorting to computational methods (see Chapter 3) due to the complex temporal and spatial dependencies of both the laminar electric field and the magnetic field. Nevertheless, the basic trajectory can be inferred from the orientation of the magnetic field, directed in $-z$. If debris expansion persists and the laminar electric field continues to point in $-y$, the He II ions will follow a cycloid-like path with a guiding center drift in the $+x$ direction (an $\vec{E} \times \vec{B}$-like drift). On the other hand, if the debris expansion stops and the laminar electric field expires, the He II ion motion will resemble simple gyration due to the magnetic Lorentz force. In either one of these scenarios, a population of He II ions initially accelerated in $-y$ must eventually

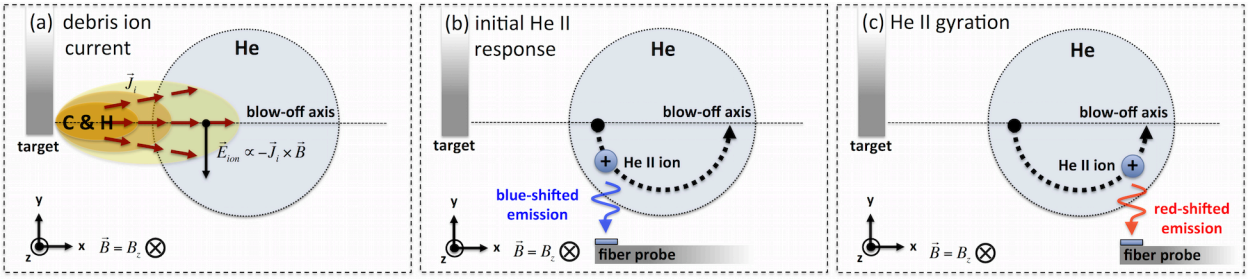

Figure 2.12: Illustration demonstrating the consistency of the cross-field ion current term of Eq. 1.9 to the measured asymmetric Doppler broadening in Fig. 2.11. In (a), the debris plasma sets up ion currents directed primarily in $+x$ as it expands along the blow-off axis through the magnetic field in $-z$, generating an electric field in $-y$. In (b), as the debris enters the ambient plasma column, the electric field accelerates He II ions in $-y$ and towards the fiber probe, resulting in the measured blue shift. In (c), the accelerated He II ions follow either an $\vec{E} \times \vec{B}$-like drift trajectory or a simple gyration motion until the magnetic field redirects the ions in $+y$ at some distance farther along x, resulting in the measured red shift.

redirect to $+y$ some distance farther along x. This distance should be on the order of the gyro-radius, which, for an accelerated He II ion at $v_y \approx 160$ km/s in the background field of $B_0 = 710$ G, corresponds to $\rho_a = \frac{m_{He} c v_y}{e B_0} \approx 10$ cm. This accounts for the asymmetric Doppler broadening towards the higher wavelengths measured later in time at $x = 45$ cm, which indicates a directed drift of up to ≈ 140 km/s away from the collecting fiber probe. Fig. 2.12 also demonstrates that the measured blue shifts and red shifts of Fig. 2.11 rely on sub-gyro-period time resolution, which allows the spectra to capture the motion of the ions before they significantly change direction in the magnetic field.

Doppler spectroscopy thus directly indicates He II ion acceleration in response to the explosive debris plasma along a trajectory consistent with the laminar electric field. However, two issues in the present analysis must be acknowledged. First, in Fig. 2.11, the predominantly blue-shifted spectrum at $x = 30$ cm also includes a small red-shifted component, and the predominantly red-shifted spectrum at $x = 45$ cm includes a blue-shifted component. This indicates that the qualitative interpretation in Fig. 2.12, based on the cross-field ion

current term of Eq. 1.9, is incomplete. In accordance with the theoretical arguments of Chapter 1, the contribution of the electron pressure gradient term relative to the magnetic pressure gradient and tension term scales as β_e and can be ignored since $\beta_e \ll 1$. However, the contribution of the cross-field ion current term to the magnetic pressure gradient and tension term scales as M_A. The current value of $M_A \approx 2$ thus indicates that the magnetic pressure gradient and tension term can contribute significantly to He II ion acceleration in the vicinity of the magnetic compression and diamagnetic cavity edge, in conjunction with the cross-field ion current term. As will be demonstrated in Chapter 3, magnetic pressure gradients do in fact account for the red shift measured at $x = 30$ cm. Second, it is important to note that the measured Doppler-broadened spectra of Fig. 2.11 do not necessarily account for the entire He II ion velocity distribution. As demonstrated in Fig. 2.7 and Fig. 2.9, the energetic electrons that cause intensification in the He II 468.6 nm line are confined by the magnetic profile and follow the diamagnetic cavity, surviving only in the final position of cavity collapse at late times. However, due to their much larger mass, He II ions with sufficient velocity can stream ahead of the magnetic compression and move outside of the region of trapped energetic electrons, where they no longer experience collisional excitation and become optically invisible. The measured spectrum thus only corresponds to the velocity distribution of the *intensified* He II ions. As will be shown in Chapter 3, the full velocity distribution likely contains much faster He II ions that do not fluoresce. This effect can also potentially explain the significantly reduced Doppler broadening measured at $x = 47.5$ cm, which might result from the fact that the faster ion population has moved out of the region of energetic electrons and no longer contributes to the measured spectrum.

The next logical step of achieving a quantitative comparison between the measured spectra and laminar coupling theory poses various challenges. For one, the spectra of Fig. 2.11 are spatially integrated along y and temporally integrated for 500 ns or more, providing enough time for He II ions to stream in and out of the collection axis from various parts of the fluorescing cloud. The sampled velocity distribution is thus complex and highly non-Maxwellian, as made evident by the asymmetric, flat-topped line shapes of the Doppler-broadened spec-

tra. Additionally, the electric and magnetic fields that determine the He II ion response are complicated functions of position and time. Thus, a quantitative comparison between measurements and theory demands a computational approach. This is detailed in Chapter 3.

2.5 Summary

This chapter has reported the key observations from a laboratory investigation of the super-Alfvénic, quasi-perpendicular expansion of laser-produced C and H debris plasma through preformed, magnetized He ambient plasma, utilizing a unique experimental platform at UCLA that combines the LAPD and Phoenix facilities. A variety of sophisticated diagnostics, including emission spectroscopy, wavelength-filtered imaging, a magnetic flux probe, and a Langmuir probe, have monitored the debris-ambient interaction, yielding the following important results:

- Swept Langmuir probe measurements in the plane perpendicular to the magnetic field indicate that the unperturbed He ambient plasma column has a FWHM of ≈ 20 cm, a peak electron density of $\approx 7.2 \times 10^{12}$ cm^{-3}, and a peak electron temperature of ≈ 4.3 eV.

- Spectroscopic measurements of the He II 468.6 nm line in the unperturbed He ambient plasma, in combination with collisional-radiative modeling in PrismSPECT, yield a line-integrated He II ion temperature estimate of 0.3 ± 0.2 eV at $x = 30$ cm. The spectral line shape is also found to be consistent with a bulk Maxwellian electron temperature of ≈ 4 eV (as measured by the Langmuir sweep) and a small primary ionizing population with a directed kinetic energy of 150 eV (as expected from the cathode discharge).

- Wavelength-filtered imaging observes a considerable and long-lasting (> 10 μs) intensification of the He II 468.6 nm emission in response to the explosive debris plasma, indirectly indicating the continual generation of electrons with directed kinetic energies

> 51 eV. Comparison to magnetic flux probe measurements suggests that the energetic electrons develop within the magnetic compression as it sweeps through the ambient plasma and remain confined primarily within the diamagnetic cavity until its collapse. Displacement of the fluorescing He II cloud by at least ≈ 20 cm from the initial peak density position provides preliminary evidence of debris-ambient coupling.

- Biased Langmuir probe measurements at positions field-aligned to the intensified He II region confirm the long-lasting (> 10 μs) duration of electrons with kinetic energies > 50 eV. The energetic electron generation mechanisms may correspond to the diamagnetic current or to the development of instabilities late in time.

- Of greatest import in the context of this work, spectroscopic measurements of the He II 468.6 nm line reveal significant, asymmetric Doppler broadening in response to the explosive debris plasma. A closer analysis indicates an initial acceleration of He II ions in the direction transverse to the debris plasma expansion and a subsequent gyration in the magnetic field. He II ion velocity components of up to ≈ 160 km/s are measured, nearly two orders of magnitude faster than the root-mean-square speed of ≈ 3 km/s in the unperturbed ambient plasma. The inferred trajectory is found to be qualitatively consistent with the cross-field ion current term of the laminar electric field (Eq. 1.9), which is expected to be the dominant debris-ambient coupling mechanism in the super-Alfvénic ($M_A > 1$), low electron beta ($\beta_e \ll 1$), collision-less ($\lambda_{da} \gg D$) regime that characterizes the present experiment.

CHAPTER 3

Analysis of Laminar Collision-less Coupling at Early Times

3.1 Overview

As detailed in Chapter 2, the laboratory investigation of super-Alfvénic, quasi-perpendicular expansion of laser-produced carbon (C) and hydrogen (H) debris plasma through preformed, magnetized helium (He) ambient plasma yields evidence of laminar collision-less coupling. Specifically, strong Doppler shifts in a He II ion spectral line directly indicate acceleration along a trajectory qualitatively consistent with an initial impulse due to the cross-field ion current term of the laminar electric field (Eq. 1.9). While the qualitative correspondence is promising, a validation of laminar coupling theory also requires a quantitative comparison, a task that poses various challenges. For one, the measurements that indicate He II ion acceleration rely on spatially and temporally integrated spectra that sample a large population of ions of differing trajectories, resulting in highly complex velocity distributions and atypical Doppler-broadened profiles. Additionally, the electric and magnetic fields that determine the He II ion response are generally complicated functions of position and time. A meaningful quantitative comparison of the observed spectral line shapes to laminar coupling theory therefore demands a computational approach that can calculate the theoretical trajectories and velocities of a distribution of He II ions in the spatially and temporally varying electric and magnetic fields.

Ignoring resistivity due to collisions, the evolution of a He II ion (charge number $Z = 1$)

subjected to arbitrary electric and magnetic fields follows from the Lorentz force,

$$\frac{d^2\vec{r}\,(t)}{dt^2} = \frac{d\vec{v}\,(t)}{dt} = \frac{e}{m_{He}}\left(\vec{E}\,(\vec{r},t) + \frac{\vec{v}\,(t)}{c} \times \vec{B}\,(\vec{r},t)\right), \tag{3.1}$$

where $\vec{r}\,(t)$ and $\vec{v}\,(t) = \frac{d\vec{r}(t)}{dt}$ are the ion position and velocity, $\vec{E}\,(\vec{r},t)$ and $\vec{B}\,(\vec{r},t)$ are the spatially and temporally dependent electric and magnetic fields evaluated at the current position of the ion, and m_{He}, e, and c are the ion mass, elementary charge, and the speed of light, respectively. Given the initial conditions, a solution to Eq. 3.1 yields the trajectory $\vec{r}\,(t)$ and velocity $\vec{v}\,(t)$. However, this requires detailed spatiotemporal knowledge of $\vec{E}\,(\vec{r},t)$, which is not measured in the present experiment, and $\vec{B}\,(\vec{r},t)$, which is only diagnosed along the blow-off axis. Theoretical considerations from Chapter 1 indicate that in the super-Alfvénic ($M_A > 1$), low electron beta ($\beta_e \ll 1$) environment of this investigation, $\vec{E}\,(\vec{r},t)$ can be computed from the expression for the laminar electric field. Thus,

$$\vec{E}\,(\vec{r},t) = \vec{E}_{lam} = -\frac{1}{en_e}\vec{\nabla}p_e - \frac{1}{4\pi en_e}\vec{B} \times \left(\vec{\nabla} \times \vec{B}\right) - \frac{1}{en_e c}\sum\nolimits_i \vec{J_i} \times \vec{B}, \tag{1.9}$$

where the magnetic field $\vec{B} = \vec{B}\,(\vec{r},t)$, the ion current densities $\vec{J_i} = \vec{J_i}\,(\vec{r},t)$, the electron density $n_e = n_e\,(\vec{r},t)$, and the electron pressure $p_e = p_e\,(\vec{r},t)$ are functions of position and time evaluated at the current location of the He II ion. However, because the spatiotemporal behavior of these parameters is also unknown from experiment, a calculation of $\vec{E}\,(\vec{r},t)$ via Eq. 1.9 cannot be easily performed. Determination of the He II ion trajectory and velocity therefore necessitates a reasonable prediction of $\vec{E}\,(\vec{r},t)$ and $\vec{B}\,(\vec{r},t)$, despite the absence of experimental data.

For this purpose, a number of recent computational studies [14, 13, 63] have utilized two-dimensional "hybrid codes," which treat the ions as particles and the electrons as a massless thermal fluid, in order to simulate the interaction of explosive debris plasma with magnetized ambient plasma. Given various initial input parameters (including plasma species, charge states, density profiles, expansion speeds, magnetic fields, and temperatures), the hybrid code first calculates $\vec{E}\,(\vec{r},t)$ via the fluid electron momentum equation (analogous to Eq. 1.9) and advances the debris and ambient ions over a small time step via the Lorentz force

(Eq. 3.1). The motion of the debris and ambient ions modifies $\vec{J}_i(\vec{r},t)$ and $n_e(\vec{r},t)$ (by quasi-neutrality), and the Maxwell-Faraday equation ($\vec{\nabla} \times \vec{E}(\vec{r},t) = -\frac{1}{c}\frac{\partial \vec{B}(\vec{r},t)}{\partial t}$) evolves $\vec{B}(\vec{r},t)$ from its initial configuration, which in turn updates $\vec{E}(\vec{r},t)$. Repetition of this procedure over numerous time steps thus yields a self-consistent solution of the ion motion and fields. However, a fundamental difficulty arises in connecting the simulation results to the actual experimental data. In the two-dimensional simulations, the density of the expanding debris plasma generally decreases with time as $\sim \frac{1}{t^2}$, while in the three-dimensional experiment, the debris density drops as $\sim \frac{1}{t^3}$. Because $\vec{E}(\vec{r},t)$ crucially depends on the plasma density (through $\vec{J}_i(\vec{r},t)$ and $n_e(\vec{r},t)$ in Eq. 1.9), the expectation is that the simulated electric fields and ion trajectories differ significantly from the experimental observations. Recently, the hybrid code has been extended into three spatial dimensions, which resolves this discrepancy. However, the computational intensity of fully three-dimensional calculations demands super-computer processing power.

The motivation of the present chapter is therefore to develop an alternative, simplified computational approach that takes into account the three-dimensional nature of the experiment without demanding the high processing power of the three-dimensional hybrid code. In contrast to the methodology of the hybrid code, which evolves the plasma parameters and fields together, the general approach here imposes predetermined spatiotemporal models of the plasma parameters, allowing for a simple calculation of $\vec{E}(\vec{r},t)$, $\vec{B}(\vec{r},t)$, and the resulting He II ion response. The computational methods developed in this chapter, while extremely useful to the present analysis, also contain significant limitations and should therefore not be viewed as a replacement to the three-dimensional hybrid code. Instead, the present approach provides a complimentary tool that can potentially allow for a rough investigation of parameter space prior to committing to a computationally (and temporally) intensive three-dimensional hybrid simulation.

In this chapter, Section 3.2 utilizes various experimental data in combination with radiation-hydrodynamic simulations of the laser-produced debris plasma in order to develop heuristic models for $n_e(\vec{r},t)$, $\vec{J}_i(\vec{r},t)$, $\vec{B}(\vec{r},t)$, and $p_e(\vec{r},t)$, allowing for a calculation of $\vec{E}(\vec{r},t)$ in the

blow-off plane ($z = 0$ cm) via Eq. 1.9. The models take into account the three-dimensional expansion of the debris, though their validity relies on a number of simplifying assumptions and requires "early times," before the debris plasma expends a substantial amount of its initial kinetic energy or undergoes significant gyration in the magnetic field. In the subsequent analysis, four different versions of the heuristic models (one version corresponding to the actual experimental parameters and three intentionally unrealistic variations) are applied in order to investigate the self-consistency of the computational approach. Section 3.3 employs the derived models in order to assess the spatiotemporal behavior of $\vec{E}(\vec{r},t)$ in relation to $\vec{B}(\vec{r},t)$ and the expanding debris plasma. The modeled $\vec{E}(\vec{r},t)$ and $\vec{B}(\vec{r},t)$ are then used to simulate the initial response of a distribution of He II ion test particles in the blow-off plane via the Lorentz force (Eq. 3.1), and the resulting He II ion motion is assessed. Section 3.4 then compares the computational results to the experimental data. Specifically, synthetic Doppler-broadened spectral line shapes constructed from the simulated He II ion trajectories and velocities are compared to the spectroscopic measurements, providing a quantitative evaluation of laminar coupling theory. Additionally, the validity of the computation is tested against the Maxwell-Faraday equation and energy conservation. Finally, Section 3.5 summarizes the important results. Most importantly, the present analysis concludes that the Doppler-broadened spectrum indicating initial He II ion acceleration in response to the explosive debris is quantitatively, as well as qualitatively, consistent with the laminar electric field of Eq. 1.9. Together, the results of Chapter 2 and Chapter 3 thus constitute an experimental validation of laminar collision-less coupling theory in a reproducible laboratory environment.

3.2 Derivation of Plasma Parameter Models

A theoretical computation of the electric field $\vec{E}(\vec{r},t)$ via Eq. 1.9 requires knowledge of the spatiotemporally dependent electron density $n_e(\vec{r},t)$, the total ion current density $\sum_i \vec{J}_i(\vec{r},t)$, the magnetic field $\vec{B}(\vec{r},t)$, and the electron pressure $p_e(\vec{r},t)$. As these parameters are not

determined experimentally (with the exception of $\vec{B}(\vec{r},t)$, diagnosed only along the blow-off axis), this section develops heuristic models by utilizing the available experimental data, radiation-hydrodynamic simulations, and several simplifying assumptions. The models are then combined via Eq. 1.9 into an expression for $\vec{E}(\vec{r},t)$ in the blow-off plane ($z = 0$ cm), where considerable simplifications arise due to symmetry.

3.2.1 Model for Electron Density

The interaction of explosive debris plasma with ambient magnetized plasma results in a very complex evolution of the electron density $n_e(\vec{r},t)$. However, the behavior of individual ion charge states is generally much more tractable. Quasi-neutrality dictates that the electrons continually redistribute themselves in order to locally match the total charge density of all the debris ion species (each of density $n_d(\vec{r},t)$ and charge number Z_d) and ambient ion species (each of density $n_a(\vec{r},t)$ and charge number Z_a), such that

$$n_e(\vec{r},t) \cong \sum\nolimits_d Z_d n_d(\vec{r},t) + \sum\nolimits_a Z_a n_a(\vec{r},t). \tag{3.2}$$

The present analysis thus derives $n_e(\vec{r},t)$ by developing models for $n_d(\vec{r},t)$ and $n_a(\vec{r},t)$.

A reasonable model of the density $n_d(\vec{r},t)$ of each debris ion charge state requires a detailed spatiotemporal knowledge of the laser-produced plasma, which generally consists of a mixture of various charge states (H II, C II - C VII) with velocity distributions segmented by the charge-to-mass ratios, as well as neutral atoms and molecular species that expand significantly slower than the ions. However, two-dimensional hybrid code simulations have demonstrated that H ions do not effectively transfer momentum and energy to the ambient plasma due to their relatively low mass and extremely fast expansion speeds. Therefore, as a simplification, the subsequent derivation of $n_d(\vec{r},t)$ considers only ion charge states C II - C VII and ignores neutral atoms and molecules.

In order to characterize the laser-produced debris plasma, the one-dimensional, Lagrangian radiation-hydrodynamics code HELIOS [39] is utilized to simulate the laser-target interaction. Given various inputs, including the target material equation-of-state (generated

target material	graphite (C)
geometry	planar
laser wavelength	1053 nm
laser pulse length	5 ns (Gaussian)
laser intensity	1 TW/cm^2

Table 3.1: HELIOS simulation parameters used characterize the evolution of the laser-produced debris plasma.

by the PROPACEOS code), the parameters of the incident laser pulse, and the expansion geometry, the code computes the evolution of the resulting laser-produced debris via fluid equations of motion with pressure contributions from ions, electrons, magnetic fields, and radiation. The HELIOS output utilized here follows directly from a comprehensive characterization of laser-produced plasmas found in [52], which also provides an experimental validation of the code and discusses the input parameters and computational methods in further detail. Motivated by the more extensive availability of simulations utilizing the graphite (C) equation of state, the results used here assume a graphite target rather than the polyethylene plastic material employed in the experiment. However, as HELIOS predicts a nearly identical composition and evolution of the C component of the debris plasma for both target types, this should be inconsequential. The simulation assumes an average laser intensity of 1 TW/cm^2 over a 5 ns Gaussian pulse at a wavelength of 1053 nm, modeled after Raptor.[1] The simulated plasma evolves in a planar geometry, such that the input laser intensity profile homogeneously irradiates an infinite flat target surface and the debris expands only along the surface normal. Table 3.1 summarizes the simulation configuration.

The HELIOS output contains numerous plasma parameters, including the spatially and temporally dependent densities of each debris ion charge state. However, the HELIOS-calculated densities necessarily differ by orders of magnitude from the actual values in the

[1]The original HELIOS computations actually assume a 25 ns Gaussian pulse, based on the configuration of Raptor in previous experiments. In order to account for the 5 ns pulse length of the present experiment, the output is manually adjusted via simple scaling laws found in [52].

experiment due to the assumption of a planar geometry, which fails to represent the three-dimensional debris expansion. While HELIOS can also perform calculations in cylindrical and spherical geometries, neither of these scenarios accurately reflects the observed ellipsoidal expansion of the laser-produced debris. Thus, instead of using the directly calculated densities, the model developed here utilizes the HELIOS-predicted total number of ablated ions N_{tot}, the relative population fractions of the ion charge states χ_d, and the velocity distributions of each ion species, which are then combined with an independently obtained model of the debris expansion geometry in order to derive $n_d(\vec{r}, t)$. The computed values of these parameters at $t = 500$ ns (roughly corresponding to the time when significant debris-ambient interaction begins in the experiment) are listed in the "Run 1 (3D)" portion of Table 3.2, shown at the end of this section. The results show that the laser pulse ablates $\sim 10^{17}$ total ions, which distribute amongst all the charge states C II - C VII. The majority of the ions correspond to C V and C IV, which constitute $\approx 40\%$ and $\approx 30\%$ of the total ion population, respectively. The velocity distributions are well-described by drifting Maxwellians of the form

$$f_d(v) = C_d \exp\left[-\frac{\left(v - \bar{V}_d\right)^2}{2\sigma_d^2}\right], \tag{3.3}$$

where $\bar{V}_d$ is the mean drift speed that increases with charge state, σ_d is the standard deviation corresponding to the spread in the distribution, and C_d is an arbitrary normalization constant. The fastest C VII charge state expands at ≈ 1000 km/s on average. Fig. 3.1 graphically illustrates the velocity distributions of each debris ion species.

Wavelength-filtered imaging of the explosive laser-produced debris plasma motivates a simple model of the expansion geometry, which is then combined with the computed parameters of Table 3.2 in order to derive $n_d(\vec{r}, t)$. Fig. 3.2 shows C V ions imaged in the blow-off plane via the 494.4 nm spectral line at $t = 625$ nm, $t = 750$ ns, and $t = 875$ ns. The images utilize the experimental setup of Chapter 2 but without the generation of the He ambient plasma column, thus showing debris expansion only into the magnetized vacuum of the LAPD. The expansion geometry follows from the C V fluorescence boundary in the

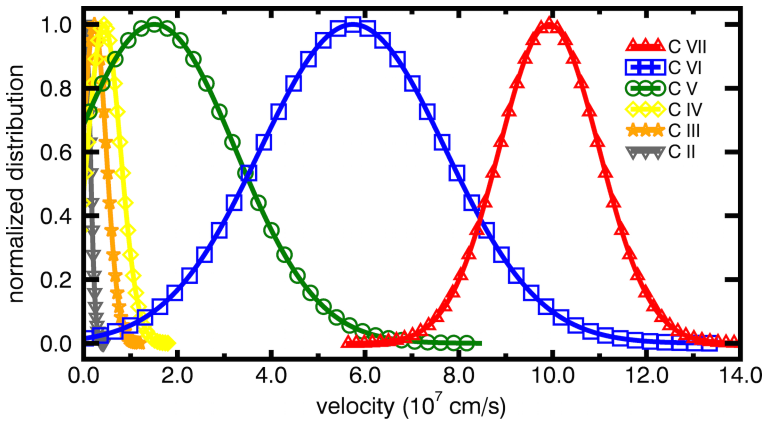

Figure 3.1: HELIOS-simulated velocity distributions of the debris ions corresponding to the input parameters of Table 3.1 at $t = 500$ ns.

blow-off plane, well-represented in polar co-ordinates by a heuristic "teardrop" function:

$$r(\theta, t) = r_0(t) \exp(-|\theta|/\theta_0) \cos\theta, -\frac{\pi}{2} \leq \theta \leq \frac{\pi}{2}. \tag{3.4}$$

In Eq. 3.4, $r = \sqrt{x^2 + y^2}$ is the distance from the origin to the fluorescence boundary in the blow-off plane, $\theta = \arctan(y/x)$ is the angle with respect to the blow-off axis, $r_0(t)$ is the time-dependent maximum extent of the fluorescence along the blow-off axis, and θ_0 is a free parameter that varies the teardrop shape. A qualitative best fit of Eq. 3.4 is obtained at $\theta_0 = 1.5$ rad and superimposed on the images of Fig. 3.2. As the cusp position represented by $r_0(t)$ evolves from $x \approx 35$ cm to $x \approx 40$ cm between $t = 625$ ns and $t = 875$ ns, Eq. 3.4 continues to provide a consistently good fit at the optimal fixed value of θ_0.

While the images of Fig. 3.2 characterize the expansion geometry in the blow-off plane perpendicular to the magnetic field, a corresponding assessment of the parallel plane is not available in the present experiment. The fully three-dimensional expansion model developed here thus assumes symmetry. Specifically, the debris is presumed to expand into the symmetric volume swept by rotating the teardrop outline of Fig. 3.2 about the blow-off axis.[2] Under this assumption, Eq. 3.4 can be easily converted from polar co-ordinates to spherical

[2]See [8] or Appendix B for a discussion of how the planar laser-induced fluorescence (PLIF) diagnostic in future experiments can potentially improve upon the expansion model utilized here by providing three-dimensional imaging of the debris plasma.

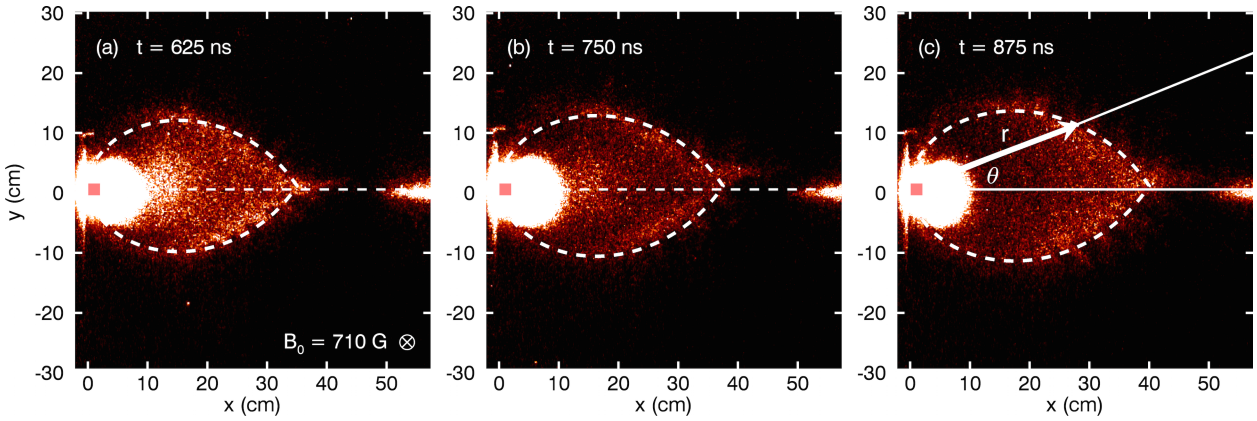

Figure 3.2: Wavelength-filtered images of C V debris ions (via the 494.4 nm line) at $t = 625$ ns, $t = 750$ ns, and $t = 875$ ns, collected over 30 ns integration times. The C V ions expand into the magnetized vacuum of the LAPD. The superimposed squares mark the position where the laser pulse irradiates the target surface, the dashed lines denote the blow-off axis, and the magnetic field points into the page. The overlaid teardrop profiles correspond to Eq. 3.4 at the optimized value of $\theta_0 = 1.5$ rad.

co-ordinates:

$$r\left(\theta,\phi,t\right) = r_0\left(t\right)\exp\left(-\theta/\theta_0\right)\cos\theta, 0 \leq \theta \leq \frac{\pi}{2}, 0 \leq \phi \leq 2\pi. \tag{3.5}$$

In Eq. 3.5, $r = \sqrt{x^2+y^2+z^2}$ now represents the distance from the origin to the fluorescence boundary in three-dimensional space, $\theta = \arctan\left(\sqrt{y^2+z^2}/x\right)$ continues to measure the angle with respect to the blow-off axis but is no longer confined to the blow-off plane, and ϕ measures the angle of the projection of r in the yz plane. Symmetry about the blow-off axis follows from the fact that r does not explicitly depend on ϕ. The geometric dependence of the expansion speed simply follows from differentiating Eq. 3.5 with respect to time,

$$v\left(\theta,\phi,t\right) = \frac{\partial r\left(\theta,\phi,t\right)}{\partial t} = v_0\left(t\right)\exp\left(-\theta/\theta_0\right)\cos\theta, \tag{3.6}$$

where $v_0\left(t\right)$ is the generally time-dependent speed along the blow-off axis. Unsurprisingly, the speed decreases with increasing θ, falling to zero at $\theta = \frac{\pi}{2}$.

In order to easily combine the HELIOS-computed parameters of Table 3.2 with the teardrop geometry derived from wavelength-filtered imaging into an expression for $n_d\left(\vec{r},t\right)$, it

is necessary to make the crucial simplifying assumption of a ballistic debris plasma expansion. Under the ballistic assumption, debris ions radially stream at constant velocity from the origin $\vec{r} = 0$, where the laser irradiates the target at $t = 0$. This has two important implications. First, a debris ion with velocity $\vec{v}$ at time t is located at position $\vec{r} = \vec{v}t$. Second, in Eq. 3.6, $v_0(t) = v_0$ is a constant and the expansion speed only depends on the direction indicated by θ. A reasonable postulate for the plasma distribution function of each debris ion charge state as a function of position $\vec{r}$, velocity $\vec{v}$, and time t is thus

$$f_d(\vec{r}, \vec{v}, t) = C_d \delta^3(\vec{r} - \vec{v}t) \exp\left[-\frac{\left(v - \bar{V}_d \exp(-\theta/\theta_0)\cos\theta\right)^2}{2\sigma_d^2}\right]. \tag{3.7}$$

Eq. 3.7 is effectively the drifting Maxwellian distribution of Eq. 3.3 with a δ-function that enforces the ballistic property $\vec{r} = \vec{v}t$. To account for the teardrop expansion geometry, the HELIOS-simulated average drift speed $\bar{V}_d$ is modulated by the angular dependence of Eq. 3.6. Thus, the actual average drift speed is only equal to $\bar{V}_d$ along the blow-off axis ($\theta = 0$) but decreases with increasing θ, falling to zero at $\theta = \frac{\pi}{2}$. The HELIOS-simulated velocity spread σ_d is assumed not to have an angular dependence.

Integration of Eq. 3.7 over all velocity space collapses the δ-function and yields the density $n_d(\vec{r}, t)$ of each debris charge state:

$$n_d(\vec{r}, t) = \int_v f_d(\vec{r}, \vec{v}, t)\, \mathrm{d}^3\vec{v} = \frac{C_d}{t^3} \exp\left[-\frac{\left(r - \bar{V}_d t \exp(-\theta/\theta_0)\cos\theta\right)^2}{2\sigma_d^2 t^2}\right]. \tag{3.8}$$

As expected, $n_d(\vec{r}, t)$ is characterized by a drifting Gaussian profile. The peak expands at speed $\bar{V}_d$ along the blow-off axis ($\theta = 0$) but moves slower with increasing θ, remaining stationary at $\theta = \frac{\pi}{2}$. The standard deviation $\sigma_d t$ grows linearly in time as the dispersion in the ion velocities causes an increasing spatial spread in the population. Simultaneously, the peak amplitude drops as $\frac{1}{t^3}$ due to the three-dimensional expansion. The contour of maximum density at any given time produces the teardrop shape superimposed in Fig. 3.2. The normalization constant C_d is obtained by integrating Eq. 3.8 over all space and equating the result to the total number of ions within each charge state, which follows from the product of the HELIOS-simulated total number of ablated ions N_{tot} and the fraction of each charge

state χ_d. Thus,

$$N_{tot}\chi_d = \int_r n_d\left(\vec{r},t\right) \mathrm{d}^3\vec{r}. \tag{3.9}$$

The integration in Eq. 3.9 is performed numerically, utilizing the values of $\bar{V}_d$, σ_d, χ_d, and N_{tot} listed in Table 3.2 and the optimized parameter $\theta_0 = 1.5$ rad. The integration range in spherical co-ordinates only spans $0 \leq \theta \leq \frac{\pi}{2}$ (corresponding to the positive side of the blow-off axis), implicitly assuming that all of the ablated ions expand away from the target surface. The numerically computed values of the constants C_d for each debris ion charge state are also listed in Table 3.2.

It is important to note that the ballistic assumption utilized in this derivation necessarily neglects any debris ion acceleration or deceleration. The expression for $n_d\left(\vec{r},t\right)$ in Eq. 3.8 is therefore only valid early in the evolution of the debris plasma, before it expends a substantial amount of kinetic energy through coupling to the ambient plasma and the expulsion of the magnetic field, and before the ions gyrate significantly due to the Lorentz force. Section 3.4 investigates the validity of the early-time ballistic assumption in further detail.

In order to derive the total electron density $n_e\left(\vec{r},t\right)$ from quasi-neutrality (Eq. 3.2), it is also necessary to develop a model for the density $n_a\left(\vec{r},t\right)$ of each ambient ion charge state. However, an exact determination of the spatiotemporal evolution of $n_a\left(\vec{r},t\right)$ necessitates knowledge of the ambient plasma response to the explosive debris. This, in turn, requires the electric and magnetic fields $\vec{E}\left(\vec{r},t\right)$ and $\vec{B}\left(\vec{r},t\right)$, the very quantities that the present analysis eventually aims to derive. Escaping the vicious circle thus requires a simplifying assumption. As shown in Fig. 2.3 of Chapter 2, a Langmuir sweep of the unperturbed ambient plasma yields a profile of the electron density in the plane perpendicular to the magnetic field. Because the measured densities do not vary significantly along the magnetic field over length scales relevant to the experiment, the Langmuir data in fact defines a volumetric electron density function, denoted $n_{e,meas}\left(\vec{r}\right)$. By quasi-neutrality, $n_{e,meas}\left(\vec{r}\right)$ equates to the total ambient ion charge density, as it is measured prior to the arrival of the debris plasma. Invoking the assumption that the explosive debris does not significantly disturb the ambient

density profile when it first arrives, the equivalence continues to hold and thus

$$\sum\nolimits_a Z_a n_a\left(\vec{r},t\right) \cong n_{e,meas}\left(\vec{r}\right). \tag{3.10}$$

Eq. 3.10 provides a good starting point for the ambient ion density as it is based directly on experimental data. However, the assumption of a static profile limits its validity. Section 3.3 attempts an improvement that takes into account the perturbation of the ambient density profile by the explosive debris.

Substitution of Eq. 3.8 for the debris ion densities $n_d\left(\vec{r},t\right)$ and Eq. 3.10 for the ambient ion densities $n_a\left(\vec{r},t\right)$ into the quasi-neutrality condition of Eq. 3.2 yields the electron density $n_e\left(\vec{r},t\right)$:

$$n_e\left(\vec{r},t\right) = \sum\nolimits_d Z_d n_d\left(\vec{r},t\right) + n_{e,meas}\left(\vec{r}\right). \tag{3.11}$$

In Eq. 3.11, the sum is taken over all debris ion charge states C II - C VII.

3.2.2 Model for Ion Current Density

Conveniently, much of the work towards a model of the total ion current density $\sum_i \vec{J}_i\left(\vec{r},t\right)$ has already been completed in the previous subsection. The summation is taken over the current density corresponding to each debris and ambient ion species, denoted $\vec{J}_d\left(\vec{r},t\right)$ and $\vec{J}_a\left(\vec{r},t\right)$, respectively. Thus,

$$\sum\nolimits_i \vec{J}_i\left(\vec{r},t\right) = \sum\nolimits_d \vec{J}_d\left(\vec{r},t\right) + \sum\nolimits_a \vec{J}_a\left(\vec{r},t\right). \tag{3.12}$$

For each debris ion charge state,

$$\vec{J}_d\left(\vec{r},t\right) = Z_d e n_d\left(\vec{r},t\right)\vec{v}_d\left(\vec{r},t\right) = Z_d e n_d\left(\vec{r},t\right)\left(\frac{r}{t}\right)\hat{r}, \tag{3.13}$$

where the debris ion density $n_d\left(\vec{r},t\right)$ follows from Eq. 3.8 and the drift velocity $\vec{v}_d\left(\vec{r},t\right) = \left(\frac{r}{t}\right)\hat{r}$ follows from the ballistic time-of-flight assumption. As expected from the expansion geometry, $\vec{J}_d\left(\vec{r},t\right)$ is directed radially outward.

By contrast to the expanding debris plasma, which contains charge states as high as C VII (corresponding to $Z_d = 6$) and expands at speeds upwards of ≈ 1000 km/s, the ambient

plasma contains only He II ($Z_a = 1$) and He III ($Z_a = 2$) and carries initial thermal speeds of only ≈ 3 km/s. For comparable debris and ambient ion densities (see Section 3.3), the expectation is that initially $\sum_d \vec{J}_d(\vec{r},t) \gg \sum_a \vec{J}_a(\vec{r},t)$, such that the total current density $\sum_i \vec{J}_i(\vec{r},t) \approx \sum_d \vec{J}_d(\vec{r},t)$. Substitution of Eq. 3.13 into Eq. 3.12 yields

$$\sum\nolimits_i \vec{J}_i(\vec{r},t) = \left(\frac{er}{t}\right) \sum\nolimits_d Z_d n_d(\vec{r},t)\,\hat{r}, \tag{3.14}$$

where the sum is taken over all debris ion charge states C II - C VII. As the ambient ions accelerate in response to the explosive debris plasma, they increasingly contribute to the current density and the approximation becomes less accurate.

3.2.3 Model for Magnetic Field

A calculation of the laminar electric field via Eq. 1.9 as well as the resulting Lorentz force that acts on the He II ambient ions via Eq. 3.1 generally requires full spatiotemporal knowledge of all three components of the magnetic field:

$$\vec{B}(\vec{r},t) = B_x(\vec{r},t)\,\hat{x} + B_y(\vec{r},t)\,\hat{y} + B_z(\vec{r},t)\,\hat{z}. \tag{3.15}$$

However, as detailed in Chapter 2, the magnetic flux probe measures only the z component of the magnetic field along an interval of the blow-off axis. While volumetric scans with three-axis magnetic flux probes can certainly yield full knowledge of $\vec{B}(\vec{r},t)$ in high repetition rate experiments, this is unfeasible at the low shot rate of the Raptor laser. As a result, the present analysis demands reasonable assumptions on the behavior of $B_x(\vec{r},t)$, $B_y(\vec{r},t)$, and $B_z(\vec{r},t)$ outside of the measured region.

Wavelength-filtered imaging, in combination with the measured magnetic field profiles, motivates a simple model of $B_z(\vec{r},t)$ in the blow-off plane. Fig. 3.3 compares images of He II ions collected via emission of the 468.6 nm spectral line to the corresponding line-outs of the normalized intensity and the magnetic field's z component along the blow-off axis at $t = 500$ ns, $t = 750$ ns, and $t = 1000$ ns. In addition, the images include overlays of the teardrop function of Eq. 3.5 at the previously optimized value of $\theta_0 = 1.5$ rad, with

the cusp position set to the magnetic compression maximum along the blow-off axis. As previously concluded from Fig. 2.7 in Chapter 2, the line-outs along the blow-off axis reveal a spatial correspondence between the He II intensification edge and the maximum compression, indicative of energetic electrons confined to the field lines. Moreover, as the maximum compression moves from $x \approx 26$ cm to $x \approx 36$ cm between $t = 500$ ns and $t = 1000$ ns, the teardrop continues to provide a reasonable fit to the He II fluorescence boundary in the blow-off plane. This suggests that the magnetic field in the blow-off plane also follows the same profile. The model developed here thus extrapolates the measured z component from the blow-off axis into the blow-off plane along the teardrop contours, such that

$$B_z\left(\vec{r},t\right) = B_{z,meas}\left(x,t\right), x \equiv \frac{r}{\exp\left(-\theta/\theta_0\right)\cos\theta}, \tag{3.16}$$

where $B_{z,meas}\left(x,t\right)$ is the experimentally measured z component at position x along the blow-off axis and x follows from re-arranging Eq. 3.5. At a fixed time, the "teardrops" define contours of constant $B_z\left(\vec{r},t\right)$. Eq. 3.16 is understood to be valid only in the blow-off plane ($z = 0$ cm).

The expanding debris plasma generally bends and deforms the initially uniform magnetic field directed along z, giving rise to $B_x\left(\vec{r},t\right)$ and $B_y\left(\vec{r},t\right)$. However, in the blow-off plane, the symmetry of the deformation implies that these components are negligible (see [63] for an excellent visualization of this based on two-dimensional hybrid code simulations). The present model assumes $B_x\left(\vec{r},t\right) = B_y\left(\vec{r},t\right) = 0$. Substitution of Eq. 3.16 into Eq. 3.15 thus yields the magnetic field in the blow-off plane,

$$\vec{B}\left(\vec{r},t\right) = B_{z,meas}\left(x,t\right)\hat{z}, \tag{3.17}$$

where the definition of x follows from Eq. 3.16. While Eq. 3.17 does not contain the full three-dimensional structure of the magnetic field, it nevertheless provides a model grounded in experimental data for calculations in the blow-off plane, which is sufficient for the subsequent analysis. For the teardrop region corresponding to $x < 26$ cm, where magnetic flux probe measurements are not taken, $\vec{B}\left(\vec{r},t\right)$ is set to the background magnetic field of $B_0 = 710$ G, directed in $-z$.

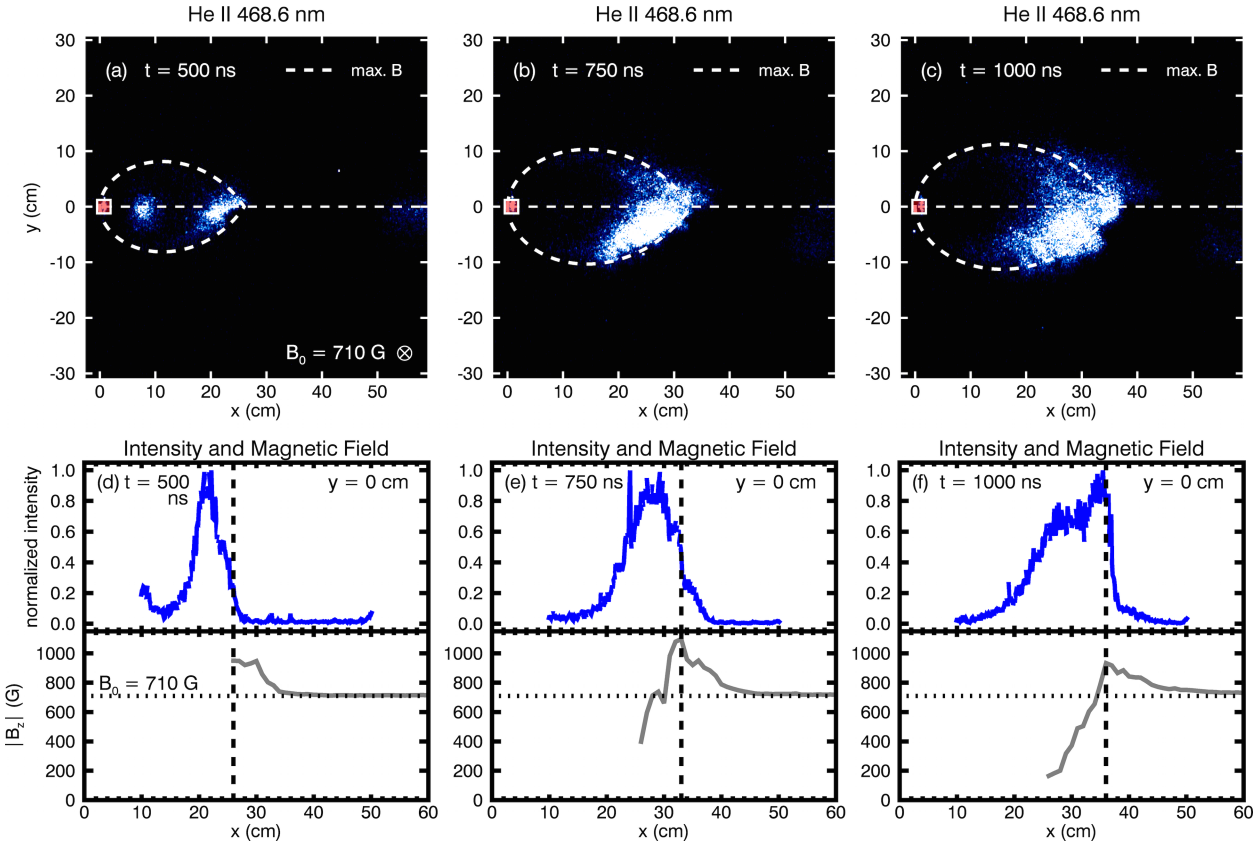

Figure 3.3: Comparison of wavelength-filtered images of He II ambient ions (via the 468.6 nm line) to corresponding line-outs of the normalized intensity (solid blue line) and the magnetic field z component (solid gray line) along the blow-off axis at $t = 500$ ns, $t = 750$ ns, and $t = 1000$ ns. The line-outs reveal a spatial correspondence between the He II fluorescence boundary and the maximum magnetic compression along the blow-off axis, as highlighted by the vertical dashed line. In the images, the superimposed squares mark the position where the laser pulse irradiates the target surface, the dashed lines denote the blow-off axis, and the magnetic field points into the page. The overlaid teardrop profiles correspond to Eq. 3.5 at the optimized value of $\theta_0 = 1.5$ rad, using the position of the maximum magnetic compression to define the cusp. The teardrop contour provides a good fit to the He II fluorescence boundary in the blow-off plane.

3.2.4 Model for Electron Pressure

From the theoretical considerations of Chapter 1, the satisfied condition $\beta_e \ll 1$ in the debris-ambient interaction region of the present experiment indicates that electron pressure gradients do not contribute significantly to the laminar electric field (Eq. 1.9). To verify the unimportance of pressure gradients in the context of the models developed throughout this section, a simple expression for the electron pressure $p_e(\vec{r},t)$ is obtained. The pressure follows from

$$p_e(\vec{r},t) = n_e(\vec{r},t)\, k_B T_e(\vec{r},t), \tag{3.18}$$

where $n_e(\vec{r},t)$ and $T_e(\vec{r},t)$ are the spatiotemporally dependent electron density and temperature, respectively, and k_B is Boltzmann's constant. While a model for $n_e(\vec{r},t)$ follows from Eq. 3.11, the behavior of $T_e(\vec{r},t)$ remains to be determined. As detailed in Chapter 2, swept Langmuir probe measurements of the unperturbed ambient plasma yield a profile of the electron temperature in the plane perpendicular to the magnetic field, detecting peak temperatures of ≈ 4 eV. However, as the explosive debris perturbs the ambient plasma, biased Langmuir probe measurements and filtered imaging reveal energetic electrons with directed kinetic energies of > 50 eV. This suggests a highly complex evolution of $T_e(\vec{r},t)$, though the data is insufficient to motivate a detailed model. The simplified approach utilized here assumes a uniform electron temperature profile in space and time, such that

$$T_e(\vec{r},t) = T_{e,max}, \tag{3.19}$$

where the value of $T_{e,max}$ follows from a reasonable upper limit of the electron temperature inferred from the data. This allows for a prediction of the maximum possible electron pressure $p_{e,max}(\vec{r},t)$, sufficient for the purpose of verifying the insignificance of the electron pressure gradients. Substitution of Eq. 3.11 and Eq. 3.19 into Eq. 3.18 yields

$$p_{e,max}(\vec{r},t) = \left[\sum\nolimits_d Z_d n_d(\vec{r},t) + n_{e,meas}(\vec{r})\right] k_B T_{e,max}, \tag{3.20}$$

where the sum is taken over all debris ion charge states C II - C VII.

3.2.5 Model for Laminar Electric Field

The heuristic models of the total electron density $n_e(\vec{r},t)$, the total ion current density $\sum_i \vec{J_i}(\vec{r},t)$, the magnetic field $\vec{B}(\vec{r},t)$, and the maximum electron pressure $p_{e,max}(\vec{r},t)$ allow for a direct calculation of the laminar electric field via

$$\vec{E}(\vec{r},t) = \vec{E}_{lam} = -\frac{1}{en_e}\vec{\nabla}p_e - \frac{1}{4\pi en_e}\vec{B}\times\left(\vec{\nabla}\times\vec{B}\right) - \frac{1}{en_e c}\sum\nolimits_i \vec{J_i}\times\vec{B}. \tag{1.9}$$

This subsection individually calculates each term of Eq. 1.9 in the blow-off plane ($z = 0$ cm), where considerable simplifications arise due to symmetry.

The first term of Eq. 1.9 denotes electric fields caused by electron pressure gradients:

$$\vec{E}_{elec} = -\frac{1}{en_e}\vec{\nabla}p_e. \tag{3.21}$$

Substituting Eq. 3.11 for $n_e(\vec{r},t)$ and Eq. 3.20 for $p_{e,max}(\vec{r},t)$ into Eq. 3.21, the assumed uniform electron temperature $T_{e,max}$ moves outside of the spatial gradient. Moreover, in the blow-off plane, symmetry implies that the debris ion density $n_d(\vec{r},t)$ does not vary over infinitesimal changes along the z direction. Similarly, the measured ambient electron density $n_{e,meas}(\vec{r})$ is assumed to be invariant along z. Thus,

$$\vec{E}_{elec}(\vec{r},t) = -\left(\frac{k_B T_{e,max}}{e}\right)\left(\frac{\sum_d Z_d \vec{\nabla}_\perp n_d(\vec{r},t) + \vec{\nabla}_\perp n_{e,meas}(\vec{r})}{\sum_d Z_d n_d(\vec{r},t) + n_{e,meas}(\vec{r})}\right), \tag{3.22}$$

where $\vec{\nabla}_\perp$ corresponds to the gradient in the blow-off plane, such that $\vec{E}_{elec}(\vec{r},t)$ does not have a z component. The magnitude of $\vec{E}_{elec}(\vec{r},t)$ represents an upper limit estimate of the electron pressure gradient contribution and depends on the debris and ambient electron density gradients, the total electron density, and a suitable guess for the maximum electron temperature $T_{e,max}$.[3] In accordance with the negative sign in front of Eq. 3.22, $\vec{E}_{elec}(\vec{r},t)$ points in the direction of decreasing plasma density.

The second term of Eq. 1.9 denotes electric fields caused by magnetic pressure gradients and tension:

$$\vec{E}_{mag} = -\frac{1}{4\pi en_e}\vec{B}\times\left(\vec{\nabla}\times\vec{B}\right). \tag{3.23}$$

[3]The possibility of large electron temperature gradients, which can significantly contribute to the magnitude of $\vec{E}_{elec}(\vec{r},t)$, is not considered here.

The expanding debris plasma deforms the initially uniform magnetic field through the generation of a magnetic compression and a diamagnetic cavity, generally resulting in a complex solution to Eq. 3.23. However, arguments from symmetry lead to considerable simplification. The vector term of Eq. 3.23 can be re-expressed in a more convenient form via

$$\vec{B} \times \left(\vec{\nabla} \times \vec{B} \right) = \frac{1}{2} \vec{\nabla} B^2 - \left(\vec{B} \cdot \vec{\nabla} \right) \vec{B}. \tag{3.24}$$

Because the initial magnetic field only has a z component, a symmetrically deformed magnetic field of the form $\vec{B} = B_x \hat{x} + B_y \hat{y} + B_z \hat{z}$ has vanishing B_x and B_y in the blow-off plane, though the spatial derivatives of these components are generally non-zero [63]. Moreover, B_z does not vary over infinitesimal changes along z. From Eq. 3.24, it therefore follows that

$$\vec{B} \times \left(\vec{\nabla} \times \vec{B} \right) = B_z \left(\frac{\partial B_z}{\partial x} - \frac{\partial B_x}{\partial z} \right) \hat{x} + B_z \left(\frac{\partial B_z}{\partial y} - \frac{\partial B_y}{\partial z} \right) \hat{y}, \tag{3.25}$$

indicating that the electric field $\vec{E}_{mag}$ does not have a z component. Furthermore, the deformation of the magnetic field in the blow-off plane is such that field gradients perpendicular to the field lines (in this case, along x and y) are typically more drastic than gradients parallel to the field lines (along z) [63]. Thus, $\frac{\partial B_z}{\partial x} \gg \frac{\partial B_x}{\partial z}$ and $\frac{\partial B_z}{\partial y} \gg \frac{\partial B_y}{\partial z}$, and Eq. 3.25 becomes

$$\vec{B} \times \left(\vec{\nabla} \times \vec{B} \right) = B_z \frac{\partial B_z}{\partial x} \hat{x} + B_z \frac{\partial B_z}{\partial y} \hat{y} = B_z \vec{\nabla}_\perp B_z, \tag{3.26}$$

where $\vec{\nabla}_\perp$ corresponds to the gradient in the blow-off plane. Eq. 3.26 demonstrates that only magnetic pressure gradients contribute significantly to $\vec{E}_{mag}$ in the blow-off plane, while magnetic tension is negligible.

Recalling that the teardrops of Eq. 3.5 define contours of constant magnetic field in the blow-off plane, it follows that the vector $B_z \vec{\nabla}_\perp B_z$ from Eq. 3.26 must point normal to the contours and in the direction of increasing B_z. A straightforward calculation of the slope of the normal to the contours yields an expression for the angle φ_B relative to the blow-off axis of a line running along $B_z \vec{\nabla}_\perp B_z$:

$$\tan \varphi_B = \frac{1 + \cos 2\theta + 2\theta_0 \sin 2\theta}{2\theta_0 \cos 2\theta - \sin 2\theta}. \tag{3.27}$$

The relationship of φ_B to θ is illustrated in Fig. 3.7. However, while Eq. 3.27 provides an easy method of determining the direction of $B_z\vec{\nabla}_\perp B_z$, calculation of its magnitude is less trivial due to a mathematical artifact introduced by the teardrop extrapolation of the magnetic field into the blow-off plane. Specifically, the magnitude of $B_z\vec{\nabla}_\perp B_z$ increases with θ due to the fact that the successive contours of constant magnetic field become spatially closer, thus artificially enhancing the gradient. In an attempt to correct for this unphysical effect, the magnitude is calculated only along the blow-off axis (where the magnetic field profile is measured directly) and applied along the teardrop contours throughout the blow-off plane. Employing this correction, substitution of Eq. 3.17 for $\vec{B}(\vec{r},t)$ into Eq. 3.26 yields

$$\left|\vec{B}(\vec{r},t)\times\left(\vec{\nabla}\times\vec{B}(\vec{r},t)\right)\right| \approx \left|B_{z,meas}(x,t)\,\frac{\partial B_{z,meas}(x,t)}{\partial x}\right|, \tag{3.28}$$

where the definition of x follows from Eq. 3.16. Substituting Eq. 3.11 for $n_e(\vec{r},t)$ and Eq. 3.28 for the vector expression into Eq. 3.23 then yields the magnitude of $\vec{E}_{mag}(\vec{r},t)$,

$$\left|\vec{E}_{mag}(\vec{r},t)\right| = \left|\frac{B_{z,meas}(x,t)}{4\pi e\left[\sum_d Z_d n_d(\vec{r},t)+n_{e,meas}(\vec{r})\right]}\frac{\partial B_{z,meas}(x,t)}{\partial x}\right|. \tag{3.29}$$

The magnitude thus depends on the measured magnetic field strength, the gradient of the magnetic field, and the total electron density. The negative sign in front of Eq. 3.23 implies that $\vec{E}_{mag}(\vec{r},t)$ points in the direction of decreasing magnetic field magnitude, along a line normal to the teardrop contours of Eq. 3.5. This line forms an angle φ_B with respect to the blow-off axis, as defined by Eq. 3.27.

The third term of Eq. 1.9 corresponds to electric fields caused by cross-field ion currents:

$$\vec{E}_{ion} = -\frac{1}{en_e c}\sum\nolimits_i \vec{J}_i\times\vec{B}. \tag{3.30}$$

Substitution of Eq. 3.11 for $n_e(\vec{r},t)$, Eq. 3.14 for $\sum_i \vec{J}_i(\vec{r},t)$, and Eq. 3.17 for $\vec{B}(\vec{r},t)$ into Eq. 3.30 yields

$$\vec{E}_{ion}(\vec{r},t) = -\left(\frac{r}{ct}\right)\left(\frac{\sum_d Z_d n_d(\vec{r},t)\,\hat{r}\times B_{z,meas}(x,t)\,\hat{z}}{\sum_d Z_d n_d(\vec{r},t)+n_{e,meas}(\vec{r})}\right). \tag{3.31}$$

In the blow-off plane, where the radial ion currents are always perpendicular to the magnetic field, the cross product computes easily. Simplifying Eq. 3.30 leads to

$$\vec{E}_{ion}(\vec{r},t) = \left(\frac{r}{ct}\right)\left(1+\frac{n_{e,meas}(\vec{r})}{\sum_d Z_d n_d(\vec{r},t)}\right)^{-1} B_{z,meas}(x,t)\,\hat{\theta}, \tag{3.32}$$

where the definition of x follows from Eq. 3.16 and $\hat{\theta}$ defines the azimuthal direction in the blow-off plane, pointing towards increasing angle θ. The magnitude of the cross-field ion current term $\vec{E}_{ion}(\vec{r},t)$ thus depends on the measured magnetic field strength, the time-of-flight speed, and the ratio of debris and ambient electron densities. Taking into account the negative value of $B_{z,meas}(x,t)$ (since the magnetic field points in the $-z$ direction), $\vec{E}_{ion}(\vec{r},t)$ points in the clockwise azimuthal direction provided that the magnetic field points into the page and the debris expands radially outward.

The total laminar electric field can now be obtained from the vector sum of the three terms:

$$\vec{E}(\vec{r},t) = \vec{E}_{elec}(\vec{r},t) + \vec{E}_{mag}(\vec{r},t) + \vec{E}_{ion}(\vec{r},t). \tag{3.33}$$

Like its contributing components, the total electric field $\vec{E}(\vec{r},t)$ of Eq. 3.33 does not have a z component in the blow-off plane and is therefore perpendicular to the magnetic field.

3.2.6 Summary of Models

The available experimental data and radiation-hydrodynamic simulations in HELIOS motivate plasma parameter models primarily based on the following assumptions:

- H II ions, neutrals, and molecules in the debris do not affect the ambient plasma.
- The debris ions expand ballistically (no acceleration, deceleration, or gyration).
- The debris ions have drifting Maxwellian velocity distributions.
- The debris ion expansion is represented by a symmetric 3D teardrop.
- The ambient density profile is not perturbed significantly by the debris.
- The ambient ions do not contribute significantly to the total ion current density.
- The magnetic field profile in the blow-off plane follows the teardrop shape.

Employing these assumptions, the spatiotemporal evolution of the total electron density $n_e(\vec{r},t)$, the total ion current density $\sum_i \vec{J}_i(\vec{r},t)$, the magnetic field $\vec{B}(\vec{r},t)$, and the maxi-

mum electron pressure $p_{e,max}(\vec{r},t)$ is determined by the expressions

$$n_e(\vec{r},t) = \sum\nolimits_d Z_d n_d(\vec{r},t) + n_{e,meas}(\vec{r}), \tag{3.11}$$

$$\sum\nolimits_i \vec{J}_i(\vec{r},t) = \left(\frac{er}{t}\right) \sum\nolimits_d Z_d n_d(\vec{r},t)\,\hat{r}, \tag{3.14}$$

$$\vec{B}(\vec{r},t) = B_{z,meas}(x,t)\,\hat{z}, x \equiv \frac{r}{\exp(-\theta/\theta_0)\cos\theta}, \tag{3.17}$$

$$p_{e,max}(\vec{r},t) = \left[\sum\nolimits_d Z_d n_d(\vec{r},t) + n_{e,meas}(\vec{r})\right] k_B T_{e,max}, \tag{3.20}$$

where the debris ion density $n_d(\vec{r},t)$ follows from

$$n_d(\vec{r},t) = \frac{C_d}{t^3} \exp\left[-\frac{\left(r - \bar{V}_d t \exp(-\theta/\theta_0)\cos\theta\right)^2}{2\sigma_d^2 t^2}\right]. \tag{3.8}$$

Here, $r = \sqrt{x^2+y^2+z^2}$ is the distance from the origin, $\theta = \arctan\left(\sqrt{y^2+z^2}/x\right)$ is the angle with respect to the blow-off axis (limited to $0 \leq \theta \leq \frac{\pi}{2}$), and t is time. The charge numbers Z_d, normalization constants C_d, average drift velocities $\bar{V}_d$, and velocity spreads σ_d follow from Table 3.2, and the sums are taken over all the debris ion charge states C II - C VII. The optimized parameter $\theta_0 = 1.5$ rad corresponds to the teardrop shape that best fits the observed debris expansion. In Eq. 3.11 and Eq. 3.20, $n_{e,meas}(\vec{r})$ corresponds to the measured ambient electron density profile of Fig. 2.3 from Chapter 2. In Eq. 3.17, which is valid only in the blow-off plane ($z = 0$ cm), $B_{z,meas}(x,t)$ corresponds to the measured magnetic field z component along the blow-off axis. In Eq. 3.20, $T_{e,max}$ is the estimated upper limit of the electron temperature, and k_B and e are Boltzmann's constant and the elementary charge, respectively.

The derived plasma parameter models allow for a direct calculation of the laminar electric field via Eq. 1.9. In the blow-off plane ($z = 0$ cm), the electron pressure gradient term $\vec{E}_{elec}(\vec{r},t)$, the magnetic pressure gradient and tension term $\vec{E}_{mag}(\vec{r},t)$, and the cross-field ion current term $\vec{E}_{ion}(\vec{r},t)$ follow from

$$\vec{E}_{elec}(\vec{r},t) = -\left(\frac{k_B T_{e,max}}{e}\right)\left(\frac{\sum_d Z_d \vec{\nabla}_\perp n_d(\vec{r},t) + \vec{\nabla}_\perp n_{e,meas}(\vec{r})}{\sum_d Z_d n_d(\vec{r},t) + n_{e,meas}(\vec{r})}\right), \tag{3.22}$$

$$\vec{E}_{ion}(\vec{r},t) = \left(\frac{r}{ct}\right)\left(1 + \frac{n_{e,meas}(\vec{r})}{\sum_d Z_d n_d(\vec{r},t)}\right)^{-1} B_{z,meas}(x,t)\,\hat{\theta}, \tag{3.32}$$

$$\left|\vec{E}_{mag}\left(\vec{r},t\right)\right| = \left|\frac{B_{z,meas}\left(x,t\right)}{4\pi e\left[\sum_d Z_d n_d\left(\vec{r},t\right) + n_{e,meas}\left(\vec{r}\right)\right]}\frac{\partial B_{z,meas}\left(x,t\right)}{\partial x}\right|, \tag{3.29}$$

$$\tan\varphi_B = \frac{1+\cos 2\theta + 2\theta_0 \sin 2\theta}{2\theta_0\cos 2\theta - \sin 2\theta}. \tag{3.27}$$

In the above expressions, $\vec{E}_{elec}\left(\vec{r},t\right)$ points in the direction of decreasing electron density, as determined by the gradient $\vec{\nabla}_\perp$ in the blow-off plane. $\vec{E}_{mag}\left(\vec{r},t\right)$ points towards decreasing magnetic field magnitude along the normal to the teardrop contours of Eq. 3.5, defined by the angle φ_B with respect to the blow-off axis. $\vec{E}_{ion}\left(\vec{r},t\right)$ is directed azimuthally, as indicated by $\hat{\theta}$, resulting in a clockwise contribution provided that the magnetic field points into the page. The total laminar electric field follows from the vector sum of the three terms:

$$\vec{E}\left(\vec{r},t\right) = \vec{E}_{elec}\left(\vec{r},t\right) + \vec{E}_{mag}\left(\vec{r},t\right) + \vec{E}_{ion}\left(\vec{r},t\right). \tag{3.33}$$

Like its contributing components, the total electric field $\vec{E}\left(\vec{r},t\right)$ of Eq. 3.33 does not have a z component in the blow-off plane and is therefore perpendicular to the magnetic field.

In the analysis to follow, four different versions of the heuristic models are applied in order to investigate the self-consistency of the computational approach and to characterize the sensitivity of the output to changes in the input. Specifically, several parameters that determine the debris ion densities $n_d\left(\vec{r},t\right)$ through Eq. 3.8 are varied with the intention of producing greater deviations from the data for inputs that differ significantly from the expected experimental conditions. To better understand the model variations, it is useful to first consider the kinetic energy of the debris plasma. Assuming the debris ions carry the vast majority of the kinetic energy, the kinetic energy density $U\left(\vec{r},t\right)$ follows from

$$U\left(\vec{r},t\right) = \frac{1}{2}m_C\sum\nolimits_d n_d\left(\vec{r},t\right)v_d^2\left(\vec{r},t\right), \tag{3.34}$$

where $n_d\left(\vec{r},t\right)$ and $v_d\left(\vec{r},t\right)$ are the density and speed of each debris ion charge state, m_C is the atomic mass of C, and the sum is taken over all charge states C II - C VII. Utilizing Eq. 3.8 for $n_d\left(\vec{r},t\right)$ and the ballistic time-of-flight assumption $\vec{v}_d\left(\vec{r},t\right) = \left(\frac{r}{t}\right)\hat{r}$ allows for a calculation of $U\left(\vec{r},t\right)$. The total kinetic energy E_K then follows from integration of Eq. 3.34 over all space:

$$E_K = \int_r U\left(\vec{r},t\right)\mathrm{d}^3\vec{r}. \tag{3.35}$$

	ion	C II	C III	C IV	C V	C VI	C VII
	$\mathbf{Z_d}$	1	2	3	4	5	6
	$\chi_\mathbf{d}$	0.064	0.187	0.322	0.408	0.014	0.006
Run 1 (3D)	$\bar{\mathbf{V}}_\mathbf{d}$	0.044	0.231	0.434	1.508	5.742	9.925
$N_{tot} = 1.865\text{E}17$	$\sigma_\mathbf{d}$	0.100	0.253	0.355	1.734	1.979	1.071
$E_K = 94$ J	$\mathbf{C_d}$	1.225E−3	1.722E−4	9.171E−5	1.195E−6	1.027E−8	1.668E−8
Run 2 (10X)	$\bar{\mathbf{V}}_\mathbf{d}$	0.015	0.080	0.150	0.500	1.900	3.300
$N_{tot} = 1.865\text{E}18$	$\sigma_\mathbf{d}$	0.030	0.080	0.110	0.550	0.620	0.330
$E_K = 94$ J	$\mathbf{C_d}$	4.400E−1	5.209E−2	2.869E−2	3.669E−4	3.111E−6	5.026E−6
Run 3 (0.1X)	$\bar{\mathbf{V}}_\mathbf{d}$	0.130	0.700	1.500	4.700	19.000	33.000
$N_{tot} = 1.865\text{E}16$	$\sigma_\mathbf{d}$	0.330	0.800	1.100	5.400	6.000	3.000
$E_K = 94$ J	$\mathbf{C_d}$	3.488E−6	5.555E−7	2.869E−7	3.954E−9	3.288E−11	5.689E−11
Run 4 (2D)	$\bar{\mathbf{V}}_\mathbf{d}$	0.044	0.231	0.434	1.508	5.742	9.925
$N_{tot} = 1.865\text{E}17$ cm^{-1}	$\sigma_\mathbf{d}$	0.100	0.253	0.355	1.734	1.979	1.071
$E_K = 73$ J cm^{-1}	$\mathbf{C_d}$	2.995E3	1.062E3	8.016E2	5.044E1	5.973E−1	1.322E0

Table 3.2: Values of charge number Z_d, ionization fraction χ_d, average velocity $\bar{V}_d$, velocity spread σ_d, integration constant C_d, total ablated ion number N_{tot}, and kinetic energy E_K corresponding to all four versions of the plasma parameter models for charge states C II - C VII. "Run 1 (3D)" follows directly from the HELIOS simulation results of Table 3.1 extracted at $t = 500$ ns. "Run 2 (10X)" and "Run 3 (0.1X)" correspond to a factor of 10 increase and decrease, respectively, in the HELIOS-predicted N_{tot}, adjusting the other parameters to keep E_K fixed. "Run 4 (2D)" corresponds to a two-dimensional debris expansion, once again utilizing the HELIOS results. The values of $\bar{V}_d$ and σ_d are in units of 10^7 cm/s. The values of C_d are in units of s^3/cm^3 except for "Run 4 (2D)," where they are in s^2/cm^3.

The first version of the heuristic models, titled "Run 1 (3D)" in Table 3.2, assumes a three-dimensional debris expansion and utilizes the values of total ablated ion number N_{tot}, normalization constants C_d, average velocities $\bar{V}_d$, and velocity spreads σ_d corresponding directly to the HELIOS simulation of Table 3.1. Calculation of the total debris kinetic energy via Eq. 3.34 and Eq. 3.35 yields $E_K = 94$ J, a reasonable value provided that roughly

60% of the $\approx$ 150 J laser pulse converts into kinetic energy of the ablated ions.[4] This version provides the most accurate representation of the actual experimental conditions. The second version, titled "Run 2 (10X)," intentionally multiplies the HELIOS-predicted number of ablated ions N_{tot} by a factor of 10. Without further adjustment, this necessarily multiplies the debris kinetic energy by a factor of 10 as well, creating an experimentally unrealistic scenario. To maintain feasible conditions, the velocity distributions are modified in order to keep the total kinetic energy fixed at $E_K = 94$ J via Eq. 3.34 and Eq. 3.35, despite the increased number of ions. Unsurprisingly, this requires the reduction of $\bar{V}_d$ and σ_d corresponding to each debris ion charge state by a factor of ≈ 3, as kinetic energy goes as the square of speed. The constants C_d are then recomputed for the modified N_{tot}, $\bar{V}_d$, and σ_d via Eq. 3.9. The third version, titled "Run 3 (0.1X)," intentionally divides the HELIOS-predicted number of ablated ions N_{tot} by a factor of 10. Analogously, $\bar{V}_d$ and σ_d are increased by a factor of ≈ 3 in order to preserve the total kinetic energy at $E_K = 94$ J, and the constants C_d are recomputed accordingly. Finally, the fourth version, titled "Run 4 (2D)," assumes a two-dimensional expansion in the plane perpendicular to the magnetic field with no variation in the plasma parameters along the z direction. This version utilizes the same HELIOS-predicted values of N_{tot}, $\bar{V}_d$, and σ_d employed for "Run 1 (3D)," though the interpretation of N_{tot} changes to the total number of ablated ions per cm of the third, invariant z dimension. The new expansion geometry requires a minor modification of the plasma parameter models, and it is straightforward to show that analogous two-dimensional expressions in the blow-off plane ($z = 0$ cm) differ only by a single power of the time t. Specifically, the $\frac{1}{t^3}$ term at the front of Eq. 3.8 becomes $\frac{1}{t^2}$. The constants C_d must also be recalculated in order to account for the new geometry. Computation of the kinetic energy via expressions analogous to Eq. 3.34 and Eq. 3.35 yields $E_K = 73$ J per cm of z. All four versions of the models assume the HELIOS-simulated ionization fractions χ_d. The values of Z_d, χ_d, $\bar{V}_d$, σ_d, C_d, N_{tot}, and E_K for all four model variations and for all charge states C II - C VII are listed in Table 3.2.

[4]The calculated debris kinetic energy depends on the HELIOS simulation results and the specific function chosen to represent the expansion geometry.

3.3 Results of Plasma Parameter Models

This section assesses the results of the heuristic models derived in Section 3.2, utilizing the parameters of Table 3.2. First, the spatiotemporal evolution of the computed laminar electric field $\vec{E}(\vec{r},t)$ in the blow-off plane ($z = 0$ cm) is analyzed in relation to the magnetic field $\vec{B}(\vec{r},t)$ and the debris ion densities $n_d(\vec{r},t)$. Then, the computed $\vec{E}(\vec{r},t)$ and $\vec{B}(\vec{r},t)$ are used to simulate the initial response of a distribution of He II ions to the expanding debris plasma via the Lorentz force (Eq. 3.1).

3.3.1 Spatiotemporal Evolution of the Laminar Electric Field

In accordance with Eq. 3.33, the total electric field $\vec{E}(\vec{r},t)$ follows from the vector sum of the electron pressure gradient term $\vec{E}_{elec}(\vec{r},t)$ (Eq. 3.22), the magnetic pressure gradient term $\vec{E}_{mag}(\vec{r},t)$ (Eq. 3.27 and Eq. 3.29), and the cross-field ion current term $\vec{E}_{ion}(\vec{r},t)$ (Eq. 3.32). However, as anticipated from the theoretical considerations of Chapter 1 and the experimental results presented in Chapter 2, the satisfied condition $\beta_e \ll 1$ implies that the electron pressure gradient term $\vec{E}_{elec}(\vec{r},t)$ should not contribute significantly. As a verification, the magnitude of $\vec{E}_{elec}(\vec{r},t)$ is compared to the total magnitude of $\vec{E}(\vec{r},t)$, utilizing the parameters corresponding to "Run 1 (3D)" from Table 3.2 and assuming a maximum electron temperature $k_B T_{e,max} = 100$ eV (loosely motivated by the detection of electrons with directed kinetic energies of > 50 eV via biased Langmuir probes, as detailed in Chapter 2). At the position $(x, y) = (20, 0)$ cm, corresponding to the edge of the ambient plasma where coupling first becomes important, $\vec{E}_{elec}(\vec{r},t)$ comprises just $\approx 11\%$ of the total magnitude at its peak. At $(x, y) = (30, 0)$ cm, corresponding to the center of the ambient plasma column, the maximum contribution drops to $\approx 1\%$. At greater distances from the origin, the relative contribution decreases even further. The relative insignificance of $\vec{E}_{elec}(\vec{r},t)$ provides an important consistency check of the plasma parameter models and allows the total electric field to be well approximated by

$$\vec{E}(\vec{r},t) \approx \vec{E}_{mag}(\vec{r},t) + \vec{E}_{ion}(\vec{r},t). \tag{3.36}$$

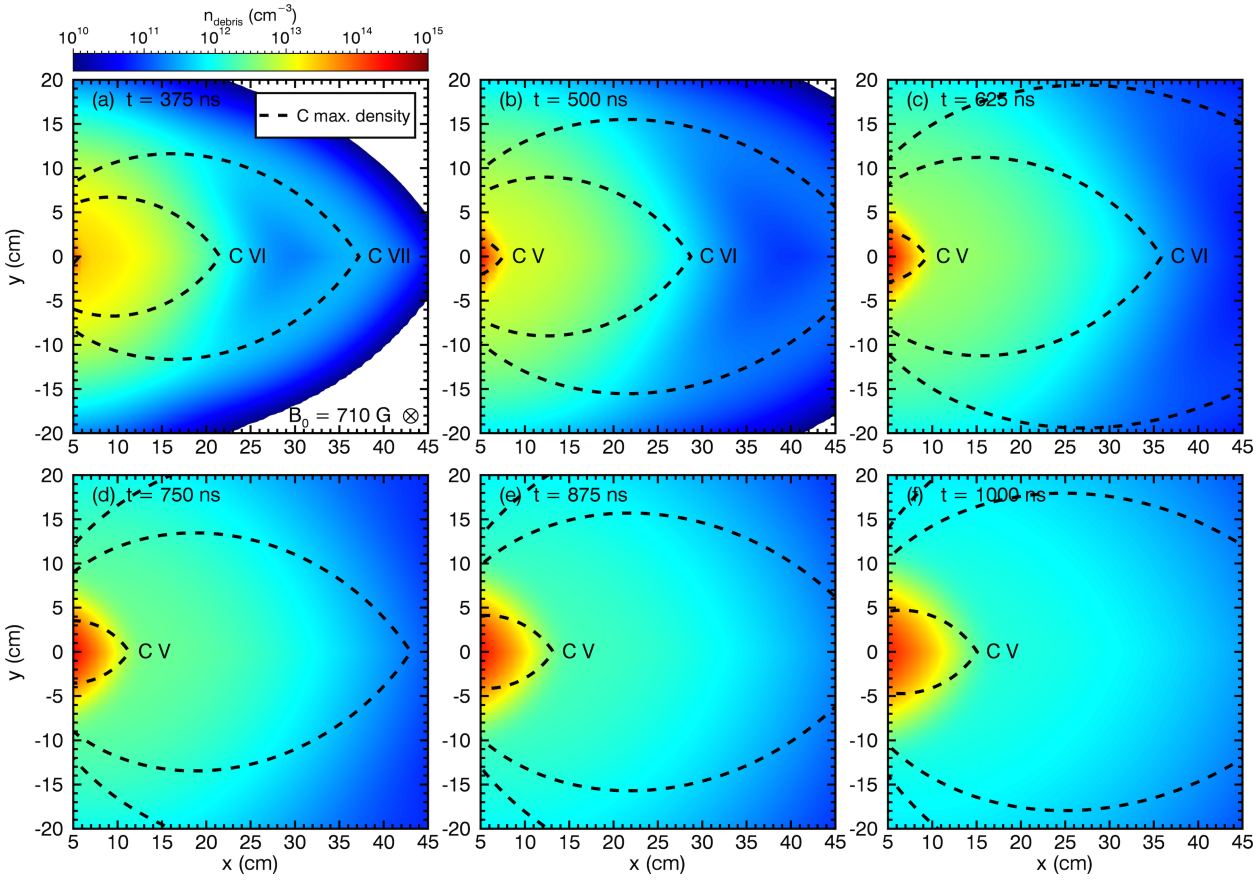

Figure 3.4: Spatiotemporal evolution of the debris ion densities in the blow-off plane, corresponding to the parameters of "Run 1 (3D)" in Table 3.2. The color contour shows the total debris ion density $\sum_d n_d(\vec{r}, t)$ (Eq. 3.8), while the teardrops (dashed black lines) indicate the positions of maximum density corresponding to each debris ion charge state.

In the subsequent analysis of this section, the electric field $\vec{E}(\vec{r}, t)$ is computed via Eq. 3.36 and contributions due to electron pressure gradients are assumed to be negligible.

Fig. 3.4 and Fig. 3.5 together illustrate the spatiotemporal evolution of the laminar electric field in relation to the magnetic field and the expanding debris plasma, based on the parameters of "Run 1 (3D)" in Table 3.2. Specifically, Fig. 3.4 shows color contours of the total debris ion density $\sum_d n_d(\vec{r}, t)$ (Eq. 3.8), as well as the teardrops corresponding to the peak density position of each debris ion charge state, while Fig. 3.5 shows the vectors of the total electric field $\vec{E}(\vec{r}, t)$ (Eq. 3.36) superimposed on color contours of the magnitude

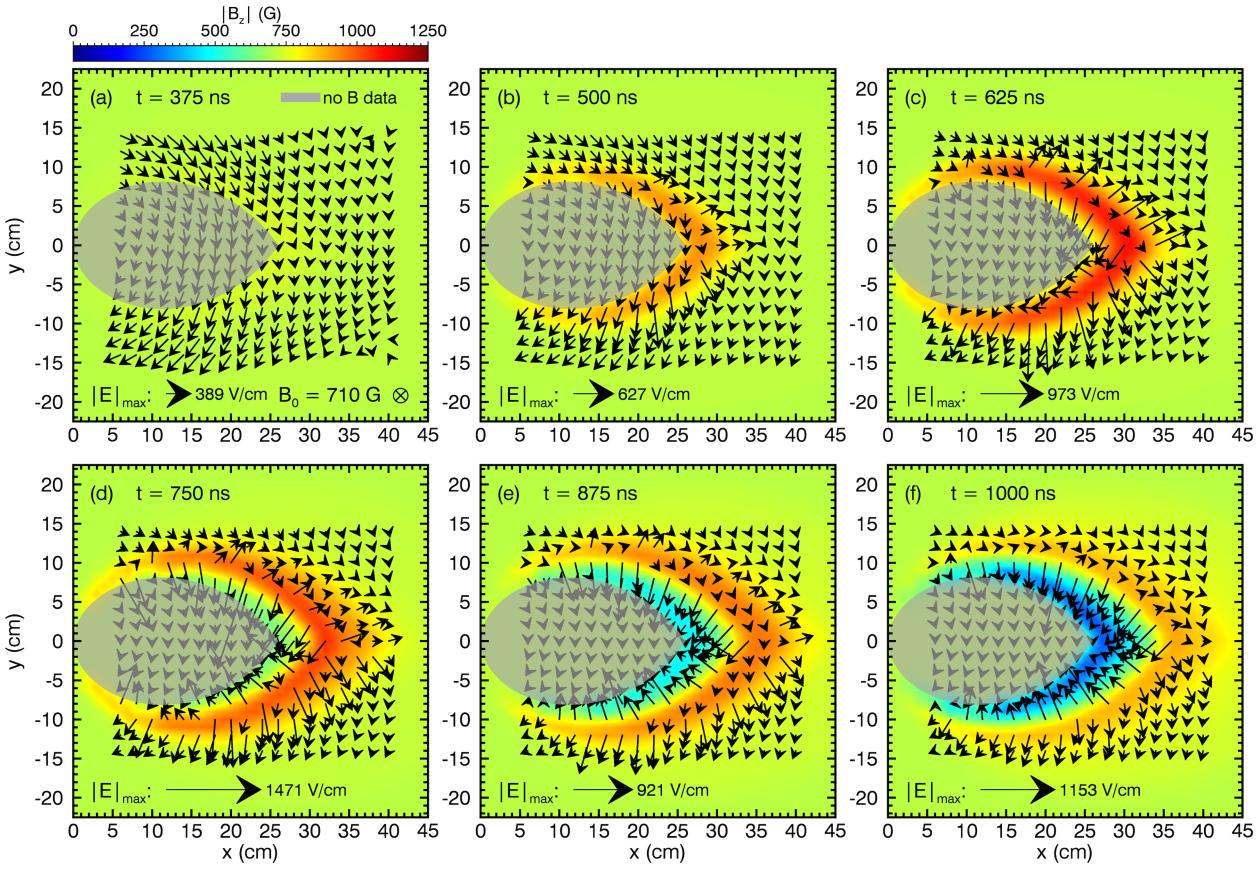

Figure 3.5: Spatiotemporal evolution of the electric and magnetic fields in the blow-off plane, corresponding to the parameters of "Run 1 (3D)" in Table 3.2. The vectors represent the total electric field $\vec{E}\,(\vec{r},t)$ (Eq. 3.36), and the scale is indicated via the maximum vector magnitude plotted at each time. The color contour represents magnitude of the magnetic field $\vec{B}\,(\vec{r},t)$ (Eq. 3.17), which is directed into the page. The grayed-out teardrop corresponds to the region where the magnetic field is not diagnosed and set to the background value of 710 G.

of the magnetic field $\vec{B}\,(\vec{r},t)$ (Eq. 3.17). The parameters are plotted in the blow-off plane at various times between $t = 375$ ns and $t = 1000$ ns. At $t = 375$ ns, the peak density of C VII (the fastest debris ion charge state) streams through the central region of the ambient plasma column, reaching $x \approx 35$ cm along the blow-off axis. Because the C VII ions outrun the magnetic compression and diamagnetic cavity and pass through a region of

uniform magnetic field (at the background value of 710 G), the resulting electric field only contains a clockwise azimuthal contribution $\vec{E}_{ion}(\vec{r},t)$ from the cross-field ion current. By $t = 625$ ns, the front of the magnetic compression reaches $x \approx 35$ cm along the blow-off axis. While the radial streaming of the debris ions continues to produce a clockwise azimuthal electric field via $\vec{E}_{ion}(\vec{r},t)$, the gradient in the magnetic field magnitude at the front of the compression now also contributes a radial-like outward electric field from $\vec{E}_{mag}(\vec{r},t)$, and the vector sum of the two contributions results in a complex, asymmetric field structure. By $t = 1000$ ns, the diamagnetic cavity edge reaches $x \approx 30$ cm along the blow-off axis. The magnitude of the azimuthal electric field $\vec{E}_{ion}(\vec{r},t)$ declines due to the slower time-of-flight speeds associated with later times and the expulsion of the magnetic field, and the total electric field is dominated by the radial-like inward contribution from $\vec{E}_{mag}(\vec{r},t)$, produced by the gradient in the magnetic field at the diamagnetic cavity edge. It is worth noting that the simulated laminar electric field structure is consistent with the measured profile of the deformed magnetic field, in accordance with the theoretical considerations of Chapter 1. Specifically, the radial-like inward contribution from the magnetic pressure gradient is the necessary electric field to drive the electrons into a clockwise azimuthal $\vec{E} \times \vec{B}$ drift and set up a diamagnetic current that expels the magnetic field (the diamagnetic cavity). Similarly, the radial-like outward contribution from the magnetic pressure gradient is the necessary electric field to drive the electrons into a counter-clockwise azimuthal $\vec{E} \times \vec{B}$ drift, which creates a current that adds to the magnetic field (the magnetic compression).

Fig. 3.6 further elucidates the evolution of the laminar electric field in relation to the magnetic field and the expanding debris plasma by examining the behavior in time at a fixed position in space, based on the parameters of "Run 1 (3D)" in Table 3.2. Specifically, this figure compares the x and y components of the magnetic pressure gradient term $\vec{E}_{mag}(\vec{r},t)$, the cross-field ion current term $\vec{E}_{ion}(\vec{r},t)$, and the total electric field $\vec{E}(\vec{r},t)$ to the debris ion densities $n_d(\vec{r},t)$ corresponding to each charge state and the magnitude of the magnetic field $\vec{B}(\vec{r},t)$. The evolution is plotted between $t = 0$ ns and $t = 1000$ at the position $(x, y) = (30, 0.5)$ cm, near the center of the ambient plasma column and just above the blow-off axis.

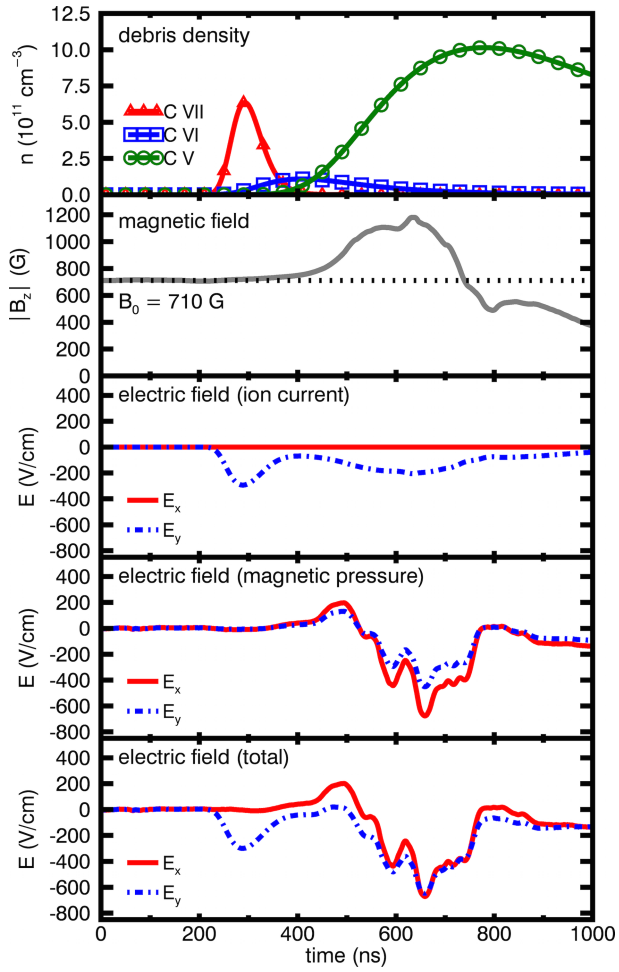

Figure 3.6: Temporal evolution of the electric field in relation to the magnetic field and the debris density at a fixed position, corresponding to the parameters of "Run 1 (3D)" in Table 3.2. From top to bottom, the plots show the debris ion densities $n_d\left(\vec{r},t\right)$ (Eq. 3.8), the magnitude of the magnetic field $\vec{B}\left(\vec{r},t\right)$ (Eq. 3.17), and the x and y components of the cross-field ion current term $\vec{E}_{ion}\left(\vec{r},t\right)$ (Eq. 3.32), the magnetic pressure gradient term $\vec{E}_{mag}\left(\vec{r},t\right)$ (Eq. 3.27 and Eq. 3.29), and the total electric field $\vec{E}\left(\vec{r},t\right)$ (Eq. 3.36) at $(x,y) = (30, 0.5)$ cm.

For comparison, the static ambient electron density at this position is $n_{e,meas}\left(\vec{r}\right) \approx 6 \times 10^{12}$ cm^{-3}. The fast C VII ions stream past the observation position between $t \approx 200$ ns and $t \approx 400$ ns, outrunning the magnetic compression. The associated ion current produces $\vec{E}_{ion}\left(\vec{r},t\right)$, which is primarily directed in $-y$ and achieves a peak magnitude of ≈ 300 V/cm.

The absence of gradients in the magnetic field during this time interval results in a negligible $\vec{E}_{mag}(\vec{r},t)$. By $t \approx 500$ ns, enough C V ions reach the observation position to comprise the majority of the local debris ion density. Concurrently, the magnetic field magnitude begins to increase, corresponding to the arrival of the magnetic compression front. The debris ion currents continue to produce $\vec{E}_{ion}(\vec{r},t)$ directed in $-y$, though the magnitude decreases to $\approx$ 200 V/cm. In addition, the magnetic compression front now generates $\vec{E}_{mag}(\vec{r},t)$, which initially has positive x and y components of $\approx$ 200 V/cm each. Correspondingly, the y component of the total electric field $\vec{E}(\vec{r},t)$ nearly cancels completely at this time. Between $t \approx 600$ ns and $t \approx 800$ ns, C V continues to dominate the debris density and the magnetic field magnitude rapidly decreases, corresponding to the arrival of the trailing side of the magnetic compression and the diamagnetic cavity edge. Debris ion currents continue to produce $\vec{E}_{ion}(\vec{r},t)$ directed in $-y$, though the magnitude declines further due to the expulsion of the magnetic field and the slower time-of-flight speeds associated with later times. The cavity edge, which has a gradient in the opposite direction of the magnetic compression front, reverses the direction of $\vec{E}_{mag}(\vec{r},t)$, which now has negative x and y components with peak magnitudes of $\approx$ 700 V/cm and $\approx$ 400 V/cm, respectively.

Several important observations follow from Fig. 3.4, Fig. 3.5, and Fig. 3.6. First, both the radial-like $\vec{E}_{mag}(\vec{r},t)$ and the azimuthal $\vec{E}_{ion}(\vec{r},t)$ contribute significantly to the total electric field $\vec{E}(\vec{r},t)$, with typical magnitudes in the hundreds of V/cm. This is consistent with the theoretical considerations of Chapter 1, which indicate that the magnitude ratio of $\vec{E}_{ion}(\vec{r},t)$ to $\vec{E}_{mag}(\vec{r},t)$ should scale as the Alfvénic Mach number M_A. The marginal current value of $M_A \approx 2$ (corresponding to the time of flight of the magnetic compression, as detailed in Chapter 2) thus signifies an intermediate regime in which both terms participate. Second, the sum of the radial-like $\vec{E}_{mag}(\vec{r},t)$ and the azimuthal $\vec{E}_{ion}(\vec{r},t)$ results in an asymmetric structure in the vector field of $\vec{E}(\vec{r},t)$ between the upper and lower portions of the blow-off plane, most clearly evident between $t = 500$ ns and $t = 875$ ns in Fig. 3.5. Specifically, $\vec{E}(\vec{r},t)$ is characterized by small $+y$ components in the upper half of the blow-off plane ($y > 0$ cm) and large $-y$ components in the lower half ($y < 0$ cm). Fig. 3.7 schematically

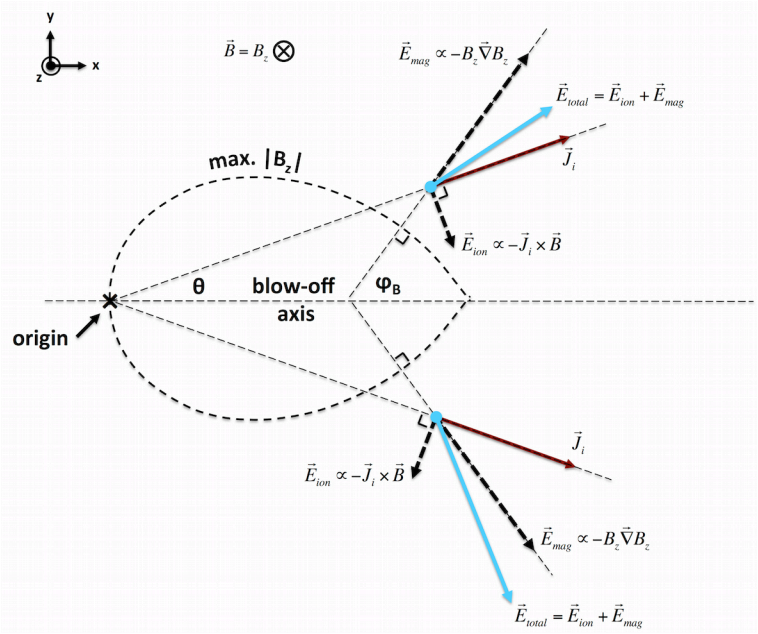

Figure 3.7: Schematic demonstration of the cause of the asymmetry in the total electric field $\vec{E}(\vec{r}, t)$ (Eq. 3.36). The dashed teardrop denotes the position of the peak magnetic compression. Just ahead of the peak compression, the gradient in the magnetic field magnitude produces a radial-like outward electric field $\vec{E}_{mag}(\vec{r}, t)$ at an angle φ_B with respect to the blow-off axis, in accordance with Eq. 3.27 and Eq. 3.29. Simultaneously, the radially outward debris ion currents generate a clockwise azimuthal electric field $\vec{E}_{ion}(\vec{r}, t)$, in accordance with Eq. 3.32. Above the blow-off axis ($y > 0$ cm), the y components of the two contributions act to cancel each other. Below the blow-off axis ($y < 0$ cm), the y components add. Provided that the magnitude of $\vec{E}_{mag}(\vec{r}, t)$ somewhat exceeds that of $\vec{E}_{ion}(\vec{r}, t)$, the total electric field $\vec{E}(\vec{r}, t)$ has a small $+y$ component above the blow-off axis and a much larger $-y$ component below the blow-off axis. The asymmetry only becomes apparent provided that the magnitudes of $\vec{E}_{mag}(\vec{r}, t)$ and $\vec{E}_{ion}(\vec{r}, t)$ are comparable.

illustrates how the asymmetry arises. Third, in the central region of the ambient plasma column between $x \approx 20$ cm and $x \approx 40$ cm along the blow-off axis, the total debris density is comparable to the ambient density. At $(x, y) = (30, 0.5)$ cm, for example, the debris ion density never exceeds $\approx 1 \times 10^{12}$ cm^{-3}, similar to the measured ambient electron density of

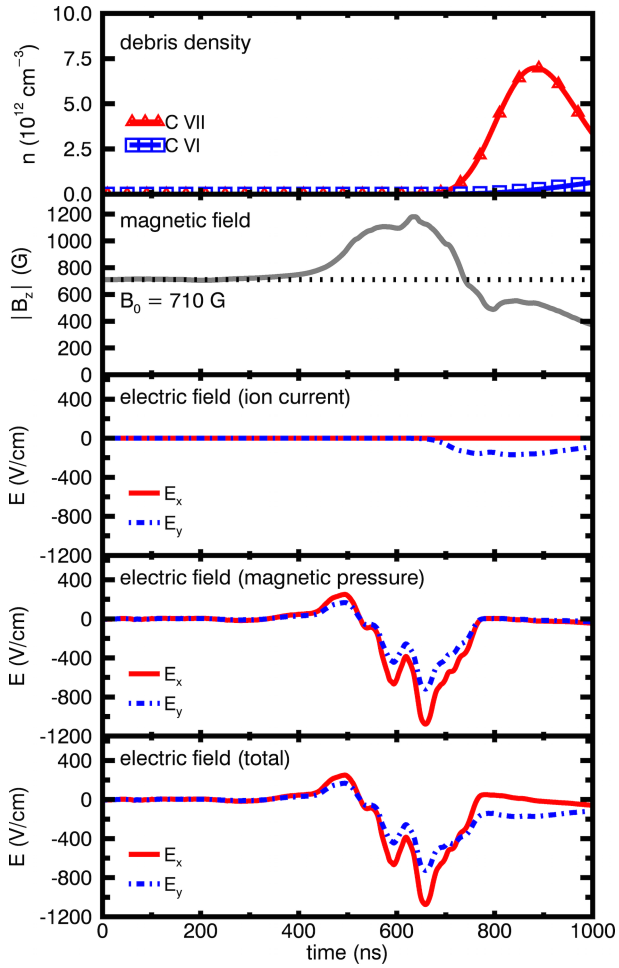

Figure 3.8: Temporal evolution of the electric field in relation to the magnetic field and the debris density at a fixed position, corresponding to the parameters of "Run 2 (10X)" in Table 3.2. From top to bottom, the plots show the debris ion densities $n_d\left(\vec{r},t\right)$ (Eq. 3.8), the magnitude of the magnetic field $\vec{B}\left(\vec{r},t\right)$ (Eq. 3.17), and the x and y components of the cross-field ion current term $\vec{E}_{ion}\left(\vec{r},t\right)$ (Eq. 3.32), the magnetic pressure gradient term $\vec{E}_{mag}\left(\vec{r},t\right)$ (Eq. 3.27 and Eq. 3.29), and the total electric field $\vec{E}\left(\vec{r},t\right)$ (Eq. 3.36) at $(x,y) = (30, 0.5)$ cm.

$\approx 6 \times 10^{12}$ cm^{-3} at the same position. This verifies that the condition $\beta_e \ll 1$ continues to hold as the debris expands into the ambient plasma.

By analogy to Fig. 3.6, the temporal evolution corresponding to the parameters of "Run 2 (10X)," "Run 3 (0.1X)," and "Run 4 (2D)" from Table 3.2 is shown in Fig. 3.8, Fig. 3.9,

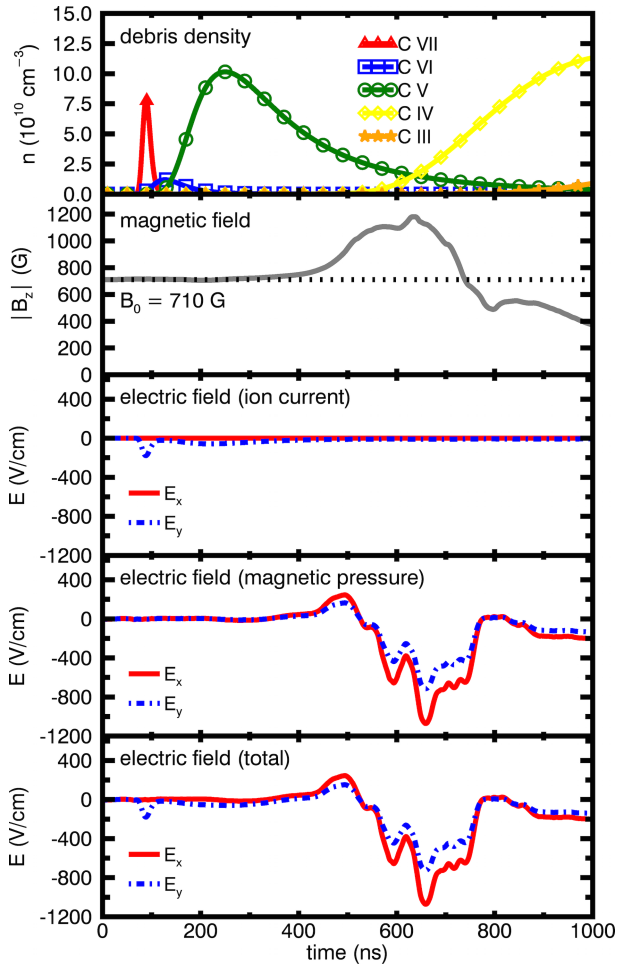

Figure 3.9: Temporal evolution of the electric field in relation to the magnetic field and the debris density at a fixed position, corresponding to the parameters of "Run 3 (0.1X)" in Table 3.2. From top to bottom, the plots show the debris ion densities $n_d\left(\vec{r},t\right)$ (Eq. 3.8), the magnitude of the magnetic field $\vec{B}\left(\vec{r},t\right)$ (Eq. 3.17), and the x and y components of the cross-field ion current term $\vec{E}_{ion}\left(\vec{r},t\right)$ (Eq. 3.32), the magnetic pressure gradient term $\vec{E}_{mag}\left(\vec{r},t\right)$ (Eq. 3.27 and Eq. 3.29), and the total electric field $\vec{E}\left(\vec{r},t\right)$ (Eq. 3.36) at $(x,y) = (30, 0.5)$ cm.

and Fig. 3.10, respectively. As before, each figure plots $n_d\left(\vec{r},t\right)$, $\vec{B}\left(\vec{r},t\right)$, and the x and y components of $\vec{E}_{mag}\left(\vec{r},t\right)$, $\vec{E}_{ion}\left(\vec{r},t\right)$, and $\vec{E}\left(\vec{r},t\right)$ at the position $(x,y) = (30, 0.5)$ cm. Comparison to the results of "Run 1 (3D)" reveals highly differentiated behavior. In Fig. 3.8, corresponding to "Run 2 (10X)," the factor of 10 increase in the total ablated ion number

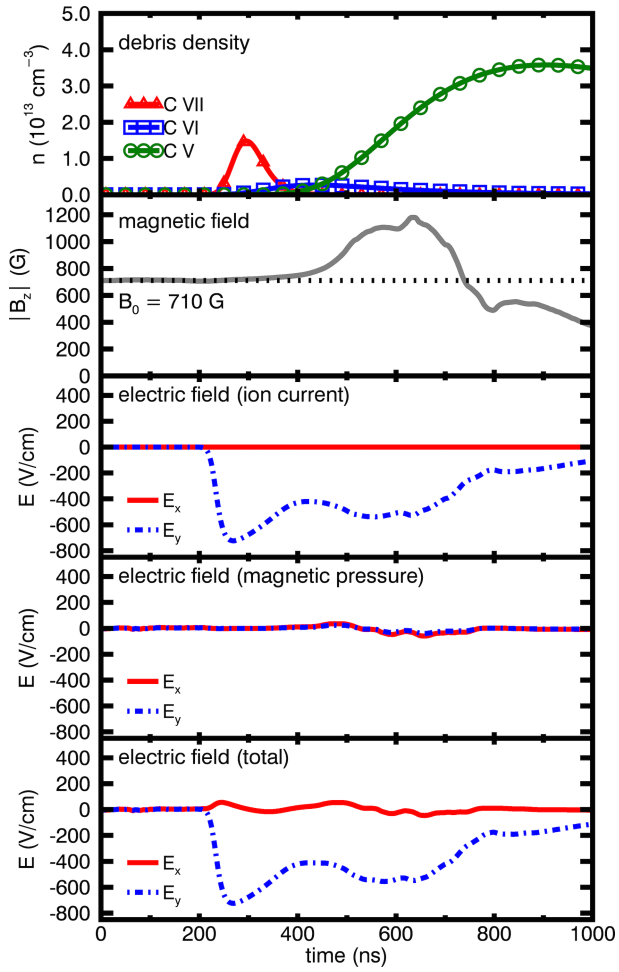

Figure 3.10: Temporal evolution of the electric field in relation to the magnetic field and the debris density at a fixed position, corresponding to the parameters of "Run 4 (2D)" in Table 3.2. From top to bottom, the plots show the debris ion densities $n_d\left(\vec{r},t\right)$ (Eq. 3.8), the magnitude of the magnetic field $\vec{B}\left(\vec{r},t\right)$ (Eq. 3.17), and the x and y components of the cross-field ion current term $\vec{E}_{ion}\left(\vec{r},t\right)$ (Eq. 3.32), the magnetic pressure gradient term $\vec{E}_{mag}\left(\vec{r},t\right)$ (Eq. 3.27 and Eq. 3.29), and the total electric field $\vec{E}\left(\vec{r},t\right)$ (Eq. 3.36) at $(x,y) = (30, 0.5)$ cm.

N_{tot} results in a comparable increase in the densities $n_d\left(\vec{r},t\right)$ of each debris ion charge state. Moreover, due to the energy-conserving factor of ≈ 3 decrease in the debris expansion speeds, the debris arrives at the observation position later in time. The late arrival of the debris postpones the appearance of the ion current term $\vec{E}_{ion}\left(\vec{r},t\right)$ and lowers the local

total plasma density, thereby increasing the magnitude of $\vec{E}_{mag}(\vec{r},t)$ through the inverse density dependence in Eq. 3.29. In Fig. 3.9, corresponding to "Run 3 (0.1X)," the factor of 10 decrease in the total ablated ion number N_{tot} results in a comparable decrease in the densities $n_d(\vec{r},t)$ of each debris ion charge state. Moreover, due to the energy-conserving factor of ≈ 3 increase in the debris expansion speeds, the debris arrives at the observation position earlier in time. The earlier arrival of the debris causes $\vec{E}_{ion}(\vec{r},t)$ to develop sooner. However, despite the faster expansion speeds, the magnitude is smaller. To understand why, it is necessary to recall that the magnitude of $\vec{E}_{ion}(\vec{r},t)$ depends on both the debris expansion speed and the ratio of debris to ambient density, in accordance with Eq. 3.32. In this case, the smaller number of ablated ions causes the latter effect to win, causing a drop in the magnitude. The smaller number of ions also lowers the local total plasma density, thereby increasing the magnitude of $\vec{E}_{mag}(\vec{r},t)$ through the inverse density dependence in Eq. 3.29. In Fig. 3.10, corresponding to "Run 4 (2D)," the ablated ion number N_{tot} and the expansion speeds remain unchanged. However, the debris densities are nearly two orders of magnitude larger due to the two-dimensional debris expansion. The increased debris density results in a dominant $\vec{E}_{ion}(\vec{r},t)$ (which escalates with increasing ratio of the debris density to the ambient density) and a negligible $\vec{E}_{mag}(\vec{r},t)$ (which declines with increasing total plasma density). In summary, the comparison of the four parameter sets of Table 3.2 reveals that a dominant $\vec{E}_{mag}(\vec{r},t)$ characterizes "Run 2 (10X)" and "Run 3 (0.1X)," a dominant $\vec{E}_{ion}(\vec{r},t)$ characterizes "Run 4 (2D)," and comparable $\vec{E}_{mag}(\vec{r},t)$ and $\vec{E}_{ion}(\vec{r},t)$ characterize "Run 1 (3D)."

3.3.2 Simulation of Initial He II Ion Response

The spatiotemporal models of the total laminar electric field $\vec{E}(\vec{r},t)$ (Eq. 3.36) and the magnetic field $\vec{B}(\vec{r},t)$ (Eq. 3.17) allow for a simulation of the initial He II ion response to the explosive debris plasma via the Lorentz force,

$$\frac{d^2\vec{r}(t)}{dt^2} = \frac{d\vec{v}(t)}{dt} = \frac{e}{m_{He}}\left(\vec{E}(\vec{r},t) + \frac{\vec{v}(t)}{c} \times \vec{B}(\vec{r},t)\right). \tag{3.1}$$

As detailed in Section 3.2, the symmetry of the blow-off plane ($z = 0$ cm) requires that $\vec{E}(\vec{r},t)$ only has x and y components (parallel to the plane), while $\vec{B}(\vec{r},t)$ only has a z component (perpendicular to the plane). Because the vector $\vec{v}(t) \times \vec{B}(\vec{r},t)$ is necessarily perpendicular to $\vec{B}(\vec{r},t)$, it follows that the Lorentz force of Eq. 3.1 must also have only x and y components (parallel to the plane). The trajectory of an initially stationary He II ion located anywhere in the blow-off plane is therefore confined to the plane and can be described via two coordinates (x and y).

Utilizing this simplifying principle, a custom simulation code computes the planar trajectories of a distribution of He II ion test particles, each of mass $m_{He} = 6.647 \times 10^{-24}$ g and charge number $Z = 1$. Initially, $N = 10^4$ particles are normally distributed throughout the plane. The distribution follows a two-dimensional Gaussian with the center at $(x_c, y_c) = (32, 6)$ cm and a standard deviation of $\sigma_x = \sigma_y = 9$ cm, designed to approximately match the measured electron density profile of the unperturbed ambient plasma from Fig. 2.3 of Chapter 2. However, particles with initial positions outside of the Langmuir sweep region, where the ambient density is unknown, are not included in the simulation. The test particles are also initially assigned a Maxwellian velocity distribution corresponding to a root-mean-square speed of $v_{rms} \approx 3$ km/s, consistent with the observed Doppler broadening in the unperturbed background. The initial thermal motion only takes place in the plane along x and y, such that the particles remain stationary along z. To perform the simulation, the position $\vec{r}_i(t)$ of the i'th test particle at time t is used to evaluate the local electric and magnetic fields $\vec{E}(\vec{r}_i,t)$ and $\vec{B}(\vec{r}_i,t)$ via Eq. 3.36 and Eq. 3.17, respectively. This, in turn, allows for a calculation of the acceleration $\frac{d^2\vec{r}_i(t)}{dt^2}$ of the i'th particle via Eq. 3.1. The position

particle type	He II ion
particle mass	$m_{He} = 6.647 \times 10^{-24}$ g
particle charge number	$Z = 1$
number of particles	$N = 10^4$
time step	$\Delta t = 0.8$ ns
init. spatial distribution	Gaussian: $(x_c, y_c) = (32, 6)$ cm, $\sigma_x = \sigma_y = 9$ cm
init. velocity distribution	Maxwellian: $v_{rms} \approx 3$ km/s

Table 3.3: Parameters of the custom simulation used to compute the trajectories of a distribution of He II ion test particles.

$\vec{r}_i\,(t)$ and velocity $\vec{v}_i\,(t)$ are then evolved over a small time step, from t to $t + \Delta t$, via the standard linearized equations

$$\vec{v}_i\,(t + \Delta t) = \vec{v}_i\,(t) + \left[\frac{d^2\vec{r}_i\,(t)}{dt^2}\right]\Delta t, \tag{3.37}$$

$$\vec{r}_i\,(t + \Delta t) = \vec{r}_i\,(t) + \vec{v}_i\,(t)\,\Delta t + \frac{1}{2}\left[\frac{d^2\vec{r}_i\,(t)}{dt^2}\right](\Delta t)^2\,. \tag{3.38}$$

The procedure then repeats at the updated positions and velocities of each particle and at the new time. The time step is set to $\Delta t = 0.8$ ns, corresponding to the temporal resolution of the measured magnetic field profile. By comparison to the ~ 100 ns time intervals associated with significant variations in the plasma parameters (see Fig. 3.6, for example), this time step is sufficiently small for an accurate computation of the trajectories. Table 3.3 summarizes the custom simulation parameters.

Up to this point, the parameter models derived in Section 3.2 have invoked the assumption that the explosive debris does not significantly disturb the ambient density profile. Consequently, the ambient electron density has been represented by the time-independent function $n_{e,meas}\,(\vec{r})$, corresponding to the measured electron density profile of Fig. 2.3 in Chapter 2. The present He II ion test particle trace attempts to improve upon this assumption by allowing the ambient density to evolve in time along the trajectories of the test

particles. Specifically, for a particle located at position $\vec{r}_i(t)$ at time t, the evolving ambient electron density $n_{e,time}(\vec{r}_i, t)$ follows from the original static profile, evaluated at the initial position $\vec{r}_i(0)$ of that same particle:

$$n_{e,time}(\vec{r}_i, t) = n_{e,meas}(\vec{r}_i(0)). \tag{3.39}$$

Thus, in the context of Eq. 3.39, "patches" of the initial ambient density profile move with the test particles. While this model ignores the possibility of compression and rarefaction in the ambient density, it nevertheless improves upon the static assumption and eliminates the problem of test particles that move outside of the Langmuir sweep region of Fig. 2.3, where the ambient density is not measured. In the calculation of the test particle trajectories, the evolving ambient density $n_{e,time}(\vec{r}_i, t)$ of Eq. 3.39 is used in place of $n_{e,meas}(\vec{r})$ to evaluate the local $\vec{E}(\vec{r}_i, t)$ and $\vec{B}(\vec{r}_i, t)$.

Fig. 3.11 illustrates the simulated response of the He II ion test particles in relation to the magnetic field and the expanding debris plasma, based on the parameters of "Run 1 (3D)" in Table 3.2 and the simulation configuration of Table 3.3. Specifically, this figure superimposes a random 10% sample of the total test particles over color contours of the magnitude of the magnetic field $\vec{B}(\vec{r}, t)$ and teardrop contours corresponding to the peak density position of each debris ion charge state. The parameters are plotted in the blow-off plane at various times between $t = 375$ ns and $t = 1000$ ns. Initially, at $t = 375$ ns, most of the test particles experience an impulse from only the clockwise azimuthal electric field $\vec{E}_{ion}(\vec{r}, t)$, which develops well ahead of the magnetic compression due to the fast C VII ion current. By $t = 625$ ns, the magnetic compression reaches the central region of the ambient plasma column and causes the particles in that region to experience an additional impulse from the radial-like $\vec{E}_{mag}(\vec{r}, t)$, which develops due to the magnetic field gradients. By this time, the motional response of the particles becomes clearly apparent at the plotted spatial scale. Between $t = 625$ ns and $t = 1000$ ns, the particles in the vicinity of the propagating magnetic compression experience acceleration due to both the azimuthal $\vec{E}_{ion}(\vec{r}, t)$ and the radial-like $\vec{E}_{mag}(\vec{r}, t)$. As calculated in Fig. 3.5 and schematically illustrated in Fig. 3.7, the vector sum of the two contributions results in an asymmetrically structured total electric field

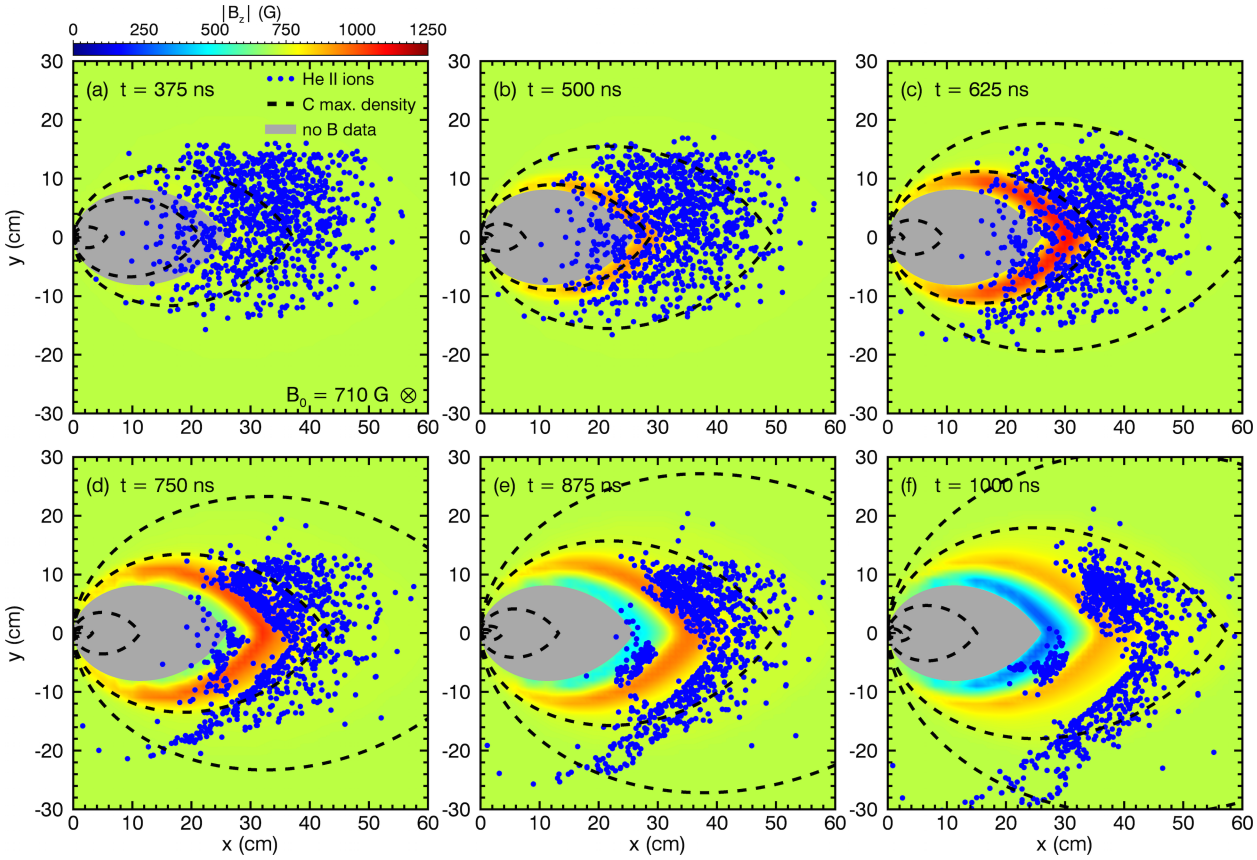

Figure 3.11: Spatiotemporal evolution of the He II ion test particles (blue dots), corresponding to the parameters of "Run 1 (3D)" in Table 3.2 and the simulation configuration of Table 3.3. Only 10% of the total test particles are plotted. The particles are superimposed on a color contour of the magnitude of the magnetic field $\vec{B}\,(\vec{r},t)$ (Eq. 3.17), which is directed into the page. The teardrops (dashed black lines) indicate the positions of maximum density corresponding to each debris ion charge state, in accordance with Eq. 3.8. The outermost teardrop represents C VII (the fastest charge state), the next teardrop represents C VI (the second fastest charge state), and so on. The grayed-out region represents where the magnetic field is not diagnosed and set to the background value of 710 G.

$\vec{E}(\vec{r},t)$, characterized by small $+y$ components in the upper half of the blow-off plane ($y > 0$ cm) and large $-y$ components in the lower half ($y < 0$ cm). The effect of this asymmetry becomes fully apparent by $t = 1000$ ns, as the particles in the lower half of the plane have acquired large velocity components in the $-y$ direction, while the particles in the upper half of the plane have acquired relatively small velocities in the $+y$ direction. In addition to the impulse from the electric field, the test particles also experience a $\vec{v} \times \vec{B}$ magnetic Lorentz force that causes gyration. However, because the plotted time interval corresponds to only about one-quarter of a gyro-period ($T = \frac{2\pi m_{He}c}{eB_0} \approx 4$ μs for $B_0 = 710$ G), the motion is dominated by the initial electric field impulse. It should also be noted that, while most of the test particles accelerate ahead of the magnetic compression, a small subset appears to become confined within the diamagnetic cavity.

By analogy to Fig. 3.11, the He II ion test particle response corresponding to the parameters of "Run 2 (10X)," "Run 3 (0.1X)," and "Run 4 (2D)" from Table 3.2 is shown in Fig. 3.12, Fig. 3.13, and Fig. 3.14, respectively. Comparison to the results of "Run 1 (3D)" reveals highly differentiated behavior. In both Fig. 3.12 and Fig. 3.13, corresponding to "Run 2 (10X)" and "Run 3 (0.1X)," the final configuration of the test particles at $t = 1000$ ns appears roughly symmetric about the blow-off axis. More specifically, the particle population splits into two groups in the upper and lower halves of the plane, which acquire comparable velocity components in $+y$ and $-y$, respectively. This results from the dominant radial-like contribution from $\vec{E}_{mag}(\vec{r},t)$, as demonstrated in the temporal evolution plots of Fig. 3.8 and Fig. 3.9. In Fig. 3.14, corresponding to "Run 4 (2D)," nearly all of the test particles acquire a large velocity in the $-y$ direction, ending up in the lower half of the plane by $t = 1000$ ns. This is attributed to the dominant clockwise azimuthal contribution from $\vec{E}_{ion}(\vec{r},t)$, as demonstrated in the temporal evolution plots of Fig. 3.10. The comparisons reveal that only in the case of Fig. 3.11, corresponding to "Run 1 (3D)," do the comparable magnitudes of $\vec{E}_{ion}(\vec{r},t)$ and $\vec{E}_{mag}(\vec{r},t)$ result in a distinct asymmetry, with large velocity components in the $-y$ direction and small velocity components in the $+y$ direction. As will be demonstrated in Section 3.4, this asymmetry accounts for the observed Doppler broadening.

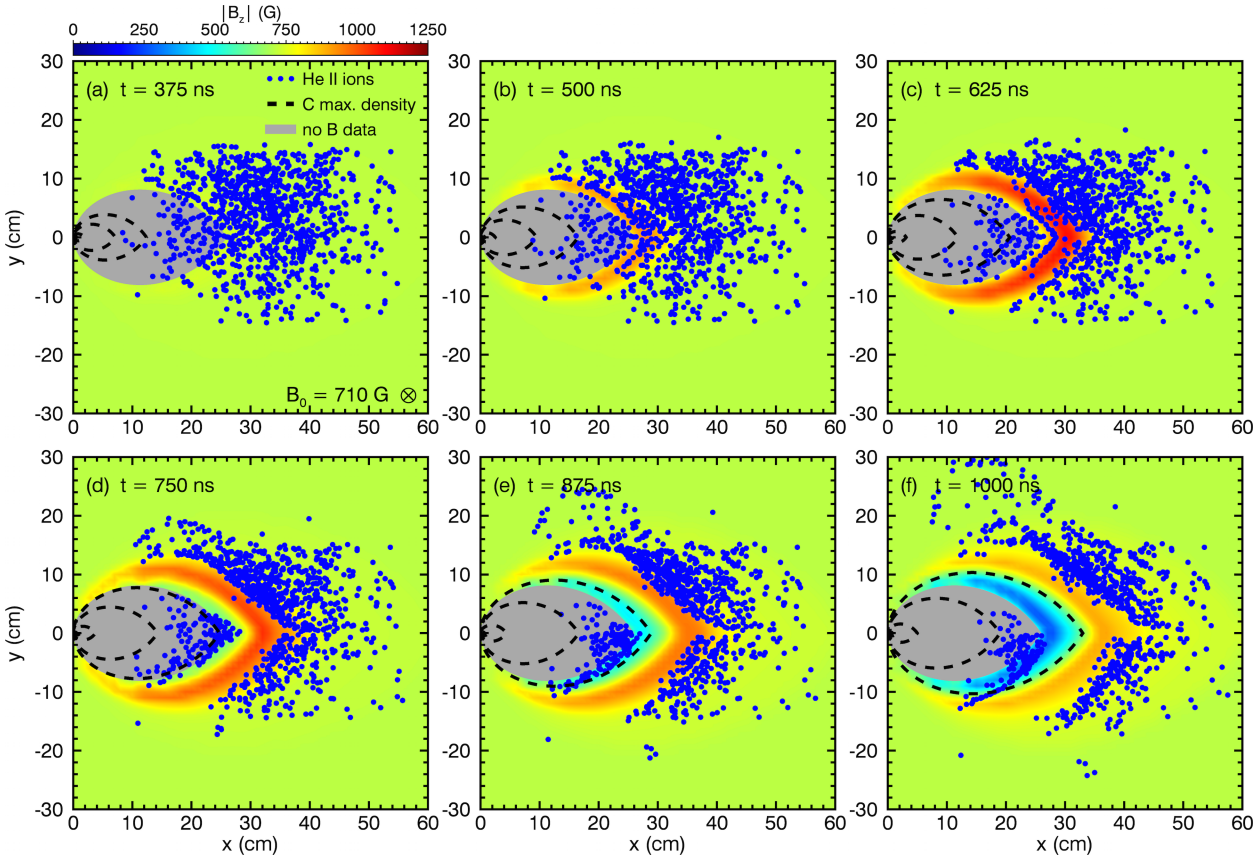

Figure 3.12: Spatiotemporal evolution of the He II ion test particles (blue dots), corresponding to the parameters of "Run 2 (10X)" in Table 3.2 and the simulation configuration of Table 3.3. Only 10% of the total test particles are plotted. The particles are superimposed on a color contour of the magnitude of the magnetic field $\vec{B}\,(\vec{r},t)$ (Eq. 3.17), which is directed into the page. The teardrops (dashed black lines) indicate the positions of maximum density corresponding to each debris ion charge state, in accordance with Eq. 3.8. The outermost teardrop represents C VII (the fastest charge state), the next teardrop represents C VI (the second fastest charge state), and so on. The grayed-out region represents where the magnetic field is not diagnosed and set to the background value of 710 G.

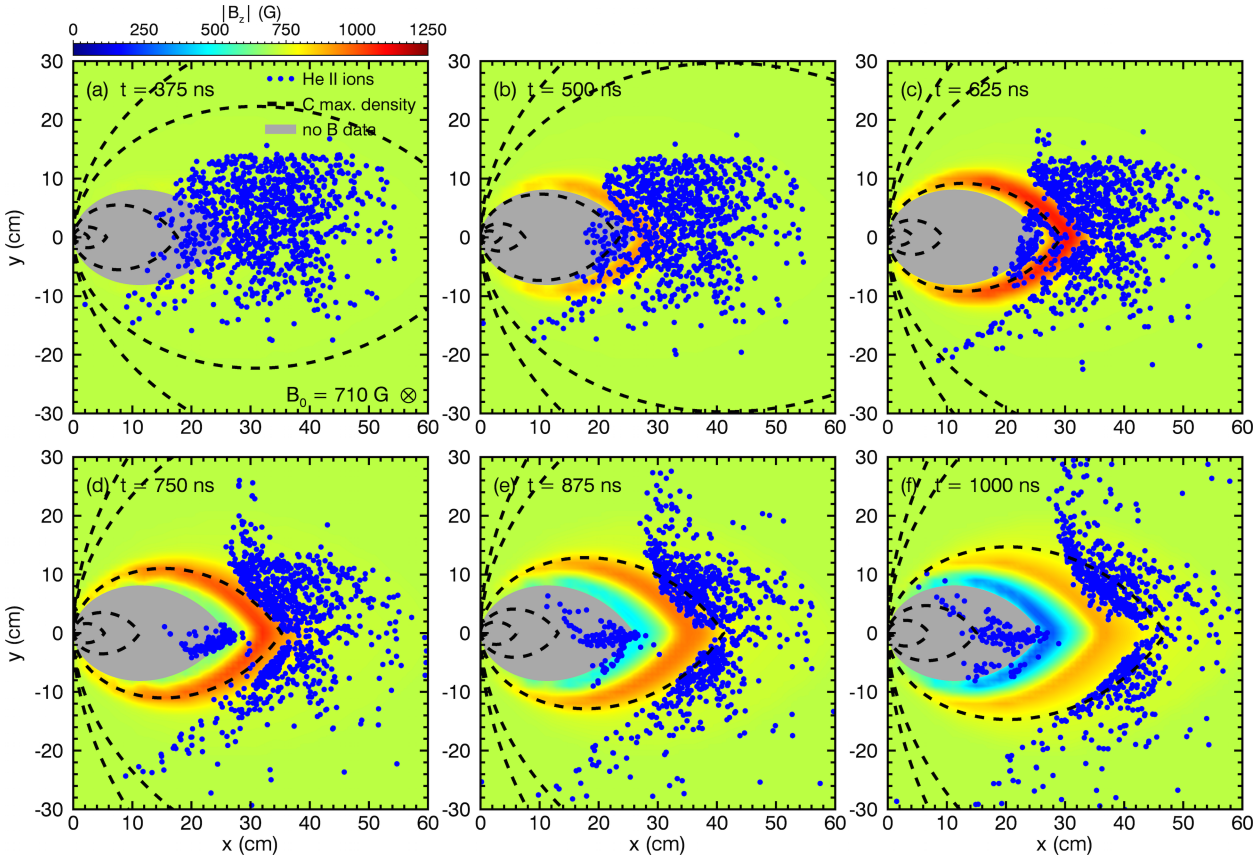

Figure 3.13: Spatiotemporal evolution of the He II ion test particles (blue dots), corresponding to the parameters of "Run 3 (0.1X)" in Table 3.2 and the simulation configuration of Table 3.3. Only 10% of the total test particles are plotted. The particles are superimposed on a color contour of the magnitude of the magnetic field $\vec{B}\,(\vec{r},t)$ (Eq. 3.17), which is directed into the page. The teardrops (dashed black lines) indicate the positions of maximum density corresponding to each debris ion charge state, in accordance with Eq. 3.8. The outermost teardrop represents C VII (the fastest charge state), the next teardrop represents C VI (the second fastest charge state), and so on. The grayed-out region represents where the magnetic field is not diagnosed and set to the background value of 710 G.

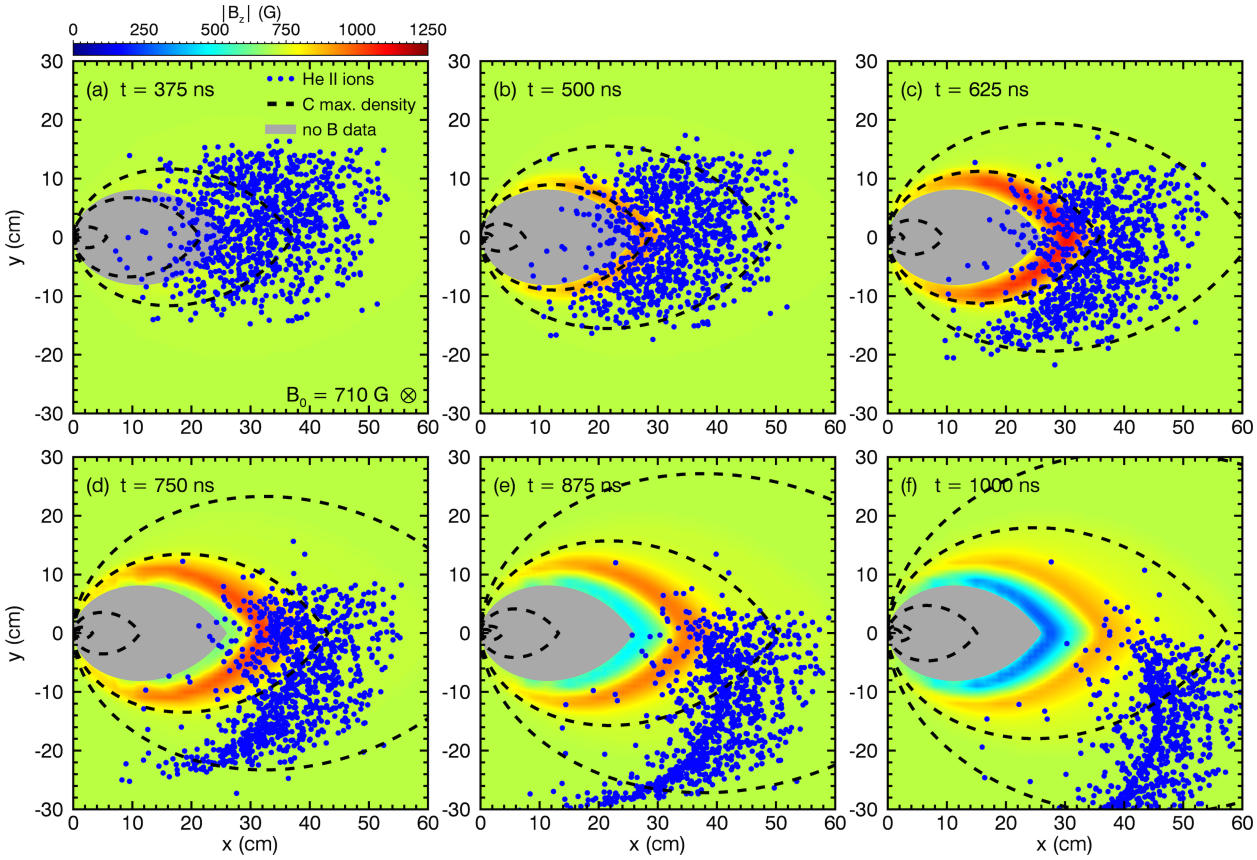

Figure 3.14: Spatiotemporal evolution of the He II ion test particles (blue dots), corresponding to the parameters of "Run 4 (2D)" in Table 3.2 and the simulation configuration of Table 3.3. Only 10% of the total test particles are plotted. The particles are superimposed on a color contour of the magnitude of the magnetic field $\vec{B}\,(\vec{r},t)$ (Eq. 3.17), which is directed into the page. The teardrops (dashed black lines) indicate the positions of maximum density corresponding to each debris ion charge state, in accordance with Eq. 3.8. The outermost teardrop represents C VII (the fastest charge state), the next teardrop represents C VI (the second fastest charge state), and so on. The grayed-out region represents where the magnetic field is not diagnosed and set to the background value of 710 G.

3.4 Comparison of Model Results to Experimental Data

This section compares the modeled results from Section 3.3 to the experimental data presented in Chapter 2, providing a quantitative evaluation of the theoretical framework of laminar collision-less coupling. Utilizing the simulated He II ion test particle motion in combination with collisional-radiative modeling, synthetic wavelength profiles of a He II ion spectral line are constructed for all four parameter sets of Table 3.2 and compared to the spatially and temporally integrated spectroscopic measurements. In addition, the computed electric field corresponding the four parameter sets is compared to the experimentally measured magnetic field via the Maxwell-Faraday equation in order to investigate the self-consistency of the computational approach. Finally, the validity of the ballistic debris expansion model is examined through the requirement of energy conservation.

3.4.1 Comparison to Spectroscopic Data

As demonstrated in Fig. 2.11 and Fig. 2.12 of Chapter 2, spectroscopic measurements of the He II 468.6 nm line reveal significant, asymmetric Doppler broadening in response to the explosive debris plasma, indicative of He II ion acceleration. Specifically, the predominant blue shift detected in the first spectrum (time-integrated from $t = 500$ ns to $t = 1000$ ns and line-integrated along y at $x = 30$ cm) demonstrates an initial impulse transverse to the debris expansion in the $-y$ direction, qualitatively consistent with the cross-field ion current term of the laminar electric field (Eq. 1.9). The predominant red shift measured in the second spectrum (time-integrated from $t = 4000$ ns to $t = 4500$ ns and line-integrated along y at $x = 45$ cm) then corresponds to the subsequent gyration of the accelerated He II ions in the magnetic field. However, the interpretation based on the cross-field ion current term alone cannot fully account for the results, as the predominantly blue-shifted spectrum also contains a small red-shifted component and vice versa. In addition, the spatially and temporally integrated spectra sample a large population of ions of differing trajectories, making it difficult to interpret the atypical Doppler-broadened profiles. In order to better

understand the measurements and examine consistency with the theoretical framework of laminar coupling, synthetic wavelength profiles of the He II 468.6 nm line are constructed by utilizing the test particle simulations of Section 3.3 in combination with collisional-radiative modeling. Because the simulations rely on the assumption of a ballistic debris expansion, the validity of the calculated results deteriorates as the debris expends an increasing amount of its initial kinetic energy, primarily through coupling to the ambient plasma and expulsion of the magnetic field. The present analysis thus confines itself only to the reconstruction of the earliest, predominantly blue-shifted spectrum, when the ballistic condition is best approximated.

As detailed in Chapter 2, generation of a synthetic wavelength profile of the He II 468.6 nm line requires knowledge of the three primary line broadening mechanisms: the instrument function S_{inst}, the fine structure splitting S_{fs}, and the Doppler broadening S_{Dop}. As before, S_{inst} follows from an experimental measurement of a calibration line with an intrinsic width smaller than the resolution limit of the spectroscopic setup, while S_{fs} is derived from collisional-radiative simulations in PrismSPECT.[5] However, the Doppler contribution S_{Dop} no longer follows from the Maxwellian profile of the unperturbed, thermalized ambient plasma but instead depends on the complex velocity distributions of the accelerated, fluorescing He II ions along the optical collection axis. Presently, the velocity distributions are obtained from the simulated trajectories of the He II ion test particles. To match the configuration of the temporally and spatially integrated spectroscopic measurement, the extracted distribution samples only the subset of particles located at $x = 30 \pm 0.5$ cm between $t = 500$ ns and $t = 1000$ ns. Because the fiber probe collects light along the y axis, the distribution samples only the y component of the particle velocities. However, this subset of the velocities is still insufficient for an accurate reconstruction of the He II 468.6 nm profile because it potentially includes particles outside of the intensified region, which do not contribute to the measured spectrum. From Fig. 3.3, it follows that the He II intensification boundary

[5]The PrismSPECT simulations assume the steady-state, ambient conditions of Table 2.2 in Chapter 2 and do not take into account the complex density and temperature fluctuations introduced by the explosive debris plasma. As a result, the simulated fine structure profile S_{fs} is only an approximation. However, this has little consequence on the final synthetic spectrum, which is dominated by the Doppler contribution.

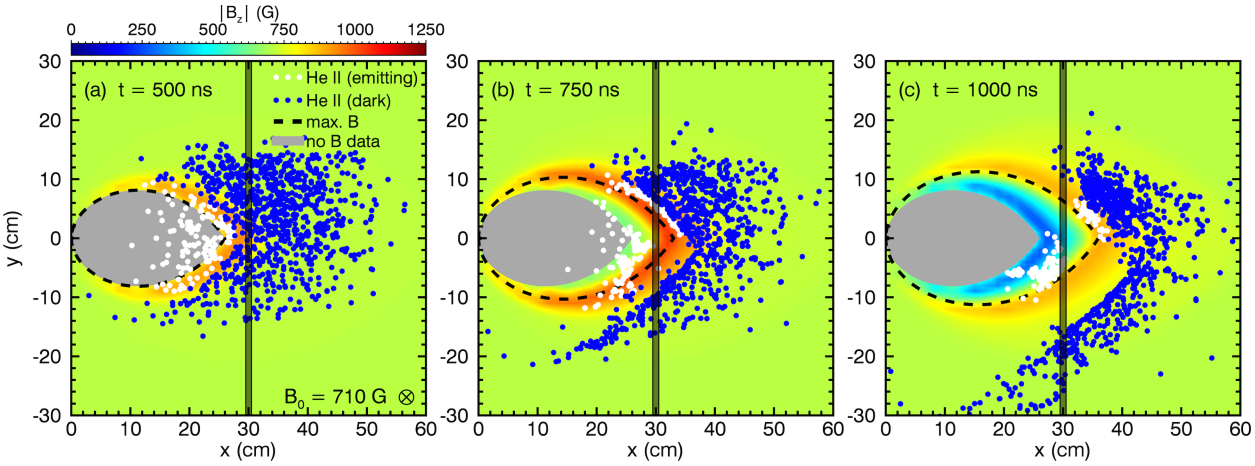

Figure 3.15: He II ion test particle simulation corresponding to the parameters of "Run 1 (3D)" in Table 3.2, showing the subset of emitting particles (white dots) located within the region bounded by $\delta = 2$ cm past the peak magnetic compression (dashed black line) and the dark particles (blue dots) outside of the intensified region. The gray line at $x = 30 \pm 0.5$ cm denotes the optical collection axis. The synthetic He II 468.6 nm spectrum is constructed by sampling the velocity y components of just the emitting subset of particles that overlap the collection axis.

in the blow-off plane roughly corresponds to the teardrop extrapolation of the peak magnetic compression. Thus, to construct the synthetic spectrum, only the subset of "emitting" test particles located within the intensified region bounded by the magnetic compression is used.[6] The extraction of the test particle velocity distributions is demonstrated in Fig. 3.15, which shows the test particle simulation corresponding to "Run 1 (3D)" in Table 3.2 and highlights both the optical collection axis at $x = 30 \pm 0.5$ cm and the subset of emitting particles located within the peak compression.

Fig. 3.16 shows the resulting distributions of the velocity y components for all four parameter sets of Table 3.2, extracted analogously to Fig. 3.15. Both the distribution of all the particles within $x = 30 \pm 0.5$ cm and the distribution of just the emitting subset of those

[6]More accurately, the boundary of the intensified region is assumed to be slightly ahead of the teardrop corresponding to the peak magnetic compression. This distance ahead of the compression, denoted δ, is treated as a free parameter and set to $\delta = 2$ cm in the results presented here, consistent with Fig. 3.3.

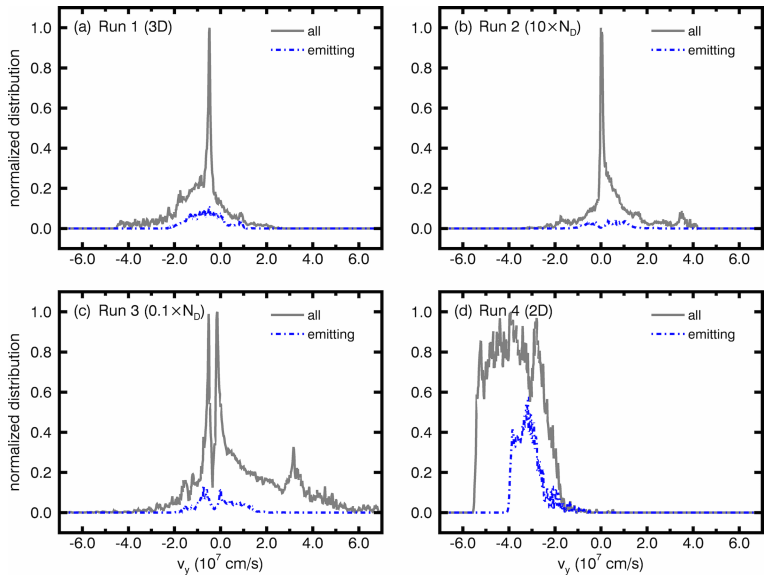

Figure 3.16: Distributions of the velocity y components from the He II ion test particle simulations corresponding to all four parameter sets of Table 3.2. The distributions are temporally integrated from $t = 500$ ns to $t = 1000$ ns and spatially integrated along y at $x = 30 \pm 0.5$ cm. Both the distribution of all the particles within $x = 30 \pm 0.5$ cm (gray solid line) and the distribution of just the emitting subset of those particles (dashed blue line) are shown.

particles are shown. A common feature of all four runs is that the emitting test particle population is significantly slower than the fastest particles, which quickly escape the intensification region. For example, in "Run 1 (3D)," the fastest particles of the entire distribution acquire a velocity component of ≈ 400 km/s in the $-y$ direction, while the emitting particles that actually contribute to a Doppler-broadened spectrum only achieve ≈ 200 km/s in the same direction. The velocity distributions also generally correspond to the previously assessed behavior of the electric fields. In "Run 1 (3D)," the asymmetric electric field structure caused by the comparable magnetic pressure gradient and cross-field ion current terms (see Fig. 3.5 and Fig. 3.7) causes particles to acquire faster velocities in the $-y$ direction and relatively slower velocities in the $+y$ direction. In "Run 2 (10X)" and "Run 3 (0.1X)," the dominant radial-like contribution from the magnetic pressure gradient term, in combination

with the small offset of the initial test particle distribution above the blow-off axis, results in fast velocities in the $+y$ direction and relatively slower velocities in the $-y$ direction. In "Run 4 (2D)," the dominant azimuthal contribution from the cross-field ion current term causes all of the particles to acquire velocity components in the $-y$ direction. In all of the distributions, the test particles acquire speeds significantly faster than the initial thermal average of $v_{rms} \approx 3$ km/s, indicative of significant acceleration due to the electric field.

The velocity y component distributions of Fig. 3.16 corresponding to just the emitting subset of the test particles define the function $f(v_y)$. Under the assumption that all of the particles embodied in the distribution emit at equal intensities, the wavelength profile of the Doppler contribution S_{Dop} follows from the standard Doppler shift relation

$$S_{Dop}(\lambda) = C \times f\left[v_y = c\left(\frac{\lambda - \lambda_c}{\lambda_c}\right)\right], \tag{3.40}$$

where λ is the independent variable indicating the wavelength, λ_c is the central wavelength of the spectral line, c is the speed of light, and C is a normalization constant.[7] Test particles with velocity components in the $-y$ direction (towards the collecting fiber probe) contribute a blue-shifted spectrum ($\lambda < \lambda_c$), while those moving in the $+y$ direction (away from the collecting fiber probe) contribute a red-shifted spectrum ($\lambda > \lambda_c$). The total synthetic wavelength profile S_{tot} of the He II 468.6 nm line then follows from a convolution of the experimentally measured S_{inst}, the PrismSPECT-simulated S_{fs}, and the test particle-generated S_{Dop} of Eq. 3.40, such that

$$S_{tot} = S_{inst} \otimes S_{fs} \otimes S_{Dop}. \tag{2.2}$$

Fig. 3.17 demonstrates the construction of the synthetic spectrum S_{tot} in accordance with Eq. 2.2 for the parameters corresponding to "Run 1 (3D)" in Table 3.2. The spectral width of the Doppler contribution S_{Dop} significantly exceeds that of S_{inst} and S_{fs} and consequently

[7]Because the He II 468.6 nm line actually consists of a closely spaced series of lines due to fine structure, each with a slightly different central wavelength λ_c, the Doppler relation of Eq. 3.40 must technically be applied to each fine structure component individually. The profile $S_{Dop}(\lambda)$ then follows from an intensity-weighted sum over all the components. However, it was verified that $S_{Dop}(\lambda)$ can be equivalently obtained by assuming just a single component with a suitable weighted average value for λ_c. In the present analysis, the utilized PrismSPECT fine structure profile in combination with NIST wavelength values yields $\lambda_c = 468.5735$ nm.

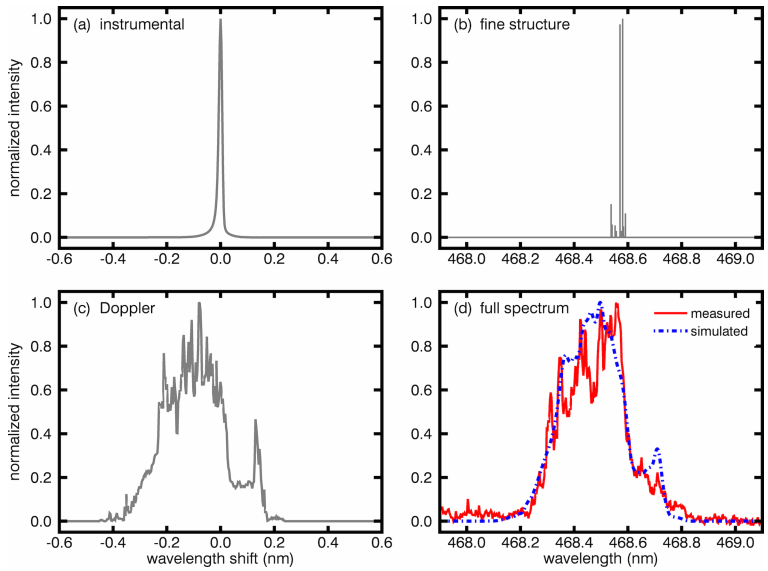

Figure 3.17: Construction of the synthetic spectrum S_{tot} corresponding to the parameters of "Run 1 (3D)" in Table 3.2. The simulated spectrum is generated via a convolution of (a) the experimentally measured instrument function S_{inst}, (b) the PrismSPECT-simulated fine structure profile S_{fs}, and (c) the Doppler profile S_{Dop} of Eq. 3.40, which follows from the emitting test particle velocity distributions of Fig. 3.16. In (d), the total simulated line shape S_{tot} (dashed blue line) is compared to the corresponding measured profile of the He II 468.6 nm line (solid red line), time-integrated from $t = 500$ ns to $t = 1000$ ns and line-integrated along y at $x = 30$ cm. The comparison reveals excellent agreement.

dominates the final line shape of S_{tot}. Comparison to the corresponding spectroscopic measurement of the He II 468.6 nm line in Fig. 2.11 of Chapter 2 (time-integrated from $t = 500$ ns to $t = 1000$ ns and line-integrated along y at $x = 30$ cm) reveals an excellent agreement. The simulated spectrum reproduces all the salient features of the measured wavelength profile, including the non-Maxwellian asymmetric broadening, the predominant blue shift, and the small red shift.

By analogy to Fig. 3.17, Fig. 3.18 compares the synthetic spectra corresponding to all four parameter sets of Table 3.2 to the same measured wavelength profile. The comparisons reveal that the best agreement follows from the experimentally realistic parameters of "Run 1

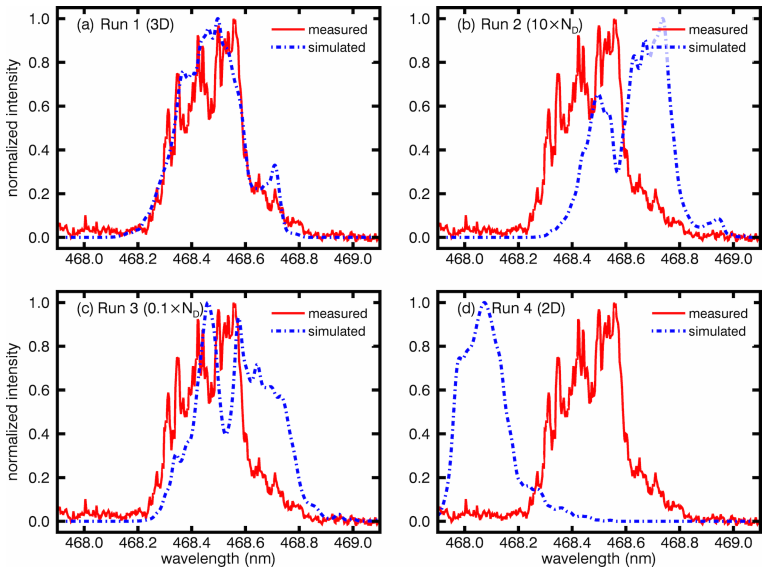

Figure 3.18: Comparison of the synthetic spectra (dashed blue lines) corresponding to all four parameter sets of Table 3.2 to the measured profile of the He II 468.6 nm line (solid red line), by analogy to Fig. 3.17. The best agreement follows from the experimentally realistic parameters of "Run 1 (3D)."

(3D)," where the comparable contributions of the radial-like magnetic pressure gradient term and azimuthal cross-field ion current term result in an asymmetric electric field structure (see Fig. 3.5 and Fig. 3.7) that generates a predominant blue shift and a small red shift. By contrast, in "Run 2 (10X)" and "Run 3 (0.1X)," the dominant radial-like magnetic pressure gradient term results in an excessive red shift, while in "Run 4 (2D)," the dominant azimuthal cross-field ion current term results in an excessive blue shift.

The excellent agreement corresponding to "Run 1 (3D)" in Fig. 3.18 demonstrates that the strong asymmetric Doppler broadening observed in the He II 468.6 nm line (Fig. 2.11 of Chapter 2) is not only qualitatively but also quantitatively consistent with initial He II ion acceleration due to the laminar electric field (Eq. 1.9), which develops as a result of the explosive debris plasma expansion. However, in contrast to the simplified qualitative picture of Fig. 2.12, both the cross-field ion current term *and* the magnetic pressure gradient term of the laminar field must be taken into account in order to fully explain the observed spectrum.

Furthermore, the significantly worse fits produced by the parameters of "Run 2 (10X)," "Run 3 (0.1X)," and "Run 4 (2D)," which intentionally deviate from the HELIOS results utilized by "Run 1 (3D)," indicate self-consistency between the HELIOS computations, the plasma parameter models derived in Section 3.2, and the measured He II 468.6 nm spectrum. The consistency of the modeled results with the experimental measurements also suggests that, while the observed Doppler broadening implies maximum He II ions speeds of ≈ 200 km/s, the measurements fail to capture an optically invisible population accelerated above ≈ 400 km/s (see Fig. 3.15 and Fig. 3.16).

3.4.2 Consistency with Maxwell-Faraday Equation

By contrast to the methodology of hybrid simulation codes, which evolve the plasma parameters, the electric field, and the magnetic field self-consistently via Maxwell's equations, the computational approach of this chapter has utilized imposed predetermined plasma parameter models that allow for a calculation of the electric field via Eq. 1.9. As a result, the electric field is not guaranteed to be Maxwell-consistent. In order to investigate its validity, the computed electric field is compared to the experimentally measured magnetic field via the Maxwell-Faraday equation:

$$\vec{\nabla} \times \vec{E}\left(\vec{r},t\right) = -\frac{1}{c}\frac{\partial \vec{B}\left(\vec{r},t\right)}{\partial t}. \tag{3.41}$$

Substitution of Eq. 3.36 for $\vec{E}\left(\vec{r},t\right)$ and Eq. 3.17 for $\vec{B}\left(\vec{r},t\right)$ into the left-hand and right-hand sides of Eq. 3.41 yields

$$\vec{\nabla} \times \vec{E}\left(\vec{r},t\right) = \vec{\nabla} \times \left(\vec{E}_{mag}\left(\vec{r},t\right) + \vec{E}_{ion}\left(\vec{r},t\right)\right), \tag{3.42}$$

$$-\frac{1}{c}\frac{\partial \vec{B}\left(\vec{r},t\right)}{\partial t} = -\frac{1}{c}\frac{\partial B_{z,meas}\left(x,t\right)}{\partial t}\hat{z}, x \equiv \frac{r}{\exp\left(-\theta/\theta_0\right)\cos\theta}, \tag{3.43}$$

where $\vec{E}_{ion}\left(\vec{r},t\right)$ follows from Eq. 3.32, $\vec{E}_{mag}\left(\vec{r},t\right)$ follows from Eq. 3.27 and Eq. 3.29, and $B_{z,meas}\left(x,t\right)$ corresponds to the measured magnetic field profile along the blow-off axis. Eq. 3.43 is understood to be valid only in the blow-off plane, where the magnetic field only has a z component.

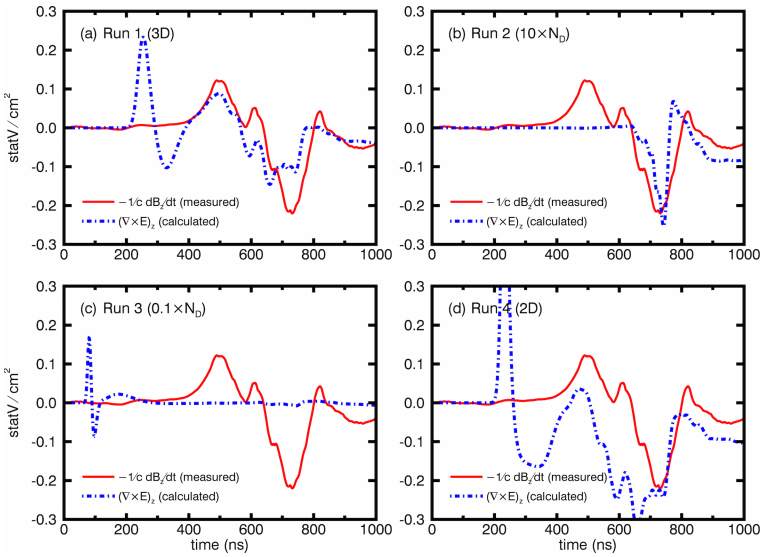

Figure 3.19: Consistency of the calculated electric field with the Maxwell-Faraday equation for all four parameter sets of Table 3.2. The plots compare the curl of the calculated electric field (dashed blue line, Eq. 3.42) to the time derivative of the measured magnetic field (solid red line, Eq. 3.43) at the position $(x, y) = (30, 0.5)$ cm. The best agreement follows from the experimentally realistic parameters of "Run 1 (3D)."

Fig. 3.19 compares the temporal evolution of the curl of the computed electric field (Eq. 3.42) to the time derivative of the measured magnetic field (Eq. 3.43) at a fixed position in space for all four parameter sets of Table 3.2. The evolution is plotted between $t = 0$ ns and $t = 1000$ ns at the position $(x, y) = (30, 0.5)$ cm, near the center of the ambient plasma column and just above the blow-off axis. The comparisons reveal that, while none of the computed electric fields corresponding to the four parameter sets perfectly satisfy the Maxwell-Faraday equation, the experimentally realistic parameters of "Run 1 (3D)" provide the best agreement. In fact, with the exception of the large perturbation in the curl of the computed electric field between $t \approx 200$ ns and $t \approx 400$ ns, "Run 1 (3D)" satisfies the Maxwell-Faraday equation reasonably well. The significantly worse agreement produced by the parameters of "Run 2 (10X)," "Run 3 (0.1X)," and "Run 4 (2D)," which intentionally deviate from the HELIOS results utilized by "Run 1 (3D)," indicates self-consistency between the HELIOS computations, the plasma parameter models derived in Section 3.2, and the

measured magnetic field profile.

The source of the early-time discrepancy corresponding to "Run 1 (3D)" in Fig. 3.19 can be inferred from Fig. 3.6, which plots the temporal evolution of the debris densities, magnetic fields, and electric field components at the same position. According to the debris expansion model, the fast C VII ions (charge number $Z = 6$) stream at average speeds of $\bar{V}_d \approx 1000$ km/s, arriving at the observation position $(x, y) = (30, 0.5)$ cm between $t \approx 200$ ns and $t \approx 400$ ns. Moreover, because the ions outrun the magnetic compression and diamagnetic cavity, they primarily stream through a uniform background magnetic field with a magnitude of $B_0 = 710$ G. In the model, the cross-field ion currents produce an electric field $\vec{E}_{ion}(\vec{r}, t)$, which necessarily contributes to the computed curl. However, a quick calculation of the C VII gyro-radius corresponding to the expansion speed and magnetic field yields $\rho = \frac{m_C c \bar{V}_d}{Z e B_0} \approx 29$ cm. Thus, in the actual experiment, most of the C VII ions fail to reach the observation position due to Lorentz gyration, and as a result, an electric field due to $\vec{E}_{ion}(\vec{r}, t)$ does not develop there at this time. The discrepancy thus corresponds to the limitation of the ballistic debris expansion model, which does not take into account debris deceleration or gyration.[8]

3.4.3 Energy Considerations

As previously described, the computational approach utilized throughout this chapter assumes a ballistic debris plasma expansion, such that the debris ions freely steam from the origin at constant velocity and the total debris kinetic energy remains unchanged. Because the explosive debris plasma in the actual experiment gradually expends its initial kinetic energy, the validity of the simulated results necessarily deteriorates at later times. In order to investigate the soundness of the ballistic approximation, a rough estimate of the energy balance is extracted from the modeled results corresponding to the experimentally realistic

[8]Though the C VII ions fail to reach the position $(x, y) = (30, 0.5)$ cm due to gyration, it is not valid to completely disregard this debris charge state in the previously described construction of the synthetic spectrum at $x = 30 \pm 0.5$ cm. This is because the C VII ions can nevertheless accelerate ambient He II ions at positions closer to the origin ($x < 30$ cm), causing the ambient ions to stream through the collection axis and contribute to the spectrum later in time. Stated more generally, the spatially and temporally integrated spectra depend on highly non-local effects.

parameters of "Run 1 (3D)" from Table 3.2. In accordance with the theoretical considerations of Chapter 1, the debris plasma loses kinetic energy predominantly through coupling to the ambient plasma and expulsion of the magnetic field. Under the assumption that the electrons carry negligible kinetic energy, the debris ion kinetic energy $E_d(t)$ thus follows from

$$E_d(t) = E_K - E_a(t) - E_B(t), \tag{3.44}$$

where E_K is the initial debris ion kinetic energy, $E_a(t)$ is the extra kinetic energy acquired by the ambient ions as a result of debris-ambient interaction, and $E_B(t)$ is the energy expended on expulsion of the magnetic field. Eq. 3.44 ignores energy losses due to plasma waves, instabilities, electron acceleration, and radiation. In addition, the energy stored within the laminar electric fields that arise in the course of debris-ambient interaction is assumed to be negligible, as easily verified for the ~ 1 kV/cm magnitudes expected under the present conditions.

The initial C debris ion kinetic energy $E_K = 94$ J follows directly from Eq. 3.34 and Eq. 3.35 and the parameters of "Run 1 (3D)" in Table 3.2. The expelled magnetic field energy $E_B(t)$ is approximated by assuming full expulsion of the background magnetic field $B_0 = 710$ G within the time-dependent volume $V_B(t)$,

$$E_B(t) = \left(\frac{B_0^2}{8\pi}\right) V_B(t), \tag{3.45}$$

where $V_B(t)$ corresponds to the three-dimensional teardrop of Eq. 3.5 with the cusp position $r_0(t)$ set to the measured position of the peak magnetic compression. Finally, the extra kinetic energy $E_a(t)$ acquired by ambient He ions due to debris-ambient interaction follows from

$$E_a(t) = \frac{1}{2} m_{He} \sum\nolimits_a \left[\int_r n_a(\vec{r}, t)\, v_a^2(\vec{r}, t)\, \mathrm{d}^3\vec{r} \right]. \tag{3.46}$$

In Eq. 3.46, $n_a(\vec{r}, t)$ and $v_a(\vec{r}, t)$ are the density and speed of each ambient ion charge state, the integral is taken over the perturbed region of space in which He ions have been accelerated above their initial thermal speeds as a result of the explosive debris, the sum is taken over the charge states He II and He III, and m_{He} is the atomic mass of He. The expression also assumes

that the initial kinetic energy of the of the thermal, unperturbed ambient ions is relatively negligible. Evaluation of Eq. 3.46 is highly non-trivial, as it requires detailed knowledge of the spatiotemporal response of the ambient ions. In order to obtain an approximate solution, the test particle simulation of Fig. 3.11 is utilized, along with several simplifying assumptions.[9] First, the integration region is assumed to span the teardrop volume of Eq. 3.5 with the cusp $r_0(t)$ set to the position of C VII maximum density along the blow-off axis. (In other words, He ions located outside the reach of the fastest C VII charge state are assumed to be largely unaffected by the debris-ambient interaction). Second, the ambient plasma is assumed to consist entirely of He II ions (charge number $Z = 1$), such that the ambient ion density $n_a(\vec{r}, t)$ follows directly from the evolving ambient electron density profile of Eq. 3.39 by quasi-neutrality. And third, because the test particle simulation contains only the blow-off plane ($z = 0$ cm), ambient ion velocities and densities are assumed to be invariant along the z direction. Utilizing these assumptions, Eq. 3.46 is then evaluated by visiting each volume element within the C VII teardrop, computing the average kinetic energy per test particle within that volume element based on the simulation of Fig. 3.11, and multiplying the average kinetic energy by the actual number of He II ions expected to inhabit that volume element based on the ambient density profile.

Fig. 3.20 shows the temporal evolution of the magnetic energy $E_B(t)$ (Eq. 3.45), the extra acquired He II ion kinetic energy $E_a(t)$ (Eq. 3.46), and the remaining debris kinetic energy $E_d(t)$ (Eq. 3.44) between $t = 500$ ns and $t = 1000$ ns, based on the parameters of "Run 1 (3D)" in Table 3.2. The results demonstrate that the debris ions lose $\approx 36\%$ of their initial kinetic energy by $t = 1000$ ns, which corresponds to a $\approx 20\%$ decrease in speed on average. This non-negligible amount highlights the limitation of the ballistic approximation and very roughly suggests that the computed test particle velocities between $t = 500$ ns and $t = 1000$ ns (the time interval used to construct the synthetic spectra) are only valid to within $\approx 20\%$. The analysis also reveals that a comparable amount of energy couples

[9]The test particle simulations presuppose the ballistic debris expansion model, which is the very assumption being questioned presently. Their use in this context provides only a first-order approximation of the ambient ion kinetic energy.

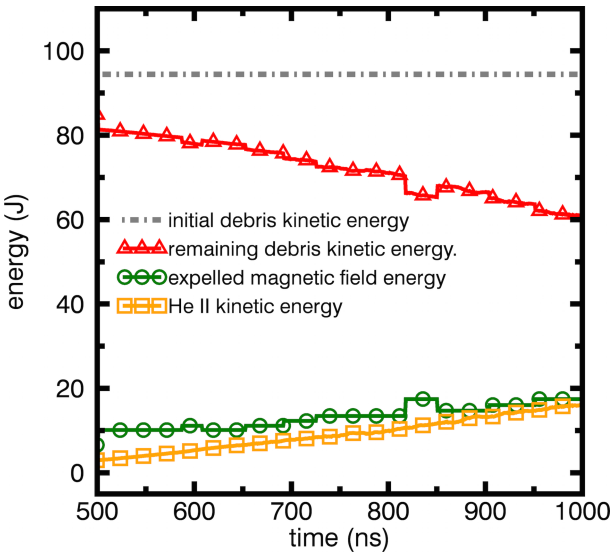

Figure 3.20: Energy balance corresponding the parameters of "Run 1 (3D)" in Table 3.2. The plot compares the temporal evolution of the magnetic energy $E_B(t)$ (green circles, Eq. 3.45), the extra He II ion kinetic energy $E_a(t)$ (orange squares, Eq. 3.46), and the remaining debris kinetic energy $E_d(t)$ (red triangles, Eq. 3.44). The initial debris ion kinetic energy E_K is also shown for comparison (dashed gray line). The step-like behavior of $E_B(t)$ results from the limited (1 cm) spatial resolution of the magnetic field measurements.

to the He II ions and the expulsion of the magnetic field, consistent with the theoretical considerations of Chapter 1 corresponding to the marginally super-Alfvénic regime of the experiment ($M_A \approx 2$ based on the speed of the peak magnetic compression).

3.5 Summary

This chapter has investigated whether the observed He II ion Doppler shifts of Chapter 2 are quantitatively, as well as qualitatively, consistent with an initial impulse due to the laminar electric field (Eq. 1.9). Due to the spatially and temporally integrated nature of the spectroscopic measurements, this investigation has demanded the development of a computational approach capable of simulating the trajectories and velocities of a distribution of ambient He II ions in response to the explosive debris plasma. Two-dimensional hybrid simulation

codes fail to take into account the three-dimensional expansion of the debris plasma in the actual experiment, while the recently developed three-dimensional hybrid code demands supercomputer processing power, which motivates an alternative, simplified approach. In the present analysis, radiation-hydrodynamic simulations of the laser-target interaction in HELIOS, wavelength-filtered imaging, limited measurements of the magnetic field and ambient density profiles, and a number of simplifying assumptions lead to spatiotemporal models of the electron density, the ion current density, the magnetic field, and the electron pressure based on a ballistic, drifting Maxwellian, teardrop-shaped debris plasma expansion. The derived models allow for a direct calculation of the electric field via Eq. 1.9 and an extrapolation of the measured magnetic field profile throughout the blow-off plane, thus permitting a simulation of the ambient He II ion response via the Lorentz force (Eq. 3.1). Four different parameter sets are utilized in the simulations, with one set corresponding to the actual experimental conditions and the three other sets corresponding to intentionally unrealistic variations, in order to examine the self-consistency of the approach. The modeled results yield the following important conclusions:

- In the central region of the ambient plasma column for $t \leq 1000$ ns, the experimentally realistic parameter set of "Run 1 (3D)" in Table 3.2 predicts that both the magnetic pressure gradient term and cross-field ion current term contribute significantly to the total laminar electric field, while the electron pressure gradient term is negligible. This is consistent with the marginally super-Alfvénic ($M_A \approx 2$), low electron beta ($\beta_e \ll 1$) regime of the experiment. The vector sum of the two contributing terms produces an asymmetric structure in the total electric field characterized by small $+y$ components in the upper half of the blow-off plane ($y > 0$ cm) and large $-y$ components in the lower half of the blow-off plane ($y < 0$ cm). Typical electric field magnitudes in the hundreds of V/cm are achieved.

- The He II ion test particle response corresponding to the experimentally realistic parameter set of "Run 1 (3D)" reflects the asymmetric electric field structure. By $t = 1000$ ns, test particles in the lower half of the blow-off plane ($y < 0$ cm) acquire

large $-y$ velocity components, while test particles in the upper half of the blow-off plane ($y > 0$ cm) develop small or negligible $+y$ velocity components. Moreover, the fastest He II ion test particles, which reach speeds upwards of ≈ 400 km/s, quickly escape the intensification region containing the energetic electrons and become optically invisible. The expectation is therefore that the observed Doppler-broadened spectra fail to capture the fastest He II ions and only include the intensified population, which achieves peak speeds of only ≈ 200 km/s.

- Synthetic temporally and spatially integrated spectra of the He II 468.6 nm line are constructed by sampling the simulated velocity distribution of the intensified, emitting subset of test particles within the optical collection region. The simulated spectrum corresponding to the realistic parameter set of "Run 1 (3D)" excellently reproduces the initial measured profile (time-integrated from $t = 500$ ns to $t = 1000$ ns and line-integrated along y at $x = 30$ cm), confirming that the observed Doppler shift quantitatively, as well as qualitatively, corresponds to initial He II ion acceleration via the laminar electric field of Eq. 1.9. The predominant blue shift and small red shift in the measured spectrum ultimately arise due to the asymmetric electric field structure produced by the vector sum of the magnetic pressure gradient term and the cross-field ion current term. Analogous synthetic spectra corresponding to the other three unrealistic parameter sets reveal significantly worse agreement to the data, indicating self-consistency between the HELIOS computations, the derived plasma parameter models, and the measured He II 468.6 nm spectrum.

- The consistency of the computed electric field is examined by comparing it to the measured magnetic field via the Maxwell-Faraday equation. The electric field corresponding to the experimentally realistic parameter set of "Run 1 (3D)" reasonably satisfies the Maxwell-Faraday equation, apart from a large initial disparity corresponding to the failure of the ballistic debris expansion model to take debris ion gyration into account. The other three unrealistic parameter sets reveal considerably more severe deviations from the Maxwell-Faraday equality, indicating self-consistency between

the HELIOS computations, the derived plasma parameter models, and the measured magnetic field profile.

- The validity of the ballistic debris expansion model is assessed via energy conservation for the experimentally realistic parameter set of "Run 1 (3D)." An estimate of the energies coupled into magnetic field expulsion (from the measured magnetic field profile) and into acceleration of the ambient He II ions (from the test particle simulations) reveals that the debris loses a non-negligible amount of its initial kinetic energy by $t = 1000$ ns. Consequently, the expectation is that the calculated test particle velocities between $t = 500$ ns and $t = 1000$ ns (the time interval used to construct the synthetic spectra) are valid only to within $\approx 20\%$. The analysis also reveals that a comparable amount of energy couples to the He II ions and to the expulsion of the magnetic field, consistent with the marginally super-Alfvénic regime ($M_A \approx 2$) of the experiment.

CHAPTER 4

Conclusion

The collision-less transfer of momentum and energy between explosive debris plasma and magnetized ambient plasma characterizes a wide variety of astrophysical and space environments. In an effort to better understand the detailed physics of collision-less coupling mechanisms, compliment *in situ* measurements, and provide validation of previous computational and theoretical work, the present research has utilized a unique experimental platform at the University of California, Los Angeles (UCLA) to study the interaction of explosive debris plasma with magnetized ambient plasma in a reproducible laboratory setting. Specifically, by jointly employing the LAPD and Phoenix facilities, the super-Alfvénic, quasi-perpendicular expansion of laser-produced carbon (C) and hydrogen (H) debris plasma through preformed, magnetized helium (He) ambient plasma has been monitored via a variety of sophisticated diagnostics, including emission spectroscopy, wavelength-filtered imaging, a magnetic flux probe, and a Langmuir probe. The subsequent data analysis has utilized various computational tools, including radiation-hydrodynamic modeling, collisional-radiative modeling, synthetic wavelength spectrum generation, and custom simulations, in order to compare the experimental data to the theoretical framework of collision-less coupling. The key conclusions of this work are as follows:

- Spectroscopic measurements of the He II 468.6 nm line collected perpendicular to both the blow-off axis and the magnetic field reveal significant, asymmetric Doppler broadening in response to the explosive debris plasma. A closer analysis indicates an initial acceleration of He II ions in the direction transverse to the debris plasma expansion and a subsequent gyration in the magnetic field. He II ion velocity components of up to

≈ 160 km/s are measured, nearly two orders of magnitude faster than the root-mean-square speed of ≈ 3 km/s in the unperturbed ambient plasma. The inferred trajectory qualitatively agrees with the cross-field ion current term of the laminar electric field (Eq. 1.9), which is theoretically expected to be the dominant debris-ambient coupling mechanism in the super-Alfvénic ($M_A > 1$), low electron beta ($\beta_e \ll 1$), collision-less ($\lambda_{da} \gg D$) regime that characterizes the experiment.

- A custom computational approach is developed in order to assess whether the observed Doppler broadening of the He II 468.6 nm line quantitatively agrees with laminar collision-less coupling. Radiation-hydrodynamic simulations of the laser-target interaction in HELIOS, wavelength-filtered imaging, limited measurements of the magnetic field and ambient density profiles, and a number of simplifying assumptions lead to spatiotemporal models of the electron density, the ion current density, the magnetic field, and the electron pressure based on a ballistic, drifting Maxwellian, teardrop-shaped debris plasma expansion. The derived models allow for a direct calculation of the electric field via Eq. 1.9 and an extrapolation of the measured magnetic field profile throughout the blow-off plane, thus permitting a simulation of the ambient He II ion response via the Lorentz force (Eq. 3.1). Four different parameter sets are utilized in the simulations, with one set corresponding to the actual experimental conditions and the three other sets corresponding to intentionally unrealistic variations, in order to examine the self-consistency of the approach.

- In the central region of the ambient plasma column for $t \leq 1000$ ns, the experimentally realistic parameter set predicts that both the radial-like magnetic pressure gradient term and the azimuthal cross-field ion current term contribute significantly to the total laminar electric field, while the electron pressure gradient term is negligible. This is consistent with the marginally super-Alfvénic ($M_A \approx 2$), low electron beta ($\beta_e \ll 1$) regime of the experiment. The vector sum of the two contributing terms produces an asymmetric structure in the total electric field characterized by small $+y$ components in the upper half of the blow-off plane ($y > 0$ cm) and large $-y$ components in the

lower half of the blow-off plane ($y < 0$ cm). Typical electric field magnitudes in the hundreds of V/cm are achieved. The modeled electric field is also shown to be reasonably consistent with the measured magnetic field through the Maxwell-Faraday equation, apart from a large initial disparity corresponding to the failure of the ballistic debris expansion model to take debris ion gyration into account.

- The He II ion test particle response corresponding to the experimentally realistic parameter set reflects the asymmetric electric field structure. By $t = 1000$ ns, test particles in the lower half of the blow-off plane ($y < 0$ cm) acquire large $-y$ velocity components, while test particles in the upper half of the blow-off plane ($y > 0$ cm) develop small or negligible $+y$ velocity components. Moreover, the fastest He II ion test particles, which reach speeds upwards of ≈ 400 km/s, quickly escape the intensification region containing the energetic electrons and become optically invisible. The expectation is therefore that the observed Doppler-broadened spectra fail to capture the fastest He II ions and only include the intensified population, which achieves peak speeds of only ≈ 200 km/s.

- Synthetic temporally and spatially integrated spectra of the He II 468.6 nm line are constructed by sampling the simulated velocity distribution of the intensified, emitting subset of test particles within the optical collection region. For the experimentally realistic parameter set, the simulated spectrum excellently reproduces the initial measured profile (time-integrated from $t = 500$ ns to $t = 1000$ ns and line-integrated along y at $x = 30$ cm), confirming that the observed Doppler shift quantitatively, as well as qualitatively, corresponds to initial He II ion acceleration via the laminar electric field of Eq. 1.9. The predominant blue shift and small red shift in the measured spectrum ultimately arise due to the asymmetric electric field structure produced by the vector sum of the magnetic pressure gradient term and the cross-field ion current term.

- Analogous synthetic spectra corresponding to the unrealistic parameter sets reveal significantly worse agreement to the measured spectrum. Similarly, the calculated

electric fields corresponding to the unrealistic parameter sets deviate more severely from the Maxwell-Faraday equation. This demonstrates self-consistency between the HELIOS-computed debris plasma parameters, the derived plasma parameter models, the measured magnetic field profile, and the measured He II 468.6 nm spectrum.

- Wavelength-filtered imaging observes a considerable and long-lasting (> 10 μs) intensification of the He II 468.6 nm emission in response to the explosive debris plasma, indirectly indicating the continual generation of electrons with kinetic energies > 51 eV. Comparison to magnetic flux probe measurements suggests that the energetic electrons first develop within the magnetic compression as it sweeps through the ambient plasma and remain confined primarily within the diamagnetic cavity until its collapse. Biased Langmuir probe measurements at positions field-aligned to the intensified He II region confirm the long-lasting duration of fast electrons that stream along the magnetic field lines with directed kinetic energies > 50 eV.

To distill the above conclusions even further, the most important result of this research is that the observed initial He II ion response to the explosive debris plasma agrees both qualitatively and quantitatively with the laminar electric field (Eq. 1.9). In other words, the data provides clear evidence of laminar collision-less debris-ambient coupling. This is theoretically consistent with the super-Alfvénic ($M_A > 1$), low electron beta ($\beta_e \ll 1$), collision-less ($\lambda_{da} \gg D$) regime of the experiment and validates the "hybrid" approach employed by previous theoretical and computational studies, which utilize a fluid electron model and use equations analogous to Eq. 1.9 to compute the electric field. The second key result of this work is that the debris-ambient interaction results in the generation of energetic electrons. However, this observation falls outside the scope of laminar coupling theory. At present, the energetic electron generation mechanism is not understood, though the possibility of certain instabilities driven by the slower, sub-Alfvénic debris ion charge states offers a promising starting point (see Appendix A or [9]).

A number of future pursuits can significantly expand upon the results of this investigation. Because the custom computational methods developed throughout this analysis assume a ballistic debris plasma expansion, the accuracy of the modeled results necessarily deteriorates with time as the debris ions undergo deceleration and gyration. Thus, while this approach suffices for a reasonable prediction of the initial ambient ion response, an assessment of late-time data will require supercomputers to run fully three-dimensional hybrid code simulations. Furthermore, the teardrop debris expansion geometry utilized in this study relies on the assumption of symmetry, since wavelength-filtered images of the debris plasma are only taken in the plane perpendicular to the magnetic field. A more accurate expansion model will require additional imaging in the plane parallel to the magnetic field. Alternatively, the planar laser-induced fluorescence diagnostic (see Appendix B or [8]) can potentially provide a three-dimensional map of the debris ion spatial distribution. Future experiments with the new high-repetition rate Peening laser will also extend this work tremendously by allowing for detailed volumetric measurements that are unfeasible with Raptor due to its lengthy cool-down time. In particular, volumetric scans with magnetic flux probes and emissive probes can yield direct spatiotemporal measurements of the magnetic and electric fields. This will ultimately allow for accurate test particle simulations of the ambient ion response that, in contrast to the present analysis, will not rely on specific debris expansion models and parameters. While Peening cannot access the high energy regime of Raptor, such experiments will nevertheless yield important results on the physics of debris-ambient coupling. A detailed investigation of the mechanisms responsible for generating the observed energetic electrons will also substantially compliment this research. Such studies can make headway by utilizing biased Langmuir probes to perform spatiotemporal scans of the energetic electron distribution and emissive probes to search for characteristic frequencies of certain candidate mechanisms like the modified two-stream instability. Eventually, the development of ion-based diagnostics such as Faraday cups and Thomson parabolas will allow for a direct measurement of the velocity distributions and abundances of the debris and ambient ions. These future pursuits will significantly build upon the results presented in this work, leading

to an improved understanding of the physics of collision-less momentum and energy transfer between explosive debris plasma and magnetized ambient plasma.

APPENDIX A

Preliminary Evidence of Instabilities

A.1 Overview

The experimental results of Chapter 2 and the computational analysis of Chapter 3 conclusively demonstrate that the observed initial response of the He II ambient ions to the explosive debris plasma agrees qualitatively and quantitatively with the laminar electric field (Eq. 1.9). This is consistent with the theoretical considerations of Chapter 1, which indicate that laminar collision-less coupling mechanisms predominate in the super-Alfvénic ($M_A > 1$), low electron beta ($\beta_e \ll 1$) regime. It is important to recall, however, that the explosive debris plasma consists of a mixture of ion charge states with average expansion speeds segmented by the charge-to-mass ratios [7]. As a consequence, while the fastest debris charge states exceed the Alfvén speed of the ambient plasma, the slower charge states may fail to do so, and the physics relevant to the sub-Alfvénic ($M_A < 1$) regime can also become important. In particular, as detailed in Chapter 1, turbulent collision-less coupling mechanisms associated with the magnetized ion-ion two-stream instability [47] and the modified two-stream instability [40] become effective provided that

$$M_A \leq (1 + \beta_e)^{\frac{1}{2}} . \tag{1.4}$$

Since $\beta_e \ll 1$, Eq. 1.4 implies that sub-Alfvénic components of the explosive debris plasma can potentially excite these instabilities. This appendix presents preliminary experimental evidence that such instabilities develop in the context of debris-ambient interaction.

Emission spectroscopy provides a species-selective, non-interfering diagnostic for assessing the strong, oscillatory electric fields associated with instabilities via the Stark effect [26].

Conventionally, Stark broadening of spectral lines is associated with dense plasmas in which emitting atoms or ions experience time-varying "micro-fields" due to ions and electrons located within approximately a Debye radius from the emitters. In this type of "pressure" Stark broadening, the width and shape of spectral lines can be used to extract various plasma parameters, including electron temperature and density [58]. However, Stark broadening can also be attributed to long-range, collective electric fields corresponding to plasma waves and turbulence [27]. This type of "wave field" Stark broadening can significantly exceed pressure broadening in lower density, non-equilibrium plasmas. In addition, the electric field oscillations corresponding to plasma waves and turbulence can generate detectable sideband spectral lines, or "satellites" [3]. Provided that all other significant broadening mechanisms are taken into account, wave field Stark broadening models can yield the magnitude, frequency, and direction of the electric field from the spectral line shape and separation between the satellites. This diagnostic has thus proven to be a valuable tool in the investigation of plasma turbulence in a number of studies [1, 23, 42].

In this appendix, an experiment analogous to that of Chapter 2 utilizes emission spectroscopy and wave field Stark broadening theory to study the electric fields associated with the quasi-perpendicular expansion of laser-produced carbon (C) debris plasma through a preformed, magnetized helium (He) ambient plasma. Spectral profiles of the He II 468.6 nm line measured at the maximum extent of the diamagnetic cavity are observed to intensify, broaden, and develop equally spaced modulations in response to the explosive C debris plasma, indicative of an energetic electron population and strong oscillatory electric fields. The profiles are analyzed via time-dependent Stark effect models corresponding to single-mode and multi-mode monochromatic (single frequency) electric fields for hydrogen (H)-like ions, yielding temporally resolved (1 μs) electric field magnitudes ($\sim 10^2$ kV/cm) and frequencies ($\sim 10^{11}$ rad/s). The measured magnitudes and frequencies exceed those of the laminar electric field (see Chapter 3) and the turbulent collision-less coupling mechanisms described previously by orders of magnitude, indicating a secondary effect. The proximity of the measured frequencies to the expected electron plasma frequency suggests

the development of the electrostatic electron beam-plasma instability, and a simple saturation model demonstrates that the measured electric field magnitudes are reasonable provided that a sufficiently fast electron population ($\sim 10^9$ cm/s) is generated during debris-ambient interaction. This is consistent with independent evidence of energetic electrons derived from biased Langmuir probe measurements and wavelength-filtered imaging of He II ion intensification in Chapter 2. Potential sources of the fast electrons are briefly addressed. In particular, the modified two-stream instability (one of the candidate turbulent collision-less coupling mechanisms) offers a promising explanation.

It is important to point out that the results described in this appendix were obtained and analyzed prior to the experiment of Chapter 2. At that time, it was believed that debris-ambient coupling was insufficient to significantly accelerate He II ions and cause considerable Doppler shifts, so the observed broadening in the He II 468.6 nm line was attributed primarily to the wave-field Stark effect. The more recent results of Chapter 2 and the detailed analysis of Chapter 3 found that significant He II ion acceleration does, in fact, occur. Therefore, in any future extensions of the investigation described in this appendix, the possibility that the observed broadening is simply the Doppler effect must be considered. Nevertheless, there are two reasons to believe that wave-field Stark broadening is actually occurring. The first reason is the detection of equally-spaced modulations at a frequency near the expected electron plasma frequency. Unless the measured spectrum contains significant noise at a highly coincidental frequency, this effect is very difficult to explain via Doppler broadening. The second reason is that the spectroscopic measurements described in this appendix are collected along the magnetic field (in contrast to the perpendicular measurements of Chapter 2) and focused to image the blow-off plane. As detailed in Chapter 3, He II ions in the blow-off plane accelerate perpendicular to the magnetic field in response to the debris and therefore do not cause Doppler broadening in spectra measured along the field. However, because the spectra also contain defocused contributions along the collection axis, they may include Doppler broadening due to the acceleration of He II ions offset from the blow-off plane. A fully three-dimensional hybrid code simulation is necessary to investigate this. In the analysis

of this appendix, it is assumed that no significant He II ion acceleration occurs along the magnetic field.

Section A.2 begins by outlining the experimental configuration. Section A.3 describes the extraction of electric field magnitudes and frequencies from spectral profiles via time-dependent Stark effect models. Section A.4 demonstrates the consistency of the measurements with the electron beam-plasma instability and briefly discusses the potential sources of the necessary fast electrons. Finally, Section A.5 summarizes the results.

A.2 The Experiment

The present experiment utilizes the platform detailed in Chapter 2, combining the Large Plasma Device (LAPD) [24] and the Raptor high-energy laser [43]. A similar co-ordinate system is employed, differing only in that the axial magnetic field now defines the $+z$ direction rather than the $-z$ direction. A schematic of the configuration is shown in Fig. A.1. The LAPD generates He ambient plasma via two simultaneous cathode-anode discharges at opposite ends of the machine. The main discharge from a large barium oxide (BaO) coated nickel (Ni) cathode produces a 60 cm diameter plasma column with an electron density of $\approx 2 \times 10^{12}$ cm^{-3}, while a second discharge from a smaller, higher-emissivity lanthanum hexa-boride (LaB_6) cathode increases the electron density of the central 20 cm diameter to $\approx 4 \times 10^{12}$ cm^{-3}. The center of the plasma column is approximately aligned to $(x, y) =$ (30 cm, 0 cm), corresponding to the central axis of the machine. A uniform magnetic field of 300 G in the $+z$ direction magnetizes the plasma. At the machine center, the electron temperature is ≈ 5.5 eV and the ion temperature is $\lesssim 1$ eV. A long, rectangular graphite target is submerged into the LAPD and the target face normal is oriented in the $+x$ direction. The Raptor laser, operating at 100 ± 5 J per pulse, is focused onto the surface of the target at $(x, y, z) =$ (0.6 cm, 0 cm, 0 cm) through a 1.8 m focal length lens to a spot size of ≈ 2 mm^2, yielding average surface intensities of 200 ± 10 GW/cm^2. Because laser-ablated plasma is primarily directed along the target surface normal independent of the laser angle

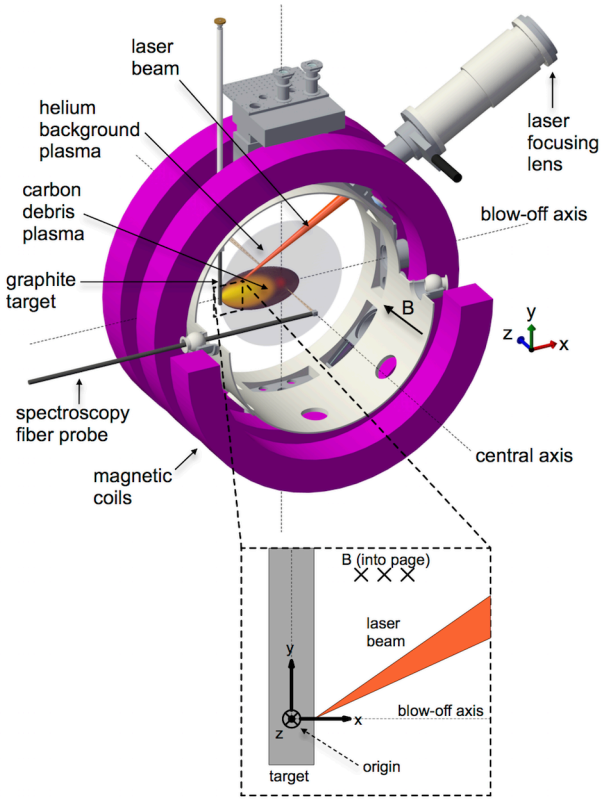

Figure A.1: Schematic of the experimental setup, showing the utilized section of the LAPD and the quasi-perpendicular expansion of laser-produced C debris plasma through the pre-formed, magnetized He ambient plasma. A spectroscopic fiber probe monitors the debris-ambient interaction with the collection axis oriented parallel to the magnetic field. The inset defines the co-ordinate system.

of incidence, the present target orientation ensures that the C debris expands primarily in the $+x$ direction along the blow-off axis defined by $(y, z) = (0\text{ cm}, 0\text{ cm})$, across the magnetic field, and through the maximal volume of ambient plasma. The target is moved up or down between every laser shot to provide a fresh, flat surface for ablation. Table A.1 summarizes the experimental parameters.

A custom-built spectroscopic fiber probe is placed at coordinates $(x, y, z) = (30\text{ cm}, 0\text{ cm}, -30\text{ cm})$ and oriented to collect line-integrated light emission along the $+z$ direction, parallel to the background magnetic field and perpendicular to the primary blow-off direction. (By

laser energy	100 ± 5 J
laser intensity	200 ± 10 GW/cm^2
background magnetic field	300 G
debris plasma species	C
ambient plasma species	He
ambient plasma diameter	≈ 20 cm (LaB_6), ≈ 60 cm (BaO)
ambient electron density	$\approx 4 \times 10^{12}$ cm^{-3}
ambient electron temperature	≈ 5.5 eV

Table A.1: Parameters of Stark broadening experiment.

contrast, the spectroscopic configuration of Chapter 2 collects emission perpendicular to both the background magnetic field and the primary blow-off direction.) A 75 mm focal length lens at the probe's collection end projects an image from the blow-off plane ($z = 0$ cm) onto a vertically oriented linear array of 20 200 μm fused silica optical fibers. In this configuration, the imaged field of view is centered at $x = 30$ cm on the blow-off axis, spanning ≈ 0.1 cm along x and ≈ 1.5 cm along y. However, the collected signal also contains defocused contributions along the entire line of sight. The fibers are directly coupled into a 0.75 m SPEX spectrometer containing a 3600 g/mm UV holographic grating. The spectrum is centered on the He II 468.6 nm line and projected onto a Princeton Instruments (PI) MAX 2 intensified charge-coupled device (ICCD) camera, yielding a spectral resolution of ≈ 0.02 nm. Light emission collected during laser shots is time-integrated for 1 μs at various delays after the laser pulse. Additional diagnostics, including a differentially wound magnetic flux probe [22] and a Thomson scattering system [50], are employed at various locations along the blow-off axis, though they are not shown in Fig. A.1.

A.3 Spectroscopic Measurements of Electric Fields

This section describes the extraction of time-resolved electric field magnitudes and frequencies from measured spectral profiles of the He II 468.6 nm line via wave field Stark effect theory. First, context is established by reviewing the basic features of laser-produced debris plasma expansion into magnetized ambient plasma and identifying the spatial and temporal extent of the spectroscopic measurements with respect to measured magnetic field profile. Second, the effect of explosive C debris plasma on the emission profile of the He II 468.6 nm line is assessed, yielding evidence of the development of oscillatory electric fields. Third, the theoretical spectral profiles of H-like ions subjected to single-mode and multi-mode monochromatic electric fields are described in accordance with the wave field Stark effect, and the inclusion of other spectral line broadening mechanisms is discussed. Finally, the theoretical spectral models are applied to the measured profiles, yielding time-resolved electric field magnitudes and frequencies from the best fits.

A.3.1 Spatial and Temporal Extent of Spectroscopic Measurements

In order to put the spectroscopic measurements into context, it is useful to review the basic features of the quasi-perpendicular expansion of laser-produced debris plasma through preformed, magnetized ambient plasma [64]. In the present experiment, an energetic laser pulse at time $t = 0$ μs ablates the surface of a graphite target, producing explosive C debris plasma expanding radially, quasi-perpendicular to the background magnetic field ($B_0 = 300$ G). At times much earlier than an ion gyro-period, the effectively free-streaming C debris ions outrun the magnetically confined debris electrons, resulting in a radial electric field. This causes an azimuthal $\vec{E} \times \vec{B}$ drift of the electrons, which, in conjunction with $\vec{\nabla} p_e \times \vec{B}$ electron pressure gradient flows, generates a diamagnetic current that expels the background magnetic field within the current layer (the diamagnetic cavity). More complicated effects [64] set up an additional, oppositely directed current layer just ahead of the cavity, which increases the magnetic field magnitude over a small region (the magnetic compression). As

the C debris plasma continues to expand, it propagates the magnetic compression forward and the diamagnetic cavity increases in size. The C debris ions also transfer momentum and energy to the He ambient ions through collision-less, collective, electromagnetic processes, primarily in the vicinity of the magnetic compression and diamagnetic cavity edge, though the efficiency of the coupling depends on a number of parameters [49, 14]. Doppler shift measurements of the dominant C V debris charge state indicate an initial expansion speed of $(1.60 \pm 0.20) \times 10^7$ cm/s [48]. At the background magnetic field, this corresponds to a marginally super-Alfvénic ($M_A \approx 1.1$) expansion on average, though a significant fraction of the debris is sub-Alfvénic ($M_A < 1$) due to the large spread in the velocity distribution. The C debris ions decelerate due to interactions with both the magnetic field and He ambient plasma, and the diamagnetic cavity growth eventually stops. Late in time, the magnetic field returns to its background value via diffusion.

Fig. A.2 demonstrates the temporal and spatial extent of the spectroscopic measurements with respect to profiles of the magnetic field's z-component (B_z), measured via the differentially wound magnetic flux probe during C debris expansion through the He ambient plasma. The temporal profile shows the evolution of B_z at $x = 30$ cm along the blow-off axis, which is the imaged spatial location of the spectroscopic measurements. The peak compression occurs at $t \approx 1.6$ μs and the field is fully expelled by $t \approx 2.8$ μs. By $t \approx 4.6$ μs, magnetic diffusion has restored the field to its background value. Continued growth of the field above the background value at later times is an artifact of the numerical integration used in the analysis. The shaded region from $t = 2$ μs to 8 μs represents the time range during which time-resolved (1 μs) spectroscopic measurements of the electric field are obtained. The spatial profile shows the structure of B_z along the blow-off axis at $t = 3$ μs, the approximate time at which the diamagnetic cavity reaches its maximum extent of $x \approx 30$ cm. The peak magnetic compression can be seen ahead of the cavity at $x \approx 45$ cm. The imaged spatial location of the spectroscopic measurements, highlighted at $x = 30$ cm, is thus at the approximate maximum extent of the diamagnetic cavity edge. It is important to recall that defocused emission along the entire line of sight also contributes to the spectroscopic signal.

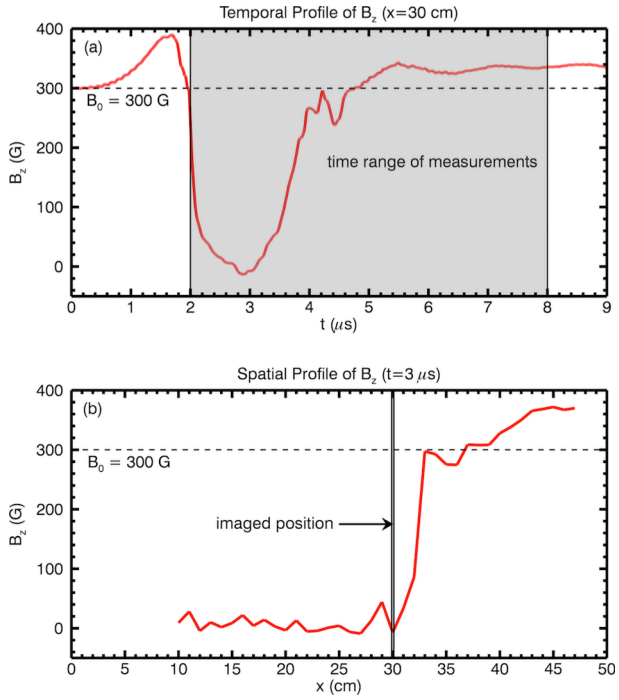

Figure A.2: Profiles of the magnetic field's z-component (B_z) during debris-ambient interaction. The temporal profile (a) shows the evolution of B_z (in G) at $x = 30$ cm along the blow-off axis, corresponding to the imaged location of the spectroscopic measurements. The spatial profile (b) shows the structure of B_z (in G) along the blow-off axis at $t = 3$ μs, when the diamagnetic cavity reaches its approximate maximum size. The highlighted regions correspond to the temporal range ($t = 2$ μs to 8 μs) and position ($x = 30$ cm) of the spectroscopic measurements.

A.3.2 Evidence of Oscillatory Electric Fields

The explosive expansion of laser-produced C debris plasma through magnetized He ambient plasma significantly affects the emission profile of the He II 468.6 nm line. Specifically, the line intensifies, broadens, and develops equally spaced modulations immediately after the magnetic compression passes through the collection field of view at $t \approx 1.6$ μs, and these effects are detectable until $t \approx 8$ μs, long after the collapse of the diamagnetic cavity. Fig. A.3 shows the wavelength profiles obtained with and without C debris plasma at $x = 30$ cm along the blow-off axis, time-integrated from $t = 3$ μs to 4 μs. Comparison of the non-normalized

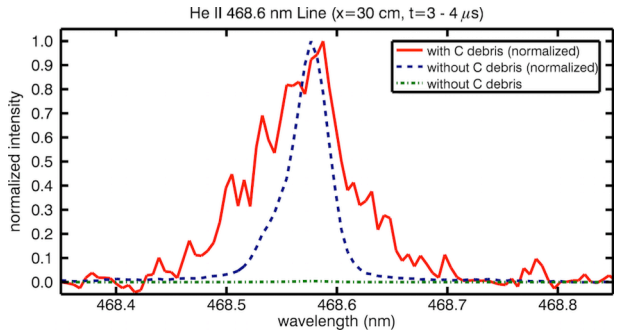

Figure A.3: Comparison of the observed He II 468.6 nm line profiles with and without explosive C debris plasma. The profile with C debris (solid line) intensifies (factor of ≈ 500 in wavelength-integrated intensity) and broadens (factor of ≈ 2 in FWHM) relative to the non-normalized (dash-dotted line) and normalized (dashed line) profiles without C debris, respectively, and becomes modulated by subsidiary peaks.

profiles reveals that the wavelength-integrated intensity increases by a factor of ≈ 500, while comparison of the normalized profiles demonstrates that the FWHM increases by a factor of ≈ 2. Additionally, in the presence of C debris, the broadened profile appears to become modulated by subsidiary peaks.

While the line intensification indicates an energetic electron population that excites ground state He II ions via collisions and causes additional fluorescence, the line broadening and formation of equally spaced modulations can be understood from the wave field Stark effect. A well-known characteristic of H-like ions subjected to an oscillating, monochromatic (single frequency) electric field is the formation of a series of sideband spectral lines, or "satellites," symmetrically located on either side of the original line center and spaced apart at the electric field frequency [46] (discussed in detail in the following subsection). If the frequency is high enough for the satellite separation to exceed the resolution limit of the spectroscopy apparatus, the individual satellites are, in principle, observable. However, if other effects (e.g., Doppler broadening) are substantial enough to overlap the individual satellites, the resulting profile can resemble a single broadened, modulated peak. This is consistent with the observed He II 468.6 nm line profile of Fig. A.3, suggesting that the interaction

of explosive C debris plasma with magnetized He ambient plasma generates monochromatic electric fields. Qualitatively similar broadened, modulated profiles of the He II 468.6 nm line have been observed in previous studies [1, 23] investigating plasma turbulence.

It is necessary to verify that the modulations are equally spaced and not an artifact of noise. Fig. A.4 demonstrates the use of Fourier transforms and low-pass filtering to identify a specific wavenumber corresponding to the modulations. It shows the broadened, modulated He II 468.6 nm line profile of Fig. A.3 low-pass filtered above and below a distinct peak in the Fourier transform with a wavenumber of 35 nm^{-1}. The modulations disappear when the low-pass filter cuts off the peak in wavenumber space, confirming that the embedded pattern is equally spaced with a separation of $\Delta\lambda_E = 1/35\ \text{nm}^{-1} \approx 0.029$ nm between consecutive modulations. At the transition wavelength $\lambda_c = 468.6$ nm, this separation corresponds to an electric field frequency of $\omega_E \approx 2\pi c\Delta\lambda_E/\lambda_c^2 \approx 2.5 \times 10^{11}$ rad/s. Fourier transforms of dark frames do not exhibit a distinct peak at any wavenumber, eliminating the possibility of a detector artifact. In addition, the modulations are not present in He II 468.6 nm line profiles measured without C debris plasma. The modulations are thus concluded to be a result of monochromatic electric fields arising during debris-ambient interaction.

A.3.3 Theoretical Spectra of H-like Ions in Monochromatic Electric Fields

From the wave field Stark effect on H-like ions, analytic expressions for the spectral profiles arising in various time-dependent electric fields can be obtained as a function of frequency, magnitude, and direction. Best fits of the theoretical spectra to the data can thus yield measurements of one or more of these parameters. Though the observed modulations suggest the development of monochromatic electric fields during debris-ambient interaction, their exact functional form is not known *a priori*. In an effort to obtain the best possible fit, this study considers both single-mode monochromatic fields, represented by a single sinusoid, and multi-mode monochromatic fields, represented by a super-position of sinusoids of different amplitudes and phases.

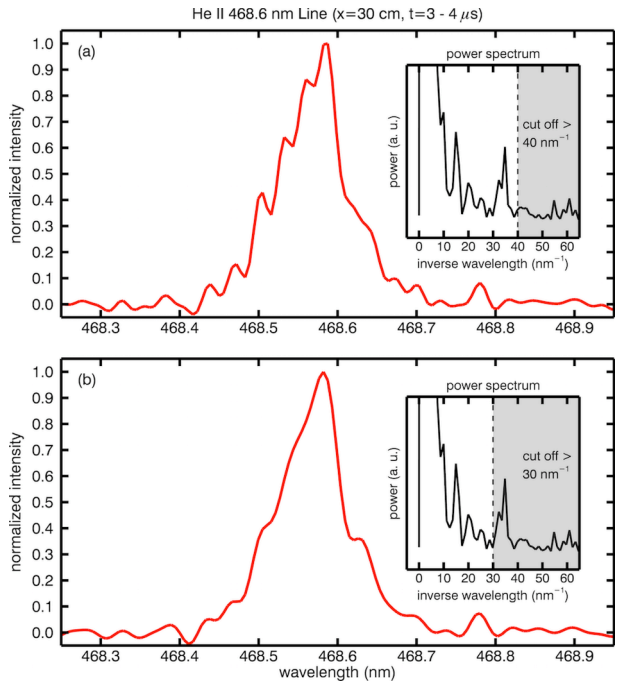

Figure A.4: Demonstration that the modulations embedded in the He II 468.6 nm line profiles measured with explosive C debris plasma are equally spaced, indicative of monochromatic electric fields. In this profile, the modulations disappear when a low-pass filter moves from (a) just above to (b) just below a distinct peak in the Fourier transform (insets) at 35 nm^{-1}, corresponding to a wavelength spacing of $\Delta\lambda_E \approx 0.029$ nm and an electric field frequency of $\omega_E \approx 2.5 \times 10^{11}$ rad/s.

Single-mode model: The theoretical spectral profile of H-like ions under the influence of a one-dimensional, single-mode, monochromatic (frequency ω_E) electric field of the form

$$E(t) = E_0 \cos(\omega_E t) \tag{A.1}$$

was first derived by Blochinzew [6, 46]. Ignoring all other line broadening mechanisms, the intensity profile S_{SM} in wavelength space has the form

$$S_{SM}(\Delta\lambda) \approx C \times \sum_{p=-\infty}^{+\infty} \delta(\Delta\lambda - p\Delta\lambda_E) I_{SM}(p, \epsilon, X_k, f_k). \tag{A.2}$$

Here, C is an arbitrary normalization constant, and $\Delta\lambda$ is the independent variable indicating the wavelength interval from the center transition wavelength λ_c. The profile S_{SM} is thus

characterized by an infinite series of δ-function satellites symmetrically located about the transition center and separated by $\Delta\lambda_E$, which is directly proportional to the electric field frequency $\omega_E \approx 2\pi c\Delta\lambda_E/\lambda_c^2$. The relative satellite intensities are determined by the function I_{SM}, which has the form

$$I_{SM}(p, \epsilon, X_k, f_k) = C \times \left(f_0\delta_{p0} + 2\sum_{k=1}^{k_m} f_k J_p^2(\epsilon X_k) \right). \tag{A.3}$$

Here, p is the satellite order, δ_{p0} is the Kronecker delta, J_p is the Bessel function of the first kind of order p, and the X_k and f_k coefficients are tabulated [61] lateral Stark component shift parameters and relative intensities, respectively. The parameter ϵ is defined by

$$\epsilon = \frac{3ea_0E_0}{2Z\hbar\omega_E}, \tag{A.4}$$

where E_0 is the electric field amplitude, ω_E is the electric field frequency, Z is the nuclear charge number (2 for He), e is the electron charge, a_0 is the Bohr radius, and $\hbar$ is the reduced Planck's constant. To obtain the full theoretical profile, it is necessary to convolve Eq. A.2 with a line shape function F that takes into account all other significant line broadening effects (e.g., Doppler broadening). The convolution is particularly simple because of the δ-function, yielding

$$S_{SM+F}(\Delta\lambda) \approx C \times \sum_{p=-\infty}^{+\infty} F(\Delta\lambda - p\Delta\lambda_E) I_{SM}(p, \epsilon, X_k, f_k). \tag{A.5}$$

Thus, the full single-mode profile S_{SM+F} is characterized by an infinite series of broadened satellites symmetrically located about the transition center, separated by $\Delta\lambda_E$, and weighted by I_{SM}. The separation between the satellites only depends on ω_E, while the satellite intensity envelope I_{SM} depends on ω_E, E_0, and the electric field direction. The electric field directionality is implicitly included in the sum over k in Eq. A.3, which selectively includes σ- and π-polarized lateral Stark components depending on the direction of observation with respect to the direction of the electric field.

Multi-mode model: The theoretical spectral profile of H-like ions under the influence of

a one-dimensional, multi-mode, monochromatic (frequency ω_E) electric field of the form

$$E(t) = \sum_{j=1}^{\mathcal{N}} E_j \cos\left(\omega_E t + \varphi_j\right) \tag{A.6}$$

was first obtained by Lifshitz [37, 46] in the limit $\mathcal{N} \to \infty$. Ignoring all other line broadening mechanisms, the intensity profile S_{MM} in wavelength space has the form

$$S_{MM}(\Delta\lambda) \approx C \times \sum_{p=-\infty}^{+\infty} \delta(\Delta\lambda - p\Delta\lambda_E) I_{MM}(p, \tilde{\epsilon_k}, f_k). \tag{A.7}$$

Just as in the single-mode case, the profile S_{MM} is characterized by an infinite series of δ-function satellites symmetrically located about the transition center and separated by $\Delta\lambda_E$. The relative satellite intensities are determined by the function I_{MM}, which has the form

$$I_{MM}(p, \tilde{\epsilon_k}, f_k) = C \times \left(f_0 \delta_{p0} + 2 \sum_{k=1}^{k_m} f_k I_{|p|}(\tilde{\epsilon_k}) e^{-\tilde{\epsilon_k}} \right). \tag{A.8}$$

Here, $I_{|p|}$ is the modified Bessel function of the first kind of order $|p|$. The parameter $\tilde{\epsilon_k}$ is defined by

$$\tilde{\epsilon_k} = \frac{1}{2} X_k^2 \left(\frac{3 e a_0 E_{RMS}}{2 Z \hbar \omega_E} \right)^2, \tag{A.9}$$

where E_{RMS} is the root-mean-square electric field magnitude $E_{RMS} = (\sum_{j=1}^{\mathcal{N}} E_j^2)^{\frac{1}{2}}$. All of the other parameters have the same definitions as in the single-mode case. The full theoretical profile is obtained by convolving Eq. A.7 with a line shape function F that includes all of the other line broadening mechanisms, yielding

$$S_{MM+F}(\Delta\lambda) \approx C \times \sum_{p=-\infty}^{+\infty} F(\Delta\lambda - p\Delta\lambda_E) I_{MM}(p, \tilde{\epsilon_k}, f_k). \tag{A.10}$$

Thus, the full multi-mode profile S_{MM+F} is characterized by an infinite series of broadened satellites symmetrically located about the transition center, separated by $\Delta\lambda_E$, and weighted by I_{MM}. As in the single-mode case, the separation between the satellites only depends on ω_E, while the satellite intensity envelope I_{MM} depends on ω_E, E_{RMS}, and the electric field direction, which is embedded in the sum over k in Eq. A.8

In order to utilize the theoretical profiles corresponding to single-mode and multi-mode monochromatic electric fields (Eq. A.5 and Eq. A.10), it is necessary to determine the line

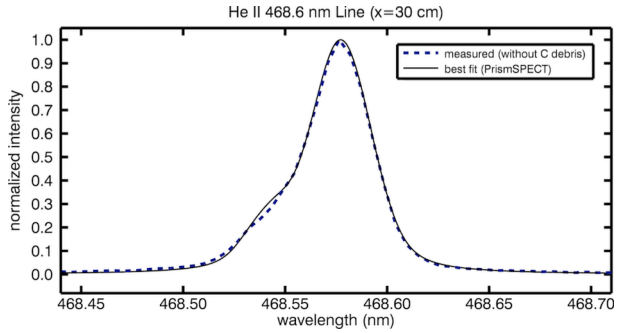

Figure A.5: Determination of the line shape function F that is employed in Eq. A.5 and Eq. A.10. A synthetic profile of the He II 468.6 nm line generated via PrismSPECT (solid line) is fit to a profile measured without C debris plasma (dashed line). The best-fit synthetic spectrum (at an ion temperature of ≈ 0.4 eV) includes Doppler broadening, instrumental broadening, pressure Stark broadening, and fine structure splitting, and defines the smooth, noise-free line shape function F.

shape function F. This is accomplished by fitting a synthetic profile of the He II 468.6 nm line generated via a steady-state, non-local thermal equilibrium (non-LTE) simulation in the collisional-radiative code PrismSPECT [38] to a profile measured without the presence of explosive C debris plasma, which does not contain the satellite effects from monochromatic electric fields and only includes contributions from other significant broadening mechanisms. Since only a rough estimate of the He II ion temperature exists, it is treated as a free parameter in the fit. The rest of the background plasma parameters used in the simulation follow from Section A.2. Fig. A.5 shows the best-fit synthetic spectrum (at an ion temperature of ≈ 0.4 eV) to a measured profile. Doppler broadening, instrumental broadening, pressure Stark broadening, and fine structure splitting are taken into account. The fit does not include Zeeman splitting, but this effect is undetectable at the experimental resolution for magnetic fields smaller than $\sim 10^4$ G. The best-fit synthetic profile defines the smooth, noise-free line shape function F.

A.3.4 Application of Theoretical Spectra to Data

Theoretical profiles corresponding to single-mode and multi-mode monochromatic electric fields (Eq. A.5 and Eq. A.10) are now fit to He II 468.6 nm line profiles measured with C debris plasma. In the fitting process, only the electric field magnitude is treated as a free parameter. The modulation separation $\Delta\lambda_E$ and the electric field frequency $\omega_E \approx 2\pi c\Delta\lambda_E/\lambda_c^2$ are locked to their determined values from the Fourier transforms of the measured wavelength profiles, as demonstrated in Fig. A.4. The direction of the electric field, unknown *a priori*, is fixed to either perpendicular or parallel to the optical collection axis through the sum over k in Eq. A.3 and Eq. A.8. In total, there are thus four types of fits: single-mode perpendicular, single-mode parallel, multi-mode perpendicular, and multi-mode parallel. To eliminate noise artifacts and improve the fit quality, the measured profiles are low-pass filtered just above the modulation wavenumber. Fig. A.6 demonstrates the construction of a single-mode perpendicular theoretical best fit to the broadened, modulated He II 468.6 nm line profile of Fig. A.3. First, a series of δ-function satellites spaced by $\Delta\lambda_E$ is constructed in accordance with Eq. A.2. Next, each δ-function satellite is replaced with the line shape function F of Fig. A.5. Finally, the broadened satellites are added together and the result is re-normalized, yielding the final theoretical profile of Eq. A.5. A Levenberg-Marquardt mean-squared error minimization algorithm varies the electric field amplitude E_0, which modifies the relative intensities of the broadened satellites through I_{SM} (Eq. A.3) until a best fit to the measured profile is achieved. The single-mode perpendicular model replicates the general shape of the profile quite well, yielding a best-fit amplitude of $E_0 = 26 \pm 6$ kV/cm. However, the model fails to reproduce the observed modulations, which are "washed out" due to the overlap of the individual broadened satellites. In order to better reproduce the observations, a more rigorous treatment of fine structure [66] and consideration of resonant non-adiabatic features [45] in the context of the time-dependent Stark effect may be necessary, which is outside the scope of this study.

The process demonstrated in Fig. A.6 is repeated for a time series of He II 468.6 nm line profiles with the four different types of theoretical fits (single-mode perpendicular, single-

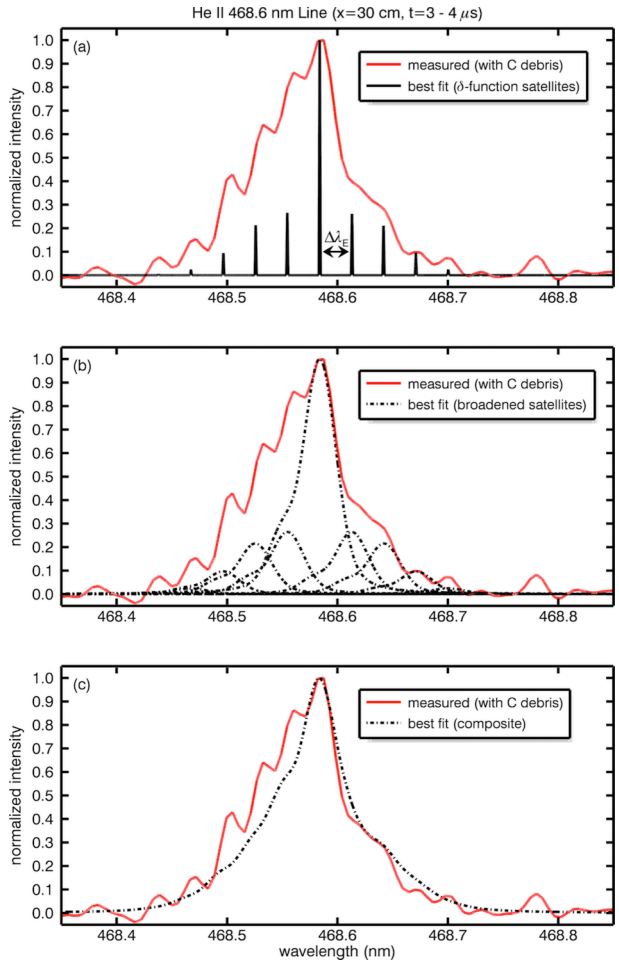

Figure A.6: Generation of a theoretical best fit (dash-dotted line) to a He II 468.6 nm wavelength profile measured with explosive C debris plasma (solid line), assuming a single-mode, perpendicular electric field. In (a), a series of δ-function satellites is spaced apart by $\Delta\lambda_E$ from the Fourier transform, in accordance with Eq. A.2. In (b), each δ-function satellite is replaced with the line shape function F. In (c), the final profile is generated by adding the broadened satellites and re-normalizing, in accordance with Eq. A.5. The best fit yields an electric field amplitude of $E_0 = 26 \pm 6$ kV/cm.

mode parallel, multi-mode perpendicular, and multi-mode parallel). The time series spans from $t = 2$ μs to 8 μs, the interval during which the intensification of the He II 468.6 nm line is sufficient to yield a strong signal over the 1 μs integration time. Fig. A.7 shows the root-mean-square electric field magnitudes, frequencies, and intensification factors (the factors by which the collected, wavelength-integrated signal intensifies relative to the background level in the presence of explosive C debris) plotted versus time. For the single-mode fits, the root-mean-square electric fields are obtained by multiplying the best-fit amplitudes E_0 by the standard factor of $\frac{\sqrt{2}}{2}$ for sinusoidal functions. From the results, it is clear that the different types of fits yield considerably different magnitudes. The single-mode perpendicular model yields the weakest fields (8 - 26 kV/cm), while the multi-mode parallel model yields the strongest fields (49 - 182 kV/cm). The measured frequencies are in the range 2.2 - 4.6×10^{11} rad/s. The data suggests some reduction in magnitudes over time, though there is no obvious correlation to the behavior of the magnetic field. The line intensification ranges from two to three orders of magnitude above the background level and persists until at least $t \approx 8$ μs. The intensities fluctuate significantly in time, likely due to the dependence of the collected signal on the time-varying spatial distribution of the excited He II ions with respect to the fiber probe.

Because the difference in the quality of fits between the four models is minor, it is challenging to extract the functional form and direction of the electric field from the spectral profiles. For most profiles, the single-mode models yield a slightly better match at the profile wings than the multi-mode models (up to 3% higher R^2 goodness-of-fit coefficient). Furthermore, reasonable fits of the multi-mode parallel model are not obtainable from $t =$ 3 μs to 6 μs. Thus, the present data weakly suggests that the electric fields are better represented by the single-mode form of Eq. A.1. However, there is no significant difference in the quality of fits between the single-mode perpendicular and single-mode parallel cases and therefore no indication of electric field direction. In this study, the results of all four models are considered feasible. The task of conclusively determining the electric field functional form and direction directly from the observed spectral profiles is left for a future experiment,

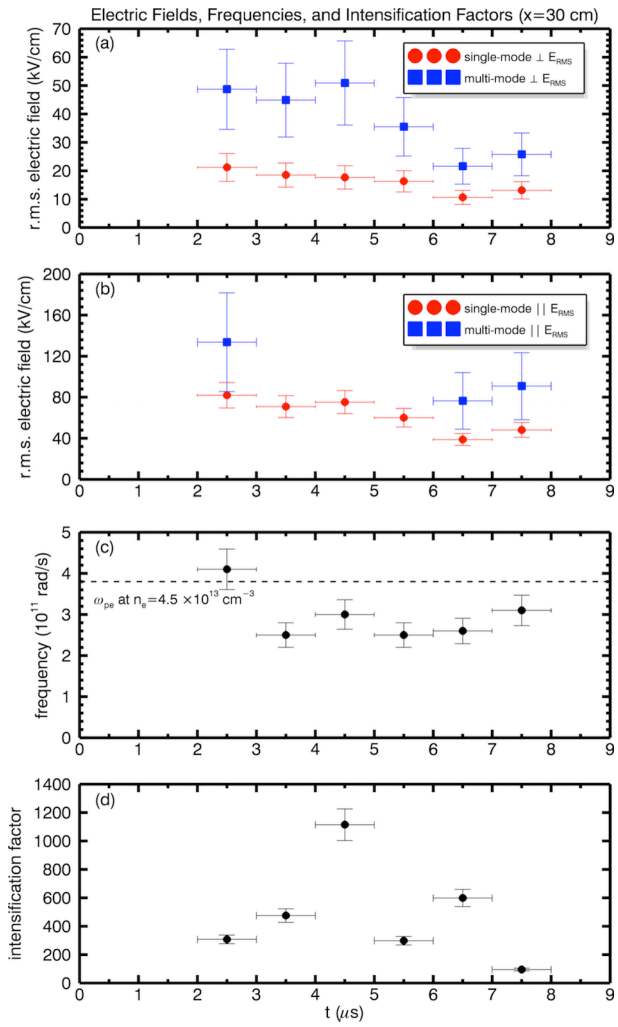

Figure A.7: Best-fit electric field magnitudes (in kV/cm), frequencies (in 10^{11} rad/s), and intensification factors versus time (in μs), extracted from a series of He II 468.6 nm line profiles obtained with C debris plasma present and integrated for 1 μs each. The plots show (a) perpendicular single-mode (circles) and multi-mode (squares) root-mean-square magnitudes, (b) parallel single-mode (circles) and multi-mode (squares) root-mean-square magnitudes, (c) frequencies, and (d) intensification factors (the factors by which the collected, wavelength-integrated signal intensifies relative to the background level) measured between $t = 2$ μs and 8 μs.

discussed in Section A.4.

It is important to acknowledge two subtleties of the fitting process used to extract electric field magnitudes. First, because the line shape function F is derived from a best fit to a He II 468.6 nm line profile measured without C debris plasma (Fig. A.5), its application to spectral profiles measured with C debris (as in Fig. A.6) implicitly assumes that the C debris does not affect the four broadening mechanisms included in F (Doppler broadening, instrumental broadening, pressure Stark broadening, and fine structure splitting). This assumption requires some justification. Instrumental broadening only depends on the spectroscopy apparatus and is obviously unaffected by the presence of C debris, eliminating it from consideration. Pressure Stark broadening due to interactions of the He II emitter ions with nearby C debris ions and electrons can also be neglected due to the low electron density. Tabulated Stark broadening data for the He II 468.6 nm line [26] indicates that the electron density must be larger than $\sim 10^{15}$ cm^{-3} in order to detect this effect at the present resolution, while an estimate of the actual electron density (utilizing Thomson scattering measurements [48] and assuming a spherical debris expansion that stops at 30 cm from the target) yields only $\sim 10^{13}$ cm^{-3}. In fine structure splitting, the relative intensities of the different fine structure components can change as a result of a sudden increase in electron temperature due to the explosive C debris plasma, modifying the line shape. However, PrismSPECT simulations have verified that this effect is minor even at electron temperatures of ~ 1 keV, resulting in less than 5% variation in the extracted electric field magnitudes. Finally, Doppler broadening is the least trivial mechanism to consider because the explosive C debris plasma can accelerate the He II ions (as in Chapter 2) or heat them above their estimated background temperature of $T_i \approx 0.4$ eV. Without spectral profiles of an additional He II line or an independent ion velocity diagnostic, an accurate assessment of the Doppler contribution cannot be made. However, in accordance with the analysis of Chapter 3, He II ion acceleration due to laminar coupling in the blow-off plane ($z = 0$ cm) is primarily perpendicular to the magnetic field. As the collection axis is presently oriented along the magnetic field (and thus perpendicular to the acceleration), additional Doppler broadening

should not be significant. Moreover, in the framework of the single-mode and multi-mode theoretical models presented in the previous subsection, the detectability of modulations in the measured profiles places an upper limit on ion heating because an excessive amount of Doppler broadening would overlap neighboring satellites to the point that the modulations would be completely "washed out." To estimate this upper limit, a rough criterion for the detection of modulations is defined as follows: the FWHM of the broadened satellites cannot exceed the spacing $\Delta\lambda_E$ between them. Considering only Doppler and instrumental broadening for the moment and approximating both effects as Gaussians, a satellite separation of $\Delta\lambda_E \approx 0.029$ nm (as measured from the wavelength profile analyzed in Fig. A.3, Fig. A.4, and Fig. A.6) places the upper limit on the ion temperature at $T_i \approx 1.4$ eV. Inclusion of other broadening mechanisms only acts to further reduce the upper limit. This small increase from the background temperature of $T_i \approx 0.4$ eV results in less than 1% variation in the extracted electric field magnitudes. Thus, the determination of the line shape function F from a best fit to a He II 468.6 nm line profile measured without C debris plasma is well justified.

The second subtlety of the fitting process is that even though the theoretical best fits match the general shape of the observed broadened peaks quite well, they often fail to replicate the modulations, as evidenced by Fig. A.6. More specifically, in most of the fits, the overlap of the individual broadened satellites is sufficient to "wash out" the modulations. One possible explanation for this discrepancy is the oversimplified approach used in the derivation of the theoretical profiles of Eq. A.5 and Eq. A.10. To obtain fits that better reproduce the observations, a more rigorous treatment of fine structure [66] and consideration of resonant non-adiabatic features [45] may be necessary. Another possibility is that neither single-mode nor multi-mode monochromatic electric fields (Eq. A.1 and Eq. A.6) perfectly represent the actual electric field structure that arises during debris-ambient interaction. A better fit might therefore require the derivation of theoretical spectra corresponding to more complex forms of oscillatory electric fields. Modifying or completely abandoning the framework of the single-mode and multi-mode models presented here would also require a revision to the previous argument for why additional ion heating (and thus Doppler broadening) cannot be

significant. Such issues are outside the scope of this study.

A.4 Interpretation of Electric Fields

In order to interpret the spectroscopic electric field measurements, they are first compared to the theoretical fields expected to arise in the interaction between explosive debris plasma and magnetized ambient plasma. As detailed in Chapter 1, an expanding debris plasma can couple momentum and energy to magnetized ambient plasma via collision-less, collective processes associated with two types of electric fields: laminar and turbulent [5]. The laminar electric field follows from

$$\vec{E}_{lam} = -\frac{1}{en_e}\vec{\nabla}p_e - \frac{1}{4\pi en_e}\vec{B}\times\left(\vec{\nabla}\times\vec{B}\right) - \frac{1}{en_e c}\sum\nolimits_i \vec{J}_i \times \vec{B}. \tag{1.9}$$

Under the experimental plasma parameters, the strongest laminar fields arise in the vicinity of the magnetic compression and diamagnetic cavity edge, where the magnetic pressure gradient and cross-field ion current terms are large and the electron pressure gradient term is relatively insignificant. Utilizing the measured magnetic field profiles of Fig. A.2, the maximal laminar fields are estimated to be $\sim 10^{-2}$ kV/cm, orders of magnitude smaller than the measured $\sim 10^{2}$ kV/cm. The discrepancy indicates that the laminar field of Eq. 1.9 does not correspond to the measurements.

Turbulent electric fields associated with collision-less debris-background coupling arise due to certain instabilities. Two candidates are the ion-ion streaming instability [47] and the modified two-stream instability [40]. In accordance with Eq. 1.4 and the satisfied condition $\beta_e \ll 1$ (outside of the diamagnetic cavity), these instabilities can only develop for sub-Alfvénic ($M_A < 1$) debris expansions. The marginally super-Alfvénic ($M_A \approx 1.1$) expansion on average and large velocity spread in the present experiment thus indicate that the candidate instabilities can potentially exist. Under the experimental parameters, the characteristic frequencies of the ion-ion streaming instability (on the order of the ion plasma frequency) and the modified two-stream instability (on the order of the lower-hybrid frequency) are $\sim 10^{9}$ rad/s and $\sim 10^{7}$ rad/s, respectively. Again, these fall considerably short

of the measured $\sim 10^{11}$ rad/s. Thus, turbulent electric fields associated with collision-less debris-ambient coupling mechanisms also do not account for the measurements directly.

It follows that the measured electric fields must correspond to a secondary effect, likely driven by the laminar or turbulent electric fields discussed previously. The estimated total electron density at the observation position provides insight into the nature of this effect. Assuming a spherical debris expansion that stops at the diamagnetic cavity edge, Thomson scattering measurements [48], in combination with the known LAPD background, infer a total electron density of $\approx 5.1 \times 10^{13}$ cm^{-3} at 30 cm from the target. At this density, the electron plasma frequency is $\sim 10^{11}$ rad/s, consistent with the measured frequencies of Fig. A.7. The most plausible explanation for strong electric fields with frequencies in this range is the electrostatic electron beam-plasma instability, which is a Langmuir mode strongly excited by a tenuous beam of fast electrons. The growth rate of the most unstable mode is on the order of the electron plasma frequency, corresponding to a characteristic "e-folding" time of $\sim 10^{-11}$ s. Saturation can thus be easily achieved on the ~ 1 μs time scales of the measurements.

To further motivate the plausibility of the electron beam-plasma instability, a simple non-linear saturation model [20] demonstrates that the measured electric field magnitudes and frequencies are consistent and feasible provided that sufficiently fast electrons are generated during debris-ambient interaction. Assuming a cold electron beam of density n_b and speed V_b injected into a cold, stationary plasma of electron density n_0, and requiring the beam density fraction $f \equiv \frac{n_b}{n_0} \ll 1$, the instability saturates by beam electron trapping at an electric field magnitude

$$E_{sat} = (2^{\frac{5}{3}} \pi m_e n_0 f^{\frac{4}{3}} V_b^2)^{\frac{1}{2}}. \tag{A.11}$$

Utilizing Eq. A.11 initially appears problematic because it contains three variables (n_0, f, and V_b). Although an estimate of the total electron density exists, the portions of that total density that participate as the fast electron beam n_b and as the stationary background n_0 are unknown. However, a self-consistent solution can be obtained for n_0 and f by simultaneously solving two independent equations that relate them, leaving only the beam speed V_b as a

variable. The first equation follows from the definition of the total electron density $n_{total} = n_0 + n_b$, allowing the beam density fraction f to be written as

$$f = \frac{n_{total}}{n_0} - 1. \tag{A.12}$$

The second equation follows from the oscillation frequency of the most unstable mode in the electron-beam plasma instability, given by

$$\omega_{E,fast} = \omega_{pe}\left(1 - \frac{1}{2^{\frac{4}{3}}} f^{\frac{1}{3}}\right). \tag{A.13}$$

Using the definition of the electron plasma frequency $\omega_{pe} = \sqrt{\frac{4\pi n_0 e^2}{m_e}}$ and solving for f in Eq. A.13 yields

$$f = 16\left(1 - \sqrt{\frac{m_e}{4\pi n_0 e^2}}\omega_{E,fast}\right)^3. \tag{A.14}$$

In order to solve for f and n_0 simultaneously, Eq. A.12 utilizes $n_{total} = 5.1 \times 10^{13}$ cm^{-3} from Thomson scattering measurements, while Eq. A.14 obtains $\omega_{E,fast} = 3.0 \times 10^{11}$ rad/s from the average of the measured electric field frequencies of Fig. A.7, implicitly assuming that the measured frequencies correspond to the most unstable mode. This yields $f \approx 0.14$ and $n_0 \approx 4.5 \times 10^{13}$ cm^{-3}. Fig. A.8 shows a plot of the saturation electric field E_{sat} of Eq. A.11 versus the remaining variable V_b, using the determined values of f and n_0. The saturation field is compared to the maximum measured root-mean-square electric field magnitudes corresponding to the four models (single-mode perpendicular, single-mode parallel, multi-mode perpendicular, and multi-mode parallel). It follows that, within the framework of the simple saturation model, the measured electric field magnitudes and frequencies of Fig. A.7 are consistent with the electron beam-plasma instability provided that sufficiently fast electrons exist. For example, the maximum electric field of 134 ± 48 kV/cm inferred from the spectroscopic measurements (corresponding to the multi-mode parallel model) requires an electron beam speed of $V_b = (2.6 \pm 0.9) \times 10^9$ cm/s.

There is, in fact, additional evidence for the existence of such fast electrons. Emission of the He II 468.6 nm line requires a population of He II ions to spontaneously transition from energy levels with principal quantum number $n = 4$ to $n = 3$. The observed orders-of-magnitude intensification of the line, both in the spectra of this experiment and in the

wavelength-filtered images of He II ions in the experiment of Chapter 2, therefore indicates a comparable increase of the $n = 4$ level population. The vast majority of the He II ions in the steady-state background plasma of the LAPD are initially in the $n = 1$ ground state, as verified by the collisional-radiative code PrismSPECT [38]. This implies that the interaction of explosive C debris with He background populates the $n = 4$ level via collisional excitation primarily from the $n = 1$ ground state, which requires free electrons with at least ≈ 51 eV of kinetic energy, corresponding to a speed of at least 3.0×10^8 cm/s. As expected, this significantly exceeds the LAPD ambient electron thermal speed of 1.7×10^8 cm/s and is comparable to the beam speeds necessary to produce the measured electric field magnitudes, in accordance with Fig. A.8. Moreover, the orders-of-magnitude intensification persists for at least 7 μs in this experiment (as shown in Fig. A.7) and for at least 13 μs in the experiment of Chapter 2 even though the characteristic spontaneous decay time from $n = 4$ to $n = 3$ is only $\sim$ 10 ns, indicating that the $n = 4$ level is continually repopulated via collisions with energetic electrons. More direct evidence of energetic electrons streaming along the magnetic field lines also follows from the field-aligned biased Langmuir probe of Chapter 2, which measures directed kinetic energies of > 50 eV.

The results of this study lead to the following general picture: as the explosive C debris plasma expands through the magnetized He ambient plasma, the resulting laminar or turbulent electric fields accelerate a small fraction of the total electron population to speeds much greater than those of the debris expansion and the thermalized LAPD ambient electrons. The fast electrons excite ground state He II ions via collisions, causing intensification in the He II 468.6 nm line. Additionally, the streaming of the fast electrons through the relatively slow debris and background plasmas leads to the development of the electron beam-plasma instability. The strong electric fields associated with this instability, which oscillate near the electron plasma frequency, then broaden and modulate the profile of the He II 468.6 nm line, in accordance with the wave field Stark effect. It should be noted that the laminar or turbulent fields that generate the fast electrons can be relatively small. For example, a field of only 5×10^{-2} kV/cm acting over a distance of 5 cm (reasonable parameters for a laminar

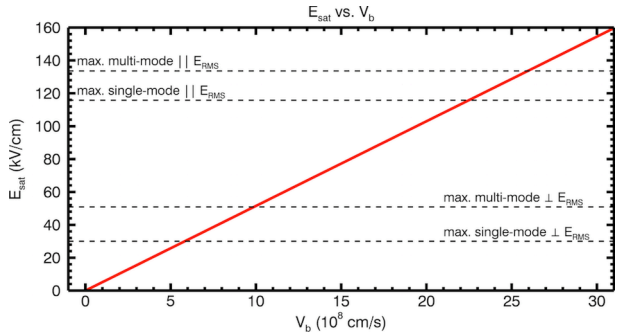

Figure A.8: Plot of the saturation electric field E_{sat} (in kV/cm) versus the remaining variable beam speed V_b (in 10^8 cm/s), using the calculated values of $f \approx 0.14$ and $n_0 \approx 4.5 \times 10^{13}$ cm^{-3} in Eq. A.11 (solid line). The result is compared to the maximum measured electric field magnitudes corresponding to the four models (dashed lines). The measured electric field magnitudes are feasible provided that a beam of fast electrons ($\sim 10^9$ cm/s) is generated during C debris - He background interaction.

electric field based on estimates from Fig. A.2) accelerates an initially stationary electron to a sufficient speed of 10^9 cm/s. Electric fields of such small magnitudes do not produce an observable effect on the He II 468.6 nm line, and only the much stronger fields associated with the resulting electron beam-plasma instability are detected.

The exact mechanism responsible for generating the fast electron population remains to be determined. However, the persistence of the measured electric fields until at least $t \approx 8$ μs, long after the collapse of the diamagnetic cavity at $t \approx 5$ μs, offers some insight at late times. Because the electron beam-plasma instability is electrostatic, the electric field that generates fast electrons must have a component parallel to the magnetic field. For quasi-perpendicular debris expansion, the laminar electric field of Eq. 1.9 is unlikely to produce such a component. After the collapse of the diamagnetic cavity, the only remaining significant contribution is the cross-field ion current term, which primarily generates an azimuthal field. The modified two-stream instability [40], one of the candidates for turbulent debris-background coupling, offers a more promising explanation. In low electron beta plasma ($\beta_e \ll 1$), this instability develops due to a relative sub-Alfvénic ($M_A < 1$) drift between the expanding debris ions

and magnetically confined electrons in the direction perpendicular to the magnetic field, resulting in a transfer of ion perpendicular drift energy into electron parallel energy. It is typically assumed that this leads to a bulk heating of the electrons along the magnetic field. However, particle simulations [57] have shown that, under certain conditions, a small fraction of the electron population can be monotonically accelerated along the magnetic field over multiple oscillations of the instability to almost an order of magnitude above the electron thermal speed, resulting in a supra-thermal tail in the velocity distribution rather than a bulk heating. In the present experiment, a sub-Alfvénic debris ion population arriving in the collection field of view after the collapse of the diamagnetic cavity can potentially drive the modified two-stream instability and generate a fast tail in the parallel electron velocity distribution. The tail would then effectively constitute the fast, tenuous electron beam that drives the electron beam-plasma instability, as in the simple non-linear saturation model employed previously. Prior to the diamagnetic cavity collapse, both turbulent and laminar electric fields can potentially be involved in the generation of fast electrons, though consideration of this more complicated case is outside the scope of this work.

Future experiments will investigate the nature of the electric fields associated with debris-ambient interaction in greater detail. Specifically, simultaneous observation of the interaction via two orthogonal spectroscopic probes will allow for a measurement of electric field direction and possibly the functional form by correlating best fits of parallel and perpendicular wave field Stark effect models. In combination with Langmuir probe detection of fast electrons, the results will yield conclusive confirmation of the electron beam-plasma instability. Correlation of spectroscopic measurements of this instability to a detailed mapping of the C debris ion distribution via wavelength-filtered high-speed imaging or planar laser-induced fluorescence (see Appendix B or [8]) will provide insight into the laminar or turbulent electric fields involved in the generation of the necessary fast electrons and shed light on collision-less coupling mechanisms between explosive debris plasma and magnetized ambient plasma.

A.5 Summary

This appendix has presented preliminary evidence of instabilities associated with the interaction of explosive debris plasma and magnetized ambient plasma. Utilizing the experimental platform detailed in Chapter 2 under a similar configuration, the electric fields associated with the marginally super-Alfvénic ($M_A \approx 1.1$), quasi-perpendicular expansion of laser-produced C debris plasma through a preformed, magnetized He ambient plasma have been investigated via emission spectroscopy and wave field Stark effect theory. The spectroscopic measurements and a detailed analysis yield the following important results:

- Spectral profiles of the He II 468.6 nm line measured at the spatial position corresponding to the maximum extent of the diamagnetic cavity are observed to intensify, broaden, and develop modulations immediately after the magnetic compression passes through the collection field of view, and the effects persist long after the diamagnetic cavity collapse. While the line intensification indicates energetic electrons above background thermal levels, the modulations suggest the development of monochromatic electric fields, and Fourier analysis verifies the existence of a distinct modulation wave number (corresponding to a distinct electric field frequency) embedded in the wavelength profiles.

- Time-dependent Stark effect models corresponding to single-mode and multi-mode monochromatic electric fields, in combination with PrismSPECT-generated synthetic spectra that take all other line broadening mechanisms into account, are applied to the He II 468.6 nm line profiles, yielding a time series (1 μs resolution) of electric field magnitudes ($\sim 10^2$ kV/cm) and frequencies ($\sim 10^{11}$ rad/s). The variation in the quality of the fits of the different models is too small to conclusively determine the electric field direction and functional form, and every model is considered feasible at present.

- The proximity of the measured frequencies to the expected electron plasma frequency

suggests the development of the electrostatic electron beam-plasma instability, and a simple saturation model verifies that the measurements are feasible provided that a sufficiently fast electron population ($\sim 10^9$ cm/s) is generated during debris-ambient interaction. This is consistent with the observed orders-of-magnitude intensification in both the spectra of this experiment and the wavelength-filtered images of Chapter 2. The field-aligned biased Langmuir probe measurements of Chapter 2 confirm the existence of such energetic electrons streaming along the magnetic field lines.

- A possible source of the energetic electrons is the modified two-stream instability, driven by a sub-Alfvénic debris ion population arriving in the collection field of view after the collapse of the diamagnetic cavity. This instability can accelerate electrons along the magnetic field lines, forming a supra-thermal tail in the velocity distribution.

APPENDIX B

Feasibility of Laser-Produced Plasma Characterization via Planar Laser-Induced Fluorescence (PLIF)

B.1 Overview

Exploding, energetic plasmas produced by laser ablation of solid targets have been extensively utilized in the field of laboratory astrophysics. Laser-ablated plasmas expanding into ambient magnetic fields are highly useful to the study of diamagnetic cavity formation, anomalous magnetic diffusion, and plasma instabilities [15, 18]. In addition, super-Alfvénic ablation plasma explosions into magnetized background plasmas are indispensable for laboratory investigations of astrophysical collisionless shocks and high-altitude nuclear explosions [49, 56, 21]. In order to better characterize ablation plasmas, planar laser induced fluorescence (PLIF) imaging has been proposed as a diagnostic. PLIF is a noninvasive optical technique that has been widely employed to obtain qualitative visualizations, concentrations, and velocities of specific ions, atoms, and molecules [36, 28, 2]. Its application to laser-ablated plasmas can yield the three-dimensional spatial distribution and temporal evolution of specific ion charge states. In the context of super-Alfvénic ablation plasma expansions into magnetized background plasmas, PLIF imaging can generate visualizations of diamagnetic cavity formation and assess coupling between ablated and background plasma ions, potentially providing an experimental evaluation of recent hybrid and kinetic simulation studies [63, 29].

We consider here the application of PLIF imaging to carbon plasmas produced by energetic laser ablation of graphite. As a first step, we confine ourselves to the case of plasma

expansion into vacuum with no external magnetic field. In previous studies, PLIF has been applied to carbon atoms [60] and molecules [30], and its feasibility with C III ions [41] and C V ions [55] in tokamak edge plasmas has been analyzed. However, to our knowledge, this is the first study examining the feasibility of PLIF with carbon ions in laser-ablated plasmas. We first employ a hydrodynamics code to simulate the temperatures and densities of the expanding ablation plasmas. Next, we input these plasma parameters into a detailed collisional-radiative code, yielding the time-dependent energy level populations of the various ion charge states. By examining the level populations, we identify several promising schemes accessible to commercially available tunable lasers for the C I atom, the C II ion, and the C V ion. We then employ a two-level model of optical pumping to estimate the signal-to-noise ratios yielded by the identified schemes under reasonable experimental configurations.

B.2 Hydrodynamic and Collisional-Radiative Simulations

In standard PLIF imaging, a pulsed laser tuned to a specific transition line irradiates a sheet of plasma, exciting a particular species and causing intensified fluorescence from the irradiated plasma region. The fluorescence is collected perpendicular to the beam sheet through a narrow-bandwidth spectral filter and imaged onto a gated ICCD camera. Background subtraction yields a spatially and temporally resolved image of the probed species within the laser-irradiated volume. Repetition of the experiment at successive beam sheet positions and times thus generates a visualization of the three-dimensional spatial distribution and temporal evolution of the species.

For successful imaging, the tuned laser must cause a significant increase in the upper energy level population of the pumped transition, such that the resulting intensification in fluorescence can be separated from background emission. However, the maximum population that can be attained by the upper level via optical pumping is limited by saturation, at which the ratio of the upper to lower level populations approaches the ratio of the corresponding statistical weights ($n_{upper}/n_{lower} \approx g_{upper}/g_{lower}$). Typically, this ratio is of order unity. A

Parameter	Plasma A	Plasma B
wavelength	1064 nm	1064 nm
peak irradiance	1 TW/cm^2	10 TW/cm^2
pulse width (FWHM)	50 ns	5 ns
peak time	50 ns	10 ns

Table B.1: Ablation laser configurations for the two carbon plasmas simulated by HELIOS.

suitable PLIF transition therefore requires the lower level to initially be highly populated and have a significantly greater population (by orders of magnitude) than the upper level. For laser-ablated plasmas, the identification of transitions that satisfy these criteria is complicated by spatial and temporal gradients in temperature and density, which cause significant variations in energy level populations. In an attempt to determine useful PLIF schemes under such highly non-uniform plasma conditions, hydrodynamic and collisional-radiative simulations are employed in combination.

The radiation-hydrodynamics code HELIOS [39] is utilized to model the spatially and temporally dependent temperatures and densities of carbon plasmas produced via energetic laser ablation of a graphite target. HELIOS evaluates plasma parameters along a one-dimensional set of spatial points. These points correspond to boundaries of constant-mass zones and are initially configured ~ 2 μm apart from each other. During ablation, the zone boundary points move with the plasma fluid (i.e., Lagrangian hydrodynamics), preserving the total mass between them. A hemispherical ablation plasma expansion is assumed, and only the four mass zone boundaries that move significantly from the initial target surface (> 0.5 cm) during the simulation time are considered. Two different plasmas are simulated with the laser parameters given in Table B.1, and the results for one of the simulations (Plasma A) are shown in Figure B.1.

The time histories of electron temperatures and ion densities corresponding to each HELIOS mass zone boundary are individually fed into the collisional-radiative code Prism-

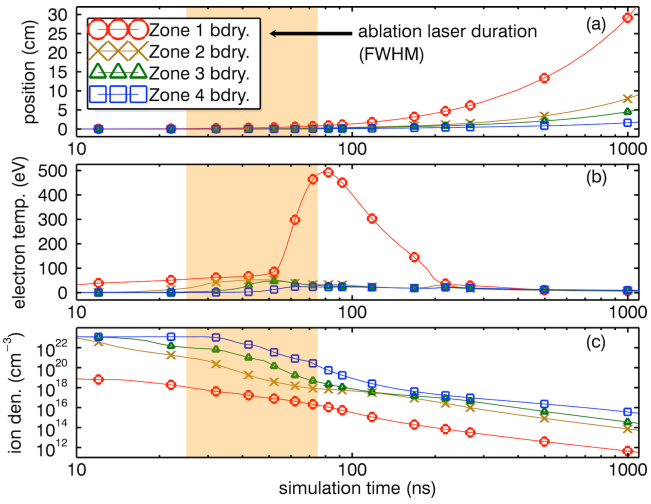

Figure B.1: HELIOS simulation results for Plasma A, showing the temporal evolution of (a) mass zone boundary positions relative to the initial target surface, (b) electron temperatures, and (c) ion densities of the carbon plasma for $\sim$ 1000 ns after the start of the ablation laser.

SPECT [38]. Each zone is thus treated as a separate, temporally dynamic, spatially uniform plasma with the temperatures and densities predicted at its HELIOS boundary. Prism-SPECT calculates the time-dependent energy level populations of the various carbon charge states by utilizing a detailed atomic model and solving sets of rate equations that include all population and de-population mechanisms. From these results, transitions for which the lower level population significantly exceeds that of the upper level are identified for the C I atom, the C II ion, and the C V ion. The schemes are summarized in Table B.2, and the corresponding level populations are plotted in Figure B.2. For each of the schemes, the excitation and fluorescence wavelengths are equivalent (i.e., two-step schemes).

The simulations demonstrate that the applicability of PLIF to specific charge states is highly dependent on the ablation laser configuration, location within the plasma, and time after ablation. The C V ion is most prevalent only within the outermost and hottest mass zone of the first simulated ablation plasma (Zone 1, Plasma A), whereas the C I atom and C II ion are only populous within the innermost and coolest mass zone of the second simulated ablation plasma (Zone 4, Plasma B). Furthermore, the lower level populations significantly exceed those of the upper level (by over an order of magnitude) only during certain time

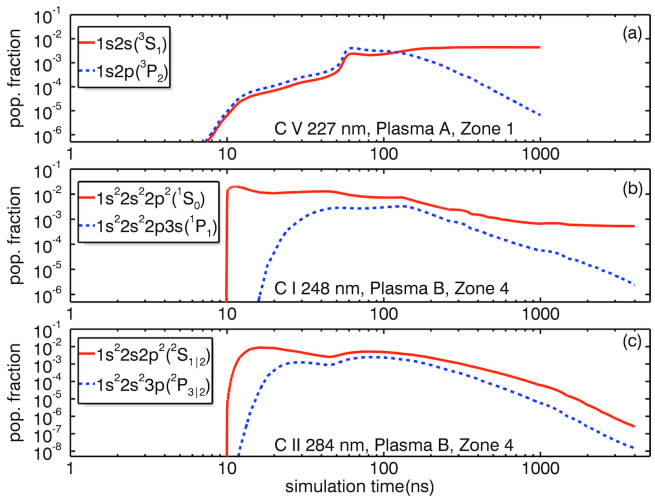

Figure B.2: PrismSPECT simulation results, showing the lower (solid line) and upper (dashed line) energy level population fractions as a function of time for the identified (a) C V 227 nm scheme, (b) C I 248 nm scheme, and (c) C II 284 nm scheme.

intervals. For C V and C I, the slow decay of the metastable lower levels generates favorable conditions for PLIF after $\sim$ 300 ns and $\sim$ 900 ns, respectively. For C II, favorable PLIF conditions exist after $\sim$ 1000 ns. Only time intervals within these favorable ranges are considered for signal-to-noise analysis.

B.3 Estimation of PLIF Signal-to-Noise Ratio

The signal-to-noise ratios yielded by the identified PLIF schemes are estimated by calculating the total detected fluorescence with and without tuned laser pumping under reasonable experimental configurations. The results are stated in Table B.2. The rate of detected signal photo-electrons from the additional fluorescence caused by laser pumping is given by $dS/dt = A_{ul}(n_{u,p}(t) - n_{u,np}(t))V_{beam}(\Omega/4\pi)f\eta$, and the rate of detected photo-electrons from background plasma fluorescence is given by $dB/dt = A_{ul}n_{u,np}(t)V_{tot}(\Omega/4\pi)f\eta + C$. In these equations, A_{ul} is the rate of spontaneous emission of the fluorescence transition (extracted from NIST data [34] and given in Table B.2), $\Omega/4\pi$ is the solid angle fraction spanned by the collection optics (5×10^{-4}), η is the detector quantum efficiency (0.14), and f is the

spectral filter transmissivity (0.10). C represents the photo-electron rate from all other transition lines within the assumed ± 10 nm bandwidth of the spectral filter and is estimated from spectra simulated by PrismSPECT. V_{tot} is the total optical collection volume, which is assumed to be a cubical section of the corresponding HELIOS mass zone. V_{beam} is the volume of the tunable laser beam, which irradiates a 0.5 cm thick sheet of V_{tot}. $n_{u,np}(t)$ is the time-dependent population density of the upper level outside of the laser-irradiated volume V_{beam} and is extracted directly from the corresponding PrismSPECT simulation. $n_{u,p}(t)$ is the time-dependent population density of the upper level within the laser-irradiated volume V_{beam} and is approximated via a two-level model of optical pumping, with the pump laser parameters based on commercially available optical parametric oscillator (OPO) tunable systems (2 mJ per pulse, 5 ns pulse length, $\sim 1 \times 10^{-3}$ eV spectral bandwidth). The OPO laser pulse is applied during the time intervals specified by the *beam time* parameter in Table B.2. The pumped and non-pumped time-dependent population densities $n_{u,p}(t)$ and $n_{u,np}(t)$ are inserted into the equations for dS/dt and dB/dt, and these rates are integrated over the 45 ns time intervals specified by the *collection time* parameter in Table B.2 to obtain the total number of collected signal (S) and background (B) photo-electrons. The signal-to-noise ratios are then calculated by assuming only Poisson shot noise and using $S/\sqrt{S+B}$. Figure B.3 shows the simulated effect of the OPO laser on the upper level population density for the C V 227 nm scheme.

The signal-to-noise ratios stated in Table B.2 are determined under the assumption that the signal and background photo-electrons are collected by a single detector (e.g., a photomultiplier tube). All three identified schemes provide more than sufficient signal for this type of detection. For PLIF imaging, however, multiple detectors (e.g., a pixel array) are necessary. For an $n \times n$ element array, the signal-to-noise ratio of each element is approximated by dividing the stated signal-to-noise value by n. From this, it follows that for a 30×30 element array, the C V 227 nm and C I 248 nm schemes yield an uncertainty of $< 10\%$ within just one dataset. The C II 284 nm scheme yields the same level of uncertainty by averaging over ~ 50 datasets.

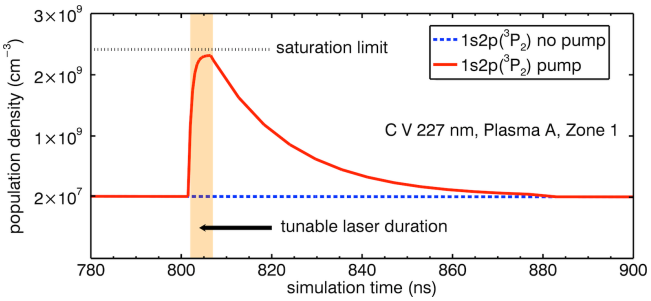

Figure B.3: Two-level model simulation of the effect of an OPO tunable laser system on the upper $1s2p(^3P_2)$ level of the C V 227 nm scheme between $\sim 800-900$ ns in Zone 1 of Plasma A. The laser pulse increases the upper level population density by two orders of magnitude, nearly to the saturation limit.

Parameter:	**C V**	**C I**	**C II**
excitation λ (nm)	227.091	247.856	283.671
fluorescence λ (nm)	227.091	247.856	283.671
A_{ul} (s^{-1})	5.67×10^7	2.80×10^7	3.30×10^7
lower level config.	$1s2s(^3S_1)$	$2s^22p^2(^1S_0)$	$2s2p^2(^2S_{\frac{1}{2}})$
upper level config.	$1s2p(^3P_2)$	$2s^22p3s(^1P_1)$	$2s^23p(^2P_{\frac{3}{2}})$
HELIOS ablation plasma	Plasma A	Plasma B	Plasma B
HELIOS mass zone	Zone 1	Zone 4	Zone 4
beam volume V_{beam} (cm^3)	50	1.125	1.125
total volume V_{tot} (cm^3)	1000	3.375	3.375
beam time (ns)	802-807	3880-3885	2030-2035
collection time (ns)	802-847	3880-3925	2030-2075
signal S (photoel.)	9.459×10^5	3.831×10^5	3.580×10^4
background B (photoel.)	3.251×10^5	1.842×10^5	3.312×10^5
signal-to-noise $S/\sqrt{S+B}$	**839**	**509**	**59**

Table B.2: Identified PLIF schemes for laser-ablated carbon plasmas and estimated signal-to-noise ratios for specific ablation plasma conditions, mass zones, and simulation times.

B.4 Summary

We conclude that PLIF imaging of certain laser-ablated carbon plasma species using commercially available OPO tunable lasers is feasible. Even though the applicability of PLIF to ablation plasmas is highly sensitive to local conditions, we have succeeded in identifying two-step schemes that yield sufficient signal-to-noise ratios within specific spatial regions and time intervals for the C I atom, the C II ion, and the C V ion. This analysis motivates further development of the PLIF diagnostic for the eventual visualization of diamagnetic cavity formation and assessment of ion coupling in the context of ablation plasma expansions into magnetized background plasmas [43].

References

[1] Behrouz Amini. Detection of lowfrequency instability through the satellites of a hydrogenlike atom. *Physics of Fluids*, 29(11):3775–3778, November 1986.

[2] A. D. Bailey. *Drift Wave Ion Fluid Velocity Field Measured By Planar Laser Induced Fluorescence*. PhD thesis, California Institute of Technology, 1993.

[3] Michel Baranger and Bernard Mozer. Light as a plasma probe. *Physical Review*, 123(1):25–28, July 1961.

[4] V.P. Bashurin, A.I. Golubev, and V.A. Terekhin. The collisionless deceleration of an ionized cloud dispersing in a uniform plasma in a magnetic field. *Journal of Applied Mechanics and Technical Physics*, 24(5):614–620, 1983.

[5] Yu. A. Berezin, G. I. Dudnikova, M. P. Fedoruk, and V. A. Vshivkov. Explosion phenomena in collisionless plasmas at super-alfvenic speed. *International Journal of Computational Fluid Dynamics*, 10(2):117–126, 1998.

[6] D. I. Blochinzew. *Physikalische Zeitschrift der Sowjetunion*, 4:501, 1933.

[7] B C Boland, F E Irons, and R W P McWhirter. A spectroscopic study of the plasma generated by a laser from polyethylene. *Journal of Physics B: Atomic and Molecular Physics*, 1(6):1180–1228–2, November 1968.

[8] A. S. Bondarenko, D. B. Schaeffer, E. T. Everson, C. G. Constantin, S. E. Clark, and C. Niemann. Feasibility of characterizing laser-ablated carbon plasmas via planar laser induced fluorescence. *The Review of Scientific Instruments*, 83(10):10E515, October 2012.

[9] AS Bondarenko, DB Schaeffer, ET Everson, SE Clark, CG Constantin, and C Niemann. Spectroscopic measurement of high-frequency electric fields in the interaction of explosive debris plasma with magnetized background plasma. *Physics of Plasmas (1994-present)*, 21(12):122112, 2014.

[10] L. F. Burlaga, R. M. Skoug, C. W. Smith, D. F. Webb, T. H. Zurbuchen, and Alysha Reinard. Fast ejecta during the ascending phase of solar cycle 23: ACE observations, 1998–1999. *Journal of Geophysical Research: Space Physics*, 106(A10):20957–20977, October 2001.

[11] Francis F Chen. Langmuir probe diagnostics. In *IEEE-ICOPS Meeting, Jeju, Korea*, 2003.

[12] Augustine Y. Cheung, R. R. Goforth, and David W. Koopman. Magnetically induced collisionless coupling between counterstreaming laser-produced plasmas. *Physical Review Letters*, 31(7):429–432, August 1973.

[13] S. E. Clark, E. T. Everson, D. B. Schaeffer, A. S. Bondarenko, C. G. Constantin, C. Niemann, and D. Winske. Enhanced collisionless shock formation in a magnetized plasma containing a density gradient. *Phys. Rev. E*, 90:041101, Oct 2014.

[14] S. E. Clark, D. Winske, D. B. Schaeffer, E. T. Everson, A. S. Bondarenko, C. G. Constantin, and C. Niemann. Hybrid simulation of shock formation for super-alfvénic expansion of laser ablated debris through an ambient, magnetized plasma. *Physics of Plasmas (1994-present)*, 20(8):082129, August 2013.

[15] A. Collette and W. Gekelman. Structure of an exploding laser-produced plasma. *Physical Review Letters*, 105(19):195003, November 2010.

[16] A Collette and W Gekelman. Structure of an exploding laser-produced plasmaa). *Physics of Plasmas (1994-present)*, 18(5):055705, 2011.

[17] C. Constantin, W. Gekelman, P. Pribyl, E. Everson, D. Schaeffer, N. Kugland, R. Presura, S. Neff, C. Plechaty, S. Vincena, A. Collette, S. Tripathi, M. Villagran Muniz, and C. Niemann. Collisionless interaction of an energetic laser produced plasma with a large magnetoplasma. *Astrophysics and Space Science*, 322(1-4):155–159, August 2009.

[18] Guy Dimonte and L. G. Wiley. Dynamics of exploding plasmas in a magnetic field. *Physical Review Letters*, 67(13):1755–1758, 1991.

[19] RP Drake. The design of laboratory experiments to produce collisionless shocks of cosmic relevance. *Physics of Plasmas (1994-present)*, 7(11):4690–4698, 2000.

[20] W. E. Drummond, J. H. Malmberg, T. M. O'Neil, and J. R. Thompson. Nonlinear development of the beamplasma instability. *Physics of Fluids (1958-1988)*, 13(9):2422–2425, September 1970.

[21] Palmer Dyal. Particle and field measurements of the starfish diamagnetic cavity. *Journal of Geophysical Research*, 111:23 PP., December 2006.

[22] E. T. Everson, P. Pribyl, C. G. Constantin, A. Zylstra, D. Schaeffer, N. L. Kugland, and C. Niemann. Design, construction, and calibration of a three-axis, high-frequency magnetic probe (b-dot probe) as a diagnostic for exploding plasmas. *Review of Scientific Instruments*, 80(11):113505, November 2009.

[23] Charles C. Gallagher and Morton A. Levine. Observation of hydrogen and helium satellites in a turbulent plasma. *Journal of Quantitative Spectroscopy and Radiative Transfer*, 15(3):275–279, March 1975.

[24] W. Gekelman, H. Pfister, Z. Lucky, J. Bamber, D. Leneman, and J. Maggs. Design, construction, and properties of the large plasma research deviceThe LAPD at UCLA. *Review of Scientific Instruments*, 62(12):2875–2883, December 1991.

[25] A.I. Golubev, A.A. Solov'ev, and V.A. Terekhin. Collisionless dispersion of an ionized cloud into a homogeneous magnetized plasma. *Journal of Applied Mechanics and Technical Physics*, 19(5):602–609, 1978.

[26] Hans R. Griem. *Spectral Line Broadening by Plasmas*. Academic Press, January 1974.

[27] Hans R. Griem and H. J. Kunze. Stark broadening of two ionized-helium lines by collective electric fields in a laboratory plasma. *Physical Review Letters*, 23(22):1279–1281, December 1969.

[28] M. Harnafi and B. Dubreuil. Characterization and analysis of the CO2 laserinduced ablation of lithium target via laserinduced fluorescence and absorption spectroscopy of emitted atoms. *Journal of Applied Physics*, 69(11):7565–7571, June 1991.

[29] Dennis W. Hewett, Stephen H. Brecht, and David J. Larson. The physics of ion decoupling in magnetized plasma expansions. *Journal of Geophysical Research*, 116:12 PP., November 2011.

[30] T. Ikegami, S. Ishibashi, Y. Yamagata, K. Ebihara, R. K. Thareja, and J. Narayan. Spatial distribution of carbon species in laser ablation of graphite target. *Journal of Vacuum Science & Technology A: Vacuum, Surfaces, and Films*, 19(4):1304, 2001.

[31] M. H. Johnson and John Kierein. Combined release and radiation effects satellite (CRRES): Spacecraft and mission. *Journal of Spacecraft and Rockets*, 29(4):556–563, 1992.

[32] Anna Mária Keszler and László Nemes. Time averaged emission spectra of nd:yag laser induced carbon plasmas. *Journal of Molecular Structure*, 695–696(0):211 – 218, 2004. ¡ce:title¿Winnewisser Special Issue¡/ce:title¿.

[33] David W Koopman. Momentum transfer interaction of a laser-produced plasma with a low-pressure background. *Physics of Fluids (1958-1988)*, 15(11):1959–1969, 1972.

[34] A. Kramida, Yu. Ralchenko, J. Reader, and NIST ASD Team. NIST Atomic Spectra Database (ver. 5.2), [Online]. Available: http://physics.nist.gov/asd [2015, April 16]. National Institute of Standards and Technology, Gaithersburg, MD., 2014.

[35] S. M. Krimigis, G Haerendel, R. W. McEntire, G. Paschmann, and D. A. Bryant. The active magnetospheric particle tracer explorers (AMPTE) program. *Eos, Transactions American Geophysical Union*, 63(45):843–850, November 1982.

[36] Fred M Levinton and Fedor Trintchouk. Visualization of plasma turbulence with laser-induced fluorescence (invited). *Review of Scientific Instruments*, 72(1):898–905, January 2001.

[37] E. V. Lifshitz. Stark effect in high frequency stochastic fields in a plasma. *Soviet Journal of Experimental and Theoretical Physics*, 26:570, March 1968.

[38] J. J. MacFarlane, I. E. Golovkin, P. Wang, P. R. Woodruff, and N. A. Pereyra. SPECT3d – a multi-dimensional collisional-radiative code for generating diagnostic signatures based on hydrodynamics and PIC simulation output. *High Energy Density Physics*, 3(1–2):181–190, May 2007.

[39] J.J. MacFarlane, I.E. Golovkin, and P.R. Woodruff. HELIOS-CR – a 1-D radiation-magnetohydrodynamics code with inline atomic kinetics modeling. *Journal of Quantitative Spectroscopy and Radiative Transfer*, 99(1–3):381–397, May 2006.

[40] John B. McBride, Edward Ott, Jay P. Boris, and Joseph H. Orens. Theory and simulation of turbulent heating by the modified TwoStream instability. *Physics of Fluids*, 15(12):2367–2383, December 1972.

[41] J. M McChesney, S. I Lippmann, W. H Goldstein, and K. B Fournier. A laserinduced fluorescence diagnostic for divertors. *Review of Scientific Instruments*, 66(1):600–602, January 1995.

[42] Yō Mizuta and Akkio Ohno. Optical satellites of langmuir turbulence. *Journal of the Physical Society of Japan*, 46(4):1315–1323, 1979.

[43] C. Niemann, C. G. Constantin, D. B. Schaeffer, A. Tauschwitz, T. Weiland, Z. Lucky, W. Gekelman, E. T. Everson, and D. Winske. High-energy nd:glass laser facility for collisionless laboratory astrophysics. *Journal of Instrumentation*, 7(03):P03010, March 2012.

[44] C. Niemann, W. Gekelman, C. G. Constantin, E. T. Everson, D. B. Schaeffer, A. S. Bondarenko, S. E. Clark, D. Winske, S. Vincena, B. VanCompernolle, and P. Pribyl. Observation of collisionless shocks in a large current-free laboratory plasma. *Geophysical Research Letters*, 41(21):7413–7418, 2014.

[45] E. A. Oks and G. V. Sholin. Stark profiles of hydrogen spectral lines in a plasma with langmuir turbulence. *Zhurnal Eksperimentalnoi i Teoreticheskoi Fiziki*, 68:974–986, March 1975.

[46] Eugene Oks. *Plasma Spectroscopy: The Influence of Microwave and Laser Fields*. Springer, Berlin ; New York, 1 edition edition, June 1995.

[47] K. Papadopoulos. Heating of counterstreaming ion beams in an external magnetic field. *Physics of Fluids*, 14(4):849, 1971.

[48] D. B. Schaeffer, E. T. Everson, A. S. Bondarenko, S. E. Clark, C. G. Constantin, S. Vincena, B. Van Compernolle, S. K. P. Tripathi, D. Winske, W. Gekelman, and C. Niemann. Laser-driven, magnetized quasi-perpendicular collisionless shocks on the large plasma devicea). *Physics of Plasmas (1994-present)*, 21(5):056312, May 2014.

[49] D. B. Schaeffer, E. T. Everson, D. Winske, C. G. Constantin, A. S. Bondarenko, L. A. Morton, K. A. Flippo, D. S. Montgomery, S. A. Gaillard, and C. Niemann. Generation

of magnetized collisionless shocks by a novel, laser-driven magnetic piston. *Physics of Plasmas*, 19(7):070702–070702–4, July 2012.

[50] D. B. Schaeffer, D. S. Montgomery, A. S. Bondarenko, L. A. Morton, R. P. Johnson, T. Shimada, C. G. Constantin, E. T. Everson, S. A. Letzring, S. A. Gaillard, K. A. Flippo, S. H. Glenzer, and C. Niemann. Thomson scattering measurements of temperature and density in a low-density, laser-driven magnetized plasma. *Journal of Instrumentation*, 7(02):P02002, February 2012.

[51] DB Schaeffer, ET Everson, AS Bondarenko, SE Clark, CG Constantin, D Winske, W Gekelman, and C Niemann. Experimental study of subcritical laboratory magnetized collisionless shocks using a laser-driven magnetic piston. *Physics of Plasmas (1994-present)*, 22(11):113101, 2015.

[52] Derek Schaeffer. *Generation of Quasi-Perpendicular Collisionless Shocks by a Laser-Driven Magnetic Piston*. 2014.

[53] I.F. Shaikhislamov, Yu.P. Zakharov, V.G. Posukh, A.V. Melekhov, E.L. Boyarintsev, A.G. Ponomarenko, and V.A. Terekhin. Experimental study of collisionless super-alfvénic interaction of interpenetrating plasma flows. *Plasma Physics Reports*, 41(5):399–407, 2015.

[54] Rajiv K Singh, OW Holland, and J Narayan. Theoretical model for deposition of superconducting thin films using pulsed laser evaporation technique. *Journal of applied physics*, 68(1):233–247, 1990.

[55] C. H Skinner, S. J Zweben, F. M Levinton, and J. McChesney. Feasibility studies of two-dimensional edge turbulence measurements by laser induced fluorescence. *Review of Scientific Instruments*, 70(1):917–920, January 1999.

[56] D. S. Spicer, S. P. Maran, and R. W. Clark. A model of the pre-sedov expansion phase of supernova remnant-ambient plasma coupling and x-ray emission from SN 1987a. *The Astrophysical Journal*, 356:549, June 1990.

[57] Motohiko Tanaka and K. Papadopoulos. Creation of highenergy electron tails by means of the modified twostream instability. *Physics of Fluids (1958-1988)*, 26(7):1697–1699, July 1983.

[58] J. Torres, J. M. Palomares, A. Sola, J. J. A. M. van der Mullen, and A. Gamero. A stark broadening method to determine simultaneously the electron temperature and density in high-pressure microwave plasmas. *Journal of Physics D: Applied Physics*, 40(19):5929, October 2007.

[59] L Torrisi, S Gammino, AM Mezzasalma, AM Visco, J Badziak, P Parys, J Wolowski, E Woryna, J Krása, L Láska, et al. Laser ablation of uhmwpe-polyethylene by 438 nm high energy pulsed laser. *Applied surface science*, 227(1):164–174, 2004.

[60] K. Tsuchida, Y. Uehara, W. Sasaki, E. Kawatoh, E. Fujiwara, Y. Kato, M. Yamanaka, K. Kadota, and J. Fujita. Measurement of atomic carbon densities by the laster-induced fluorescence method with an ar2 laser. *Journal of Nuclear Materials*, 128–129(0):982–985, December 1984.

[61] Anne Barbara Underhill and John H. Waddell. *Stark broadening functions for the hydrogen lines*. U.S. National Bureau of Standards Circular603. U.S. Dept. of Commerce, National Bureau of Standards, Washington, 1959.

[62] Dan Winske and Misa Cowee. Conditions for debris-background ion interactions and collisionless shock wave generation. Technical report, Los Alamos National Laboratory (United States). Funding organisation: US Department of Defense (United States), 2012.

[63] Dan Winske and S. Peter Gary. Hybrid simulations of debris-ambient ion interactions in astrophysical explosions. *Journal of Geophysical Research*, 112(A10):A10303, October 2007.

[64] Thomas P. Wright. Earlytime model of laser plasma expansion. *Physics of Fluids (1958-1988)*, 14(9):1905–1910, September 1971.

[65] Yu.P. Zakharov. Laboratory simulation of artificial plasma releases in space. *Advances in Space Research*, 29(9):1335–1344, 2002.

[66] A. G. Zhidkov, A. N. Tkachev, and S. I. Iakovlenko. The effect of fine structure on the line shape of hydrogen-like ions. *Zhurnal Eksperimentalnoi i Teoreticheskoi Fiziki*, 91:445–453, August 1986.